A BIOCOMPATIBLE, LOCAL DRUG DELIVERY PLATFORM FOR THE CHRONIC TREATMENT OF NEUROLOGICAL DISORDERS OF THE BRAIN

by

Kevin C. Spencer

B.S. Materials Science and Engineering

University of Illinois – Urbana Champaign, 2010

SUBMITTED TO THE DEPARTMENT OF MATERIALS SCIENCE AND ENGINEERING IN PARTIAL FULFILLMENT OF THE REQUIREMENTS FOR THE DEGREE OF DOCTOR OF PHILOSOPHY IN MATERIALS SCIENCE AND ENGINEERING AT THE MASSACHUSSETTS INSTITUTE OF TECHNOLOGY

FEBRUARY 2017

Signature redacted

Signature of Author:_____
Kevin Spencer
Deparment of Materials Science and Engineering
December 20th, 2016

Signature redacted

Certified by:_____
Michael J. Cima
Department of Materials Science and Engineering
Thesis Supervisor

Signature redacted

Accepted by: _____
Donald R. Sadoway
John F. Elliott Professor of Materials Chemistry
Chair, Departmental Committee on Graduate Students

A BIOCOMPATIBLE, LOCAL DRUG DELIVERY PLATFORM FOR THE CHRONIC TREATMENT OF NEUROLOGICAL DISORDERS OF THE BRAIN

By

Kevin C Spencer

Submitted to the Department of Materials Science and Engineering on December 20, 2016 in Partial Fulfilment of the Requirements for the Degree of Doctor of Philosophy in Materials Science and Engineering

ABSTRACT

Many neurological disorders are now classified as circuit disorders, in which the underlying pathology arises from a failure in dynamic communication between anatomically distinct regions of the brain. Systemic therapies are often not effective due to their untargeted nature. The injectrode is a multifunctional probe designed to treat neurological disorders through targeted chemical and electrical stimulation directly to a focal point within the implicated neural circuit. This thesis details the characterization and biocompatibility of the injectrode for the treatment of neurological disorders on chronic timescales.

In vitro and *in vivo* infusion tests were conducted to validate the ability to deliver nanoliter scale volumes (10-1000 nl) of drug to targeted brain structures over the course of an eight week implantation period. Muscimol was delivered to deep brain structures to demonstrate effective modulation of neural activity and behavior. These findings highlight the utility of a local chemical delivery approach to treat circuit diseases of the brain.

Glial scar is a major barrier to neural probe function. A main objective of this thesis is focused on understanding the process of glial scar formation from a materials perspective. Micromotion and mechanical mismatch are thought to be key drivers of scar formation. This hypothesis was investigated using a novel 3D *in vitro* glial scar model, which replicates the magnitude and frequency of micromotions that are observed *in vivo*. Astrocytes were found to have a significant increase in cellular area and perimeter in response to micromotion compared to static control wells.

These findings were applied to improve the biocompatibility of the injectrode. Hydrogel coatings, with moduli matched to brain tissue, were formed to mitigate the effects of micromotion. These coatings were found to reduce local strain by up to 70%. *In vivo* studies were conducted to explore the impact that implant diameter and modulus have on scar formation. Hydrogel coated implants (E=11.6 kPa) were found to significantly reduce scarring at 8 weeks post implantation, compared to uncoated implants (E=70 GPa). Size effects from increasing the overall implant diameter were also observed, highlighting the importance of considering both mechanical and geometric factors when designing chronic neural implants.

Thesis Supervisor: Michael J. Cima

Title: David H. Koch Professor of Engineering

ACKNOWLEDGEMENTS

There are a countless number of individuals whose help and encouragement have made this thesis possible - I'd like to thank many of them here.

First of all, I'd like to thank my fantastic advisor, Michael Cima, for providing me with the opportunity of working in his lab for the past six years. Working in the Cima lab has been a wonderful privilege, and it amazes me to think of how much I've grown, both as a scientist and as a person throughout this time. Michael provided me with both the freedom to investigate the problems that I found interesting, as well as the tools and resources to efficiently and effectively conduct research. Michael's excitement and valuable outlook on how our work may translate to significant clinical impacts has kept me motivated throughout the long, tortuous journey of graduate school.

I am also incredibly grateful for the mentorship of Polina Anikeeva and Darrell Irvine for the valuable guidance they have provided on my thesis committee. They have consistently provided valuable insight and great support throughout my time at MIT. I will always be appreciative of the numerous discussions during my early years at MIT, which significantly shaped the directions of my project. There is no doubt that their contributions significantly improved the outcome of my thesis.

In graduate school, you tend to spend the majority of time in lab, which quickly starts to feel like your home. I feel extremely lucky to have had the opportunity to work and interact with so many wonderful people throughout my time in graduate school. I'd like to thank all Cima lab members, current and former, for making the time spent in the lab so great. The constant lunch and trivia outings were always highlights of the day, and I've formed many lifelong friendships in lab.

In addition, it's been a privilege to have so many awesome teammates on the injectrode project over the years. I'd like to especially thank Byron and Patrick for laying the

foundation for this project, and Jay for basically training me in every lab technique that I know. I'd like to thank Professor Ann Graybiel and Professor Robert Langer for their valuable insight and suggestions provided in team meetings over the past several years. The current injectrode team is pretty great too – it has been a joy working so closely with Khalil the past couple of years. Having someone to constantly brainstorm ideas with helps make even the tallest tasks seem more achievable. I'd like to thank Helen, Canan, Pauline, and everyone in the Graybiel lab for an exciting and productive last few years as well. I'm excited to see where the project goes next! I've always been amazed at how helpful and collaborative people have been at MIT. Special thanks to Sebastien Delcasso and Howard Mak who have not only been great collaborators over the past year, but are also extremely enjoyable people to work with.

I'd also like to give a special shout out to all my friends at MIT, who have made the hours spent outside of lab very enjoyable. My roommates Daniel, Audren, Ryan, as well as the unofficial roommate Carl, are some of the best dudes in town, and we've certainly had our share of great times over the years. It has been great making the transitions from undergrads to full grown "adults" with these guys. Their energy and fantastic work has certainly kept me motivated over the years as well.

Thank you to my parents for making me the person that I am today. They certainly instilled their hard work ethic in me, and I am so appreciative for all that they have provided me. I would not have been able to get to this point without their unwavering support and encouragement at every point along the way. My younger brother Jack has always been an inspiration for me – it's been great growing up with such a positive and supportive brother. I don't think I've ever heard of someone not getting along with Jack. I wish we saw each other more than a few times per year, but hopefully that'll change soon! I'd also like to thank my wonderful grandparents, Rollie, Jean, Max, and Ardys for being such great examples of how life should be lived.

Last but certainly not least, there's Beth. Beth is the most wonderful lady I've ever known, such a kind, talented, and compassionate person, and I'm so grateful to have her in my life. After finishing up her graduate work back home in Illinois, she quickly realized that I still had quite some time left. She picked up everything and came out to start a life in Boston, just to be with me. Having her by my side throughout the many highs and lows of the PhD was so important, I am eternally grateful it. As a result of our many discussions about my experiments, I highly doubt there are any architects in the world as knowledgeable in the process of glial scar formation as Beth. Can't wait to see where life takes us next!

TABLE OF CONTENTS

List of Tables

List of Figures

List of Abbreviations and Acronyms

PD	Parkinson's disease
MDD	Major Depressive Disorder
TRD	Treatment resistant despression
DBS	Deep Brain Stimulation
L-dopa	Levadopa
CNS	Central Nervous System
BBB	Blood brain barrier
MTD	Maximum tolerated dose
CED	Convection enhanced delivery
GBM	Glioiblastoma multiforme
STN	Subthalamic Nucleus
GPi	Global pallidus
DREADD	Designer receptor exclusively activated by designer drugs
IV	Intravenous
IP	Intraperitoneal
DA	Dopamine
PET	Positron emission tomography
CT	Computerized tomography
NOTA	1,4,7-triazacyclononane-1,4,7-trisacetic acid
PEG-DMA	Polyethylene glycol dimethacrylate
BS	Borosilicate
CNC	Computer numerical control
HPLC	High pressure liquid chromatography
PBS	Phosphate buffered saline
ICG	Indocyanine green
IOI	Integrative optical imaging
ECS	Extracellular space
ROI	Region of interest
PCA	Principal component analysis
GFAP	Glial fibrillary acidic protein
PDL	Poly-d-lysine
LPS	Lipopolysaccharide
TGF-β	Transforming growth factor- beta

bFGF	Basic fibroblast growth factor
PIV	Particle image velocimetry
ROIs	Reactive oxygen intermediates
FEA	Finite element analysis
TPM	3-(Trichlorosilyl) propyl methacrylate
BF	Bright field
IF	Immunofluorescent
GC	Glass capillary
6-OHDA	6-hydroxydopamine
NHP	Non-human primate

List of Appendices

1 INTRODUCTION

1.1 Circuit Disorders of the Brain: A Shift in the Therapeutic Target for Neurological Disorders

1.1.1 Clinical Rationale:

Neurological disorders are among the most prevalent and debilitating diseases in the world, contributing to approximately 10% of the global disease burden (*1*). Many neurological disorders are severely debilitating and there are often no effective treatments available to large subsets of the patient populations.

One example is Parkinson's disease (PD). PD is the second most common neurodegenerative disorder (behind Alzheimer's disease), affecting approximately 645,000 patients in the USA (*2*). Parkinson's disease affects approximately 0.3% of the total population, with incidence rates increasingly drastically beyond the age of 60 (*2*). PD is known for its very noticeable movement symptoms including resting tremor, bradykinesia (slowness or absence of movement), and muscle rigidity. Non-movement symptoms of PD include cognitive impairment, depression, and personality changes. PD is severely debilitating and carries a large cost of treatment. The cost burden of PD is estimated at $23 billion dollars annually, with approximately 50% of this cost due to productivity loss of the patient. While the origin of PD is still not fully understood, it is known that the symptoms occur as a result of the selective loss of dopaminergic neurons in the substantia nigra (SN). These neurons project to the striatum where they stimulate the release of dopamine to control movement (*3*). The loss of these neurons leads to less

dopamine in the striatum, disrupting the neural control of movement and behavior within the basal ganglia circuit (*4*).

Anxiety and mood disorders are another class of neurological disorder which are very common and extremely debilitating. Nearly half of all Americans will suffer from a psychiatric disorder in their lifetime (*5*), with the two most prevalent being anxiety disorders (29%) and major depressive disorder (MDD) (17%). MDD is ranked as the top contributor to years lived with disability, according to the World Health Organization (*6*). A key reasons for this is that MDD is often resistant to current treatments (*7*). It is estimated that three percent of Americans a year (up to 4 million) suffer from treatment resistant depression (TRD), in which traditional therapies provide no improvement to the patient's quality of life (*8*). TRD patients often fail several rounds of antidepressant drug therapies before being referred to electroconvulsive therapy. Patients with TRD are twice as likely to be hospitalized due to their illness compared to non-TRD patients. TRD patients also bear a 6 fold higher heath care cost per year as well (*8*). There is a clear need for improved treatment strategies for patients with TRD.

1.1.2 Pathology of Neurological Disorders from a Circuit Perspective

Recent efforts in neuroscience have greatly expanded our understanding of the underlying pathology of many of these neurological disorders. Neurons in the brain function within circuits to carry out brain functions such as the processing of information, controlling movement, and decision making (*9*). Recent advances in neuroscience imaging and recording technologies have identified abnormal activity across key neural circuits which underlies the pathology of many neurological disorders. These discovery led to a new classification for these neurological disorders,

termed circuit disorders. Unlike conventional diseases in which the pathology is localized to a certain tissue or cell type, the pathology of these circuit disorders exists at the systems level. The symptoms of these diseases arise as a result of failure in the dynamic communication between anatomically distinct areas of the brain (*4*). Many diseases have now been classified as circuit disorders including Parkinson's disease (*10*), depression (*4, 11*), and obsessive compulsive disorder (*12*). In the case of Parkinson's disease it has been suggested that many of the behavioral symptoms are explained by irregular neural activity in the basal ganglia-thalamocortical circuit (*13*). Figure 1-1 shows a schematic drawing of the basal-ganglia circuit that is implicated in PD. One can see that the regions implicated in the disease, are small brain structure which are physically separated from each other.

Recent advances in imaging and neural modulation technologies (e.g. fMRI, dMRI, optogenetics) have begun to further refine our understandings of these diseases, by resolving connections within individual brain structures, such as the striatum (*14*). This work has defined smaller regions referred to as microcircuits. Microcircuitry that is implicated in many disease has been identified including PD (*15*) and mood disorders (*16*).

The focal points within microcircuits have been described as regions with high density of neural connections, with dimensions ranging from 300 μm (*15*) to 1-2 mm in diameter (*17*). This concept presents a major shift in the therapeutic target. In contrast to delivering drug to an entire pathological tissue or organ, as in cancer, the goal is to normalize abnormal activity across the malfunctioning circuit. This can be achieved by modulating neural activity via a stimuli at any link within the communication chain, not just the region of original deficiency. One example of such an approach is high

frequency deep brain stimulation (DBS), which will be discussed in more detail in the following section.

Recent work in animal models has identified specific anatomical regions of the brain that are implicated with many of these movement and mood/behavioral disorders (*15-18*). While the symptoms of these disorders are often very different in appearance, the underlying approach to treatment is very similar between the two from a circuit perspective. The objective is to deliver normalizing stimuli to one focal point in the circuit, which will normalize activity throughout the entire circuit and thus improve the patient's condition. Despite the new insights into the underlying pathology of these diseases, there is a clear need for improved technologies to establish suitable long term treatment in a clinical setting.

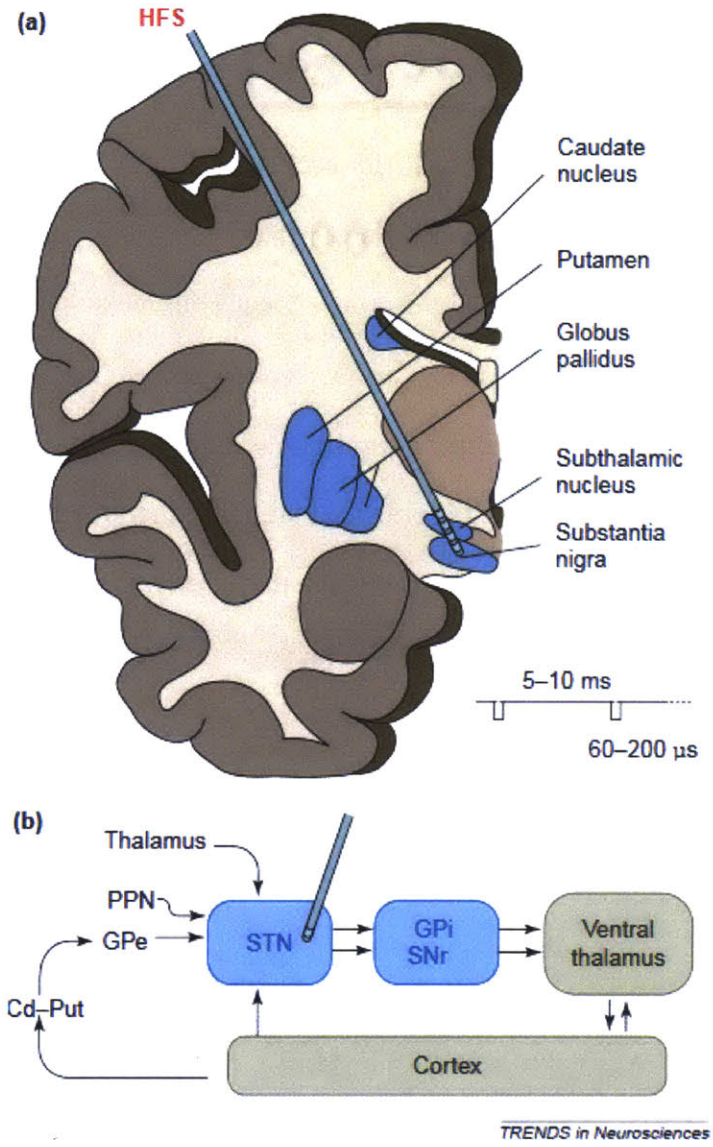

Figure 1-1 Schematic Diagram of the Basal Ganglia Circuit in the Brain.
Disfunction in the communication of anatomically distinct regions of the brain underlies the pathology of many neurological disorders, termed circuit disorders. The regions of the brain associated with the Basal ganglia circuit are shaded blue in this figure. The degeneration of neurons in the Substantia nigra leads to a decrease in dopamine concentrations in the striatum (Globus pallidus and Putamen). This reduced concentration leads to the mood and behavioral symptoms associated with the disease. Effective treatment for neurological disorders may be achieved by focusing treatment to any point within the implicated circuit. A potential location for effective high frequency deep brain stimulation (DBS) is indicated in the picture. Figure was adapted from (19).

1.2 Current Standards of Care

1.2.1 Systemic Delivery

The first pass at therapy for neurological disorders is nearly always some sort of systemic pharmacologic treatment (intravenous or oral), due to the low barrier of administration. When thinking of these diseases from a circuit perspective, however, it is not surprising that these treatments are often not successful.

The current standard of care of PD patients is systemic levodopa (L-Dopa) therapy. L-dopa is a dopamine precursor that is metabolized by the enzyme dopa-decarboxylase to form dopamine in the body. L-dopa is administered as it enters the brain tissue much more effectively than dopamine. L-dopa is metabolized to form dopamine once in the brain. L-dopa is typically administered with a peripheral dopa-decarboxylase inhibitor, carbidopa, which increases the bioavailability of L-dopa 4-fold (*20*). Carbidopa is prevented from entering the CNS by the blood brain barrier (BBB). Dosing regimens of L-Dopa therapy inevitably become less effective and increasingly complex over time. Up to half of all patients taking L-dopa for PD treatment experience motor symptoms and drug induced side effects such as dyskinesia after five years of treatment (*20*).

Several factors contribute to systemic delivery failing for many neurological disorders: off target effects, poor tissue penetration due to the blood brain barrier, and improper delivery kinetics.

Systemic drug delivery (i.e. oral, intravenous or intramuscular) of neuromodulatory drugs is a very inefficient mode of delivery from a circuit perspective. A large portion of the administered drug is going to other tissues and parts of the brain where it is not needed. Furthermore, the receptors located on cellular membranes that are the targets of these drugs are found throughout the central nervous system and peripheral nervous

system. This leads to dose limiting side effects and further limits the therapeutic efficacy of the drug treatment (*21*). Many potentially novel and useful treatments have been thrown out for this reason alone. Secondly, the blood brain barrier (BBB) prohibits many potentially viable therapeutics from being considered due to poor penetration into the brain. The BBB is composed of tight endothelial junctions formed by cerebral microvessels which separate systemic blood flow from the brain microenvironment. The tight junctions in the BBB form a seamless surface preventing a majority of molecules from entering the brain vasculature (*22*). The BBB leads to an 8 log difference between the permeability of the liver and brain capillaries (Figure 1-2) (*23*). The BBB is a rigorous barrier through which molecules only pass through specialized mechanisms. Highly lipid, low molecular weight molecules can pass by diffusion through lipid membranes. Other vital nutrient molecules such as glucose or amino acids pass the BBB via specialized transport mechanisms (*22*). Strategies of improving a systemically administered drug's ability to cross the BBB include receptor mediated transport (*24*), chemical modification of drugs (*25*), and hyperosmotic BBB disruption (*26*). Even in ideal cases, systemic approaches are still hindered by the fact that the entire body acts as a sink and systemically administered drugs go to all tissues. Only approximately 1% of an ideal drug which readily crosses the BBB will end up reaching tissue target tissue in the brain due to this sink effect (*23*). Any effort in improving the delivery of drugs to the brain through systemic approaches will have to accept this inherent obstacle. The maximum tolerated dose (MTD) of many drugs is often limited by the toxicity on normal tissues outside of central nervous system.

Systemic administration of drugs to treat neurological disorders provides course temporal resolution which does not adequately match the rapid dynamics of neural circuits. It is difficult to achieve and maintain the proper therapeutic concentrations for

extended periods of time. Over 60% of PD patients experience issues in treatment due to delays in the drug reaching effective concentrations in the striatum after ingesting a dose of levodopa (*27*). Many patients also experience movement side effects, such as diskenesia, due to the drug concentration half-life shortening overtime (*27*). Similarly, systemic administration of drugs to treat mood disorders by modulating neurotransmitter concentrations has only been moderately successful and is typically accompanied with a wide range of debilitating side effects (*28*).

In summary, it is very challenging to achieve the proper therapeutic concentrations from a systemic approach, while simultaneously avoiding side effects, for complex diseases such as circuit disorders. Local treatment strategies are a more viable approach due to their precise nature of delivery. The next two sections will highlight two local intervention strategies for the treatment of brain disorders: convection enhanced delivery, and deep brain stimulation.

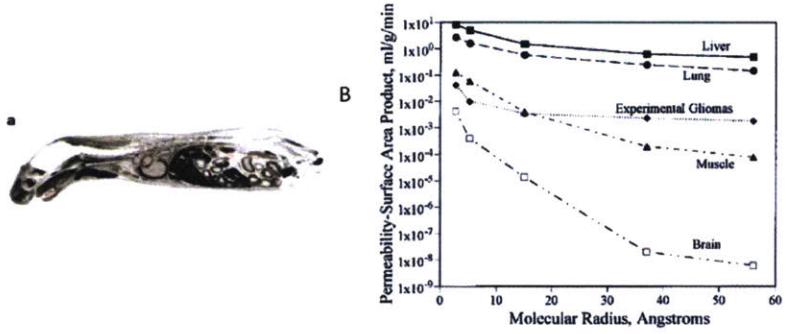

Figure 1-2 The Blood Brain Barrier
A) Illustration of the dramatic effect of the BBB. A mouse was injected with a small radiolabled dye and imaged after 30 minutes. The dye had distributed in almost all parts of the body besides the brain (24). B) The relationship between molecular size and capillary permeability for various tissues in the body. Brain tissue as an 8-log difference in permeability compared to liver tissue for a 50 angstrom molecular radius (23).

1.2.2 Convection Enhanced Delivery

Convection Enhanced Delivery (CED) is a method that was first described by Bobo et al. to bypass the BBB and improve the poor passive distribution profiles of drugs in the brain interstitium (*29*). CED involves inserting a catheter directly into the brain and infusing drug solutions which are driven by an external pump. The convection from the infusion greatly supplements diffusion resulting in larger distribution. CED can produce concentrations of drug that are 100 fold greater than systemic administration (*29*). The use of CED to treat CNS disorders including glioblastoma multiforme (GBM) has been thoroughly investigated over the past 15 years (*30-32*). These studies have reinforced the main advantage of CED which is to provide an increased distribution profile compared to systemic approaches. Catheter based delivery provides much finer temporal control compared to systemic approaches. Control of the infusion parameters (flow rate, duration, location, infusate viscosity etc.) provides adjustable control over the total drug distribution achieved by CED.

CED has not yet been readily adopted for clinical use due to several critical drawbacks of the approach. The greatest issue concerning CED is it that distribution profiles are often non-uniform (Figure 1-3). This is largely a result of the brain tissue being heterogeneous and having anisotropic hydraulic resistance properties. The drug tends to follow paths which provide less resistance to fluid flow such as white matter tracts, previous infusion paths, or back along the catheter (*33*). The high pressure associated with CED has a tendency to disrupt tissue around the catheter increasing the risk of backflow along the catheter. Other complications include brain edema resulting from the high volumes and pressures associated with the technique (*33*). Despite the drawbacks associated with CED, catheter based drug delivery remains a potential approach to deliver therapeutics directly to the CNS. The external control that comes

with catheter drug delivery can achieve complex release regimens that are not achievable with controlled release polymer implants. Control of the infusion parameters provides robust control over the region that receives therapeutic dose of chemical. Stereotactic implantation procedures make accurate targeting of precise brain regions possible. These potential benefits make catheter based delivery a viable strategy to treat disorders which require therapeutic drug exposures in targeted regions of the brain. Circuit disorders are one class of diseases which could benefit from a drug delivery strategy with precise temporal and spatial control. Recent studies have shown that small CED infusions of non-diffusible excitatory neurotransmitters can provide long-lasting seizure protection for periods of weeks to months (*34*).

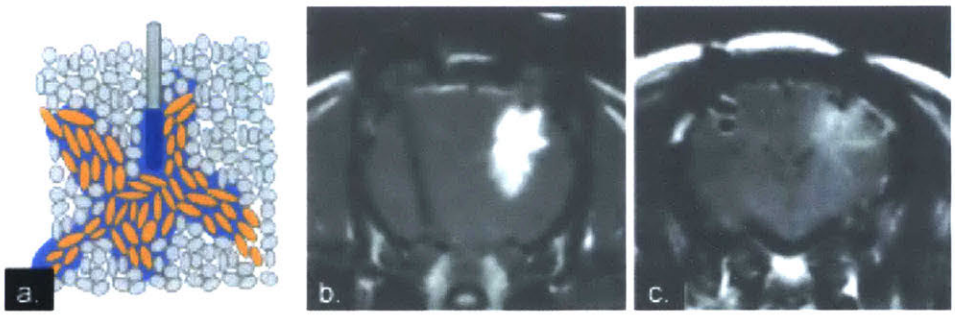

Figure 1-3 Convection Enhanced Delivery to the Brain
A. Sketch illustrating the irregular distribution resulting from CED infusion. The high pressure associated with the technique influences the drug to preferentially follows white matter tracts (illustrated in orange). B, C) T1 weighted MRI image after infusion of Gd-DTPA into pig brain. The infusion pattern has an irregular shape due to motion along lower resistance white matter tracts. (33)

1.2.3 Local Electrical Modulation (Deep Brain Stimulation, DREADDs, Optogenetics)

Deep brain stimulation (DBS) is a treatment strategy in which an electrode is implanted in a specific region of the brain, and high frequency stimulation is applied to modulate the local neural activity. The electrode is targeted to a specific region of the brain, which is implicated in the circuit disorder. The objective is to normalize the activity across the entire circuit through the local activation of neural cell bodies and fibers of

passage. DBS was approved by the FDA in 2003 for electrical stimulation to the STN and GPi for the treatment of PD. While the exact mechanism of action for DBS is still being elucidated, the efficacy of DBS is well documented (*35*). Over 20000 patients worldwide have been implanted with stimulators for the treatment of PD, with a vast majority experiencing a drastic improvement to their quality of life. The now widespread use of DBS in the treatment of PD demonstrates the value in localized, focal treatment strategies for the treatment of circuit disorders. The use of DBS for the treatment of other neurological disorders, including mood disorders, has also shown great potential. Studies have suggested DBS may be beneficial for patients suffering from other severe neurologic disorders including TRD (*4, 11*), severe anxiety (*17*), and obsessive compulsive disorder (*12*).

In the past several years, techniques such as optogenetics and designer receptors exclusively activated by designer drugs (DREADD) have been established to provide enhanced control on the local activation of neural activity compared with electrical stimulation. Optogenetics uses genetic engineering techniques to express light responsive ion channels on the surface a targeted neuron population (*36*). When exposed to a specific wavelength of light, the ion channels are activated and thus the local neural activity of the cells is modulated. DREADDS use similar genetic engineering techniques so that certain neural populations express G-protein coupled receptors. These receptors are responsive to otherwise biologically inert small molecules which readily cross the BBB (*37*). Administration of these chemicals IV or IP results in the selective activation of the neurons which express the designer receptor. Both of these techniques provide greater targeting of specific cell populations in that only the neural cells transfected are controlled by the stimuli. Some obstacles associated

with implementing these techniques clinically include the many challenges associated with modifying the genome in in human patient populations (*38*).

1.3 The Need for Improved Local Chemical Delivery for the Treatment of Neurological Disorders

The systems level disruptions that occur as a result of neurodegenerative disorders, such as Parkinson's disease (PD), arise as a result of the loss of a specific population of neurons.. The clinical diagnosis of PD is based on the development of motor symptoms such as resting tremor and bradykinesia which occurs as the result of the loss of dopaminergic neurons projecting from the substantia nigra (SN) to the striatum (*39*). It is estimated that approximately 50%-70% of the dopaminergic neurons in the SN are lost before the patients experience any detectable symptoms (*39*). This corresponds with an 80% decrease in striatal dopamine concentration at symptom onset (*40*). This depression in striatal dopamine concentration manifests itself by disrupting motor and behavior circuits in the patient (*41*).

The first course of action for most Parkinson's patients in Levodopa therapy. L-DOPA, a DA precursor, is delivered systemically along with carbidopa. Carbidopa prevents the metabolism of L-DOPA to DA until L-DOPA enters the central nervous system (CNS). Levodopa therapies are successful in the short term, as they replenish the dopamine supply, however the CNS-wide delivery induces tolerance and off target effects with time (*39, 42*).

The objective of Parkinson's therapy is to restore the deficit in dopamine concentration in the striatum, thus normalizing the abnormal activity across the implicated neural circuits. However, the lack of precise targeting and dose-limiting side effects associated with L-Dopa therapy limit the effectiveness of this approach over time (*27*). Local

neural stimulation techniques such as DBS and optogenetics aim to use electricity and/or light to selectively excite certain neural cell populations (*43*). Due to the loss of the majority of the dopaminergic neurons, successful treatment of neurodegenerative diseases such as PD via electrical stimulation alone may not be successful in severe cases. Considering that dopaminergic neuron loss progresses overtime, long term treatment would likely require the engineering of another cell type which projects to the striatum to achieve adequate dopamine production. Another option would be to selectively intervene at other specific regions within the circuit. However this may require multiple implantations and viral injections to successfully normalize all essential elements of the neural circuit.

A more direct approach to successful treatment of these diseases should involve precise chemical delivery directly to a critical point within the circuit, such as the striatum. Neurons in the brain use a combination of chemical and electrical signals to communicate. Combining electrical and chemical therapeutic approaches would therefore be expected to have great potential advantages compared to either treatment alone in normalizing pathogenic neural circuits. Successful treatment here would require a device that has both precise spatial and temporal resolution to mimic the dopamine concentration dynamics of healthy patient's populations. The device should have be scalable in size so that it can be readily translated from animal models to the clinic.

1.4 The Injectrode: Combined Local Chemical and Electrical Stimulation for the Chronic Treatment of Neurological Disorders

The injectrode is a cannula based device developed in our lab which is designed to provide greater precision in the treatment of circuit diseases by combining local chemical delivery of multiple drugs with simultaneous electrical recording/stimulation. Local treatment is expected to reduce non-specific side effects compared to systemic administration. Local delivery enables a much wider range of drugs and concentrations to be delivered by bypassing the BBB, and avoiding off target effects.

A combined chemical/electrical approach is expected to improve the efficacy of treatment compared to DBS alone. A drug could be administered to increase the excitability of a brain structure, effectively priming the neurons for electrical stimulation and reducing the currents required to stimulate a given area. This reduces the risk of side effects such as unintended neuron activation and tissue damage from high currents (*44*). Drugs with opposing effects (e.g. bicuculline/muscimol to increase/decrease neuron activity respectively) can be administered to normalize circuit activity based on patient need. The recording electrode provides real time feedback on the treatment progress.

The core of the injectrode device consists of a 150 μm multi-lumen borosilicate glass tubing, which is implanted directly in the region of interest in the brain (Figure 1-4). Two lumens are designated for delivery of neuromodulatory drugs with differing effects. The third lumen houses an electrode for stimulation/recording of neural activity. A manifold rests on the skull and facilitates the connection between the individual lumens and wirelessly controlled drug pumps for the precise, on demand delivery of therapeutics. The manifold construction procedure will be described in the next chapter

(section 2.2.2). The injectrode allows for the precise delivery of potent therapeutics directly to the desired site of action. Driving flow via wirelessly controlled precision micropumps enables complex dosing regimens based on patient response and activity.

The injectrode platform was developed to improve upon existing chemical/electrical stimulation devices which were limited in utility due to their design (*33, 45, 46*). One class of devices consists of single-lumen devices in which an electrode is centered within a cannula. These platforms are limited in their ability to only administer one fluid at a time. Switching solutions requires expelling the entire dead-volume of the device into the tissue, potentially leading to overdosing and off target effects. The second class of devices are constructed using microfabrication techniques, and can have multiple lumen and onboard electrodes. The merit of these primarily silicon-based devices is the wide range of functions (multiple solution infusion and electrophysiology) and dimensions that are possible with a single device. The brittle nature of the substrate limits the aspect ratios that can be achieved (5 mm: 200 μm). Silicon-based devices are therefore limited to use in rodent models and are not directly scalable to larger animal models or to clinical applications (*47*).

The injectrode combines the advantages of both classes of devices; the three lumens can be used for any combination of multiple drug delivery, neurochemical sensing, electrical recording, and stimulation. The high aspect ratio and micron scale dimensions of the borosilicate channel ensure that minimal diffusion occurs in the "off" state and that there is a low amount of dead-volume within the device. A summary of the design constraints and advantages of the injectrode platform is presented in Table 1-1.

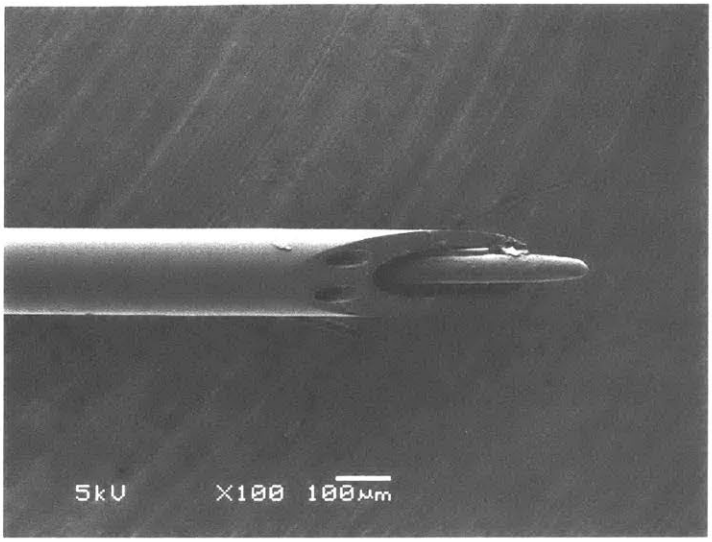

Figure 1-4 SEM Micrograph of the Injectrode Device
The core of the device consists of multilumen borosilicate glass tubing which is implanted to interface with the nodes of neural circuits. The two smaller 35 µm channels are designated for drug delivery, while the third channel houses an electrode for monitoring and stimulation of the local neural activity.

Ideal Treatment Objective	Device Design	Design Benefits
High Spatial + Temporal Resolution	• **Rigid fluidic channels** • **Micron-scale channels**	• **Targeted delivery to circuit nodes.** • **Limited diffusion leak from the device.** • **Enables "on" and "off" state**
Translatable Design	• BS channel has scalable length	• Sufficiently rigid to target deep brain structures • Small and large animal models without change in design
Multimodal Stimulation	• **Multiple lumens in device** • **Electrode for electrical stimulation**	• **Drugs with opposing effects can be delivered to fine tune neural activity** • **Synergies between electrical and chemical delivery**
Guided treatment	• On board electrode	• Local neural activity to guide treatment and assess drug function
Chronic Functioning	• **Mechanically matched hydrogel coatings.** • **Wireless pumps**	• **Minimize scar formation to ensure long term device function.** • **Wireless pumps enable treatment in awake, behaving rodents.**

Table 1-1 Design Features of the Injectrode Platform
This table highlights the critical design features of the injectrode platform and a comment on their utility.

1.5 Thesis Structure

The work presented in this thesis will describe the progress that has been made towards establishing a chronic local treatment strategy for the treatment of circuit disorders. It is essential to have a chronic functioning system capable of high resolution delivery of therapeutics on demand to effectively treat neurological diseases. The work presented in this thesis investigates several key materials issues associated with establishing a chronic functioning platform in the brain. The first portion of the thesis will characterize the fluidic and electrical operation of the device on acute and chronic timescales. The ability to modulate animal behavior through the local intervention of neural circuits will be presented.

Additionally, a successful implantable treatment device must operate as intended for months to years following implantation. The second portion of the thesis will address the topic of glial scarring, the biological response to implants in the brain from a materials perspective. The work presented in this portion of the thesis first seeks to understand mechanical factors that are thought to drive scar formation response around neural implants, and then proposes a potential solution to modulate this response. These findings will provide a strategy to improve the biocompatibility, not only for the injectrode platform, but for all conventional neural probes going forward.

Chapter 2 will focus on the validation of the drug delivery aspects of the device design in both *in vitro* and *in vivo* animal models. PET imaging, chronic impedance spectroscopy, and rodent behavioral testing are used to validate proper device function following chronic implantation.

Chapter 3 will explore the effect that mechanical micromotion has on glial cells in the central nervous system. This was conducted by establishing a novel 3D *in vitro* glial scar model.

Chapter 4 investigates the ability to reduce scarring around the device using a materials based approach. Soft hydrogel coatings are used to improve the biocompatibility of neural implants, by mitigating the effects of micromotion induced strain around the device. Experiments are highlighted which characterize the mechanical and geometric effects of these coatings in tissue phantoms, as well as in a rodent implantation model.

Chapter 5 summarizes the findings presented in this thesis and proposes potential future directions for the project.

2 *IN VITRO* AND *IN VIVO* CHARACTERIZATION OF THE INJECTRODE DEVICE

2.1 Introduction and Motivation:

As discussed in Chapter 1, the injectrode is a multimodal device designed to treat circuit disorders of the brain through combined local chemical and electrical stimulation. The device must be able to dose nanoliter scale volumes of drug, modulate neural behavior, and operate effectively on chronic timescales in order to maximize the effectiveness of ≈Infusions need to be reliable and controllable in order to target small regions of brain tissue on demand. The neural circuit nodes that we are targeting with this device are on the order of 0.5 – 2.5 mm in diameter (*17*). Often times neurons in neighboring regions are known to produce different or opposing effects (*17*). The approximate target drug infusion volume may be determined according to the equation:

$$V_{Drug} = \alpha * V_{Tissue} = \alpha * \frac{4}{3} * \pi * (\frac{d}{2})^3$$

where α is the ECS space volume fraction (typically assumed to be ≈0.2 for healthy brain tissue (*48*)), d is the diameter of the neural target region in the tissue. This equation suggests that 13 nl – 1.6 μl scale volumes of drug should be infused to successfully target these regions (0.5-2.5 mm in diameter). This is desired so that the appropriate neural circuit nodes are targeted, without producing unwanted side effects in nearby tissue regions. The dynamics of neural circuit dynamics are highly dynamic. Therefore it is also critical to be able to have high temporal resolution in the drug delivery process in addition to precise spatial control. There should be minimal effects from drug passive release (e.g. diffusion from the exposed tip) when the device is in the "off" state.

This chapter highlights the work that has been completed to validate the device's ability to accomplish these tasks on acute and chronic timescales. Preliminary infusion tests were conducted *in vitro* and *in vivo* to assess the spatial and temporal characteristics of typical infusion parameters. Electrophysiology experiments were conducted to demonstrate these nanoliter scale volumes of drugs are capable of locally modulating neural activity in a rodent model.

The final portion of this chapter will focus on the chronic operation of the device in a rodent model. Positron emission tomography (PET) imaging was used to quantify infusion volumes and assess device operation at various time points after chronic implantation. Changes in electrical properties of the recording electrode and the local tissue environment were assessed via chronic impedance spectroscopy. As a last proof of concept for the potential of the injectrode platform, we demonstrate behavioral modification through infusion of microliter volumes of drug in a rodent behavioral model.

Throughout these experiments muscimol was used as a model drug. Muscimol is a potent $GABA_A$ agonist, which silences neural activity by selectively binding to the $GABA_A$ receptors in the brain (*49*).

2.2 Methods:

Many established techniques were employed to characterize the operation of the injectrode platform *in vitro* and *in vivo*, on both acute and chronic timescales. Background and procedures related to these techniques are provided in this section.

2.2.1 Materials

Muscimol, heptafluorobutric acid (HPTA), agarose, indocyanine green, and Tris(2-carboxyethyl)phosphine hydrochloride (TCEP) were purchased from Sigma Aldrich (St. Louis, MO, USA). 4-arm Polyethylene glycol was purchased from Creative PEGworks (Chapel Hill, NC, USA). Maleimido-mono-amide-NOTA was purchased from Macrocyclics Inc (Plano, TX, USA). Cu-64 was purchased from the cyclotron facility at Washington University in St. Louis.

2.2.2 Device Fabrication:

The core of the injectrode platform consists of multiple micron scale borosilicate (BS) channels for fluid flow, as well as a larger lumen to house an electrode for neural recording and stimulation. The 1st and 2nd generation fabrication procedures are described below. The implanted core of both device designs are largely identical, with the mode of upstream fluidic connections varying between the two. The 2nd generation device design was implemented to improve device yield and fluidic reliability of the device.

1st Generation Device:

The device design consists of four components: borosilicate glass tubing (Vitrocom, Inc, Mountain Lakes, NJ), a five-piece custom machined manifold, an electrode, and upstream drug reservoirs connected to a microsyringe pump (Figure 2-1A). The borosilicate (BS) tubing is 150 μm in diameter and contains three lumens. Two of the lumens are 30 μm in diameter and are intended for the delivery of neuromodulating drug solutions to the region of interest. The third lumen is larger in diameter (90 μm) and houses an electrode to record and stimulate neural activity, or a carbon fiber electrode to measure local neurotransmitter concentrations.

The manifold is designed to establish airtight fluid connections between the upstream syringe pump and the specific lumens in the glass tube. The components of the manifold are designed and fabricated in house using a micro-computer numerical control (CNC, Cameron Micromaching Center, Sonora, CA, USA) machine. The chambers are separated by the septa. Two of the chambers connect a fluid port to a specific lumen and the middle lumen is designed to prevent leaking between the two fluid channels. Access ports are cut in the glass tubing so that each lumen aligns with one compartment in the manifold. Access ports are made with a precision milling machine and diamond tipped engraver tool so that they intersect with one lumen along the length of the glass.

PE20 tubing (Becton Dickinson, Franklin Lakes, NJ), is connected to each infusion chamber to interface with syringe pumps to drive fluid flow. Devices were tested to ensure proper function prior to experimental use. Quality testing includes infusion of a controlled amount of dye through each lumen and comparison to a calibration curve and visual inspection for any minor leaks.

2nd Generation Device:

Second generation injectrode devices were made by employing microfabrication techniques to improve the production yield and fluidic reliability of the device (Figure 2-1C). The 2nd generation device consisted of a stainless steel guide tube (200 μm O.D., Hamilton Company), two borosilicate fluidic channels (30 μm OD, 20 μm ID, Vitrocom), a tungsten electrode/tetrode for recording and electrical stimulation (FHC, Inc, Bowdoin, ME, USA), and the 150 μm multichannel BS glass tip. Briefly, all components were aligned utilizing a polyimide template constructed in the Harvard cleanroom facility. The components were fixed in place with UV curable epoxy, and then threaded down the guide tube. The tips of the fluidic channels were inserted into a

short 150 μm borosilicate multichannel glass tube mentioned in the previous section that served to align the tips at the end of the device. The two fluidic channels were placed in an individual 35 μm channel and the tungsten electrode/tetrode was placed in the larger channel. The glass tips typically extended approximately 2-3 mm from the guide tube, but is customizable based on the intended application. The length and electrical components (e.g. tungsten electrode, carbon fiber, or tetrode) of the device were chosen based on the intended application and targeted brain structure. Flow from the devices was driven by syringe pump (Quintessential Stereotactic Injector, Stoelting) or wirelessly controlled implantable pumps (iPrecio SMP-300 pump Primetech Corp., Japan). The device fabrication procedure and assembly was established and carried out by C. Dagdiveren, PhD and P. Joe in the Harvard Cleanroom.

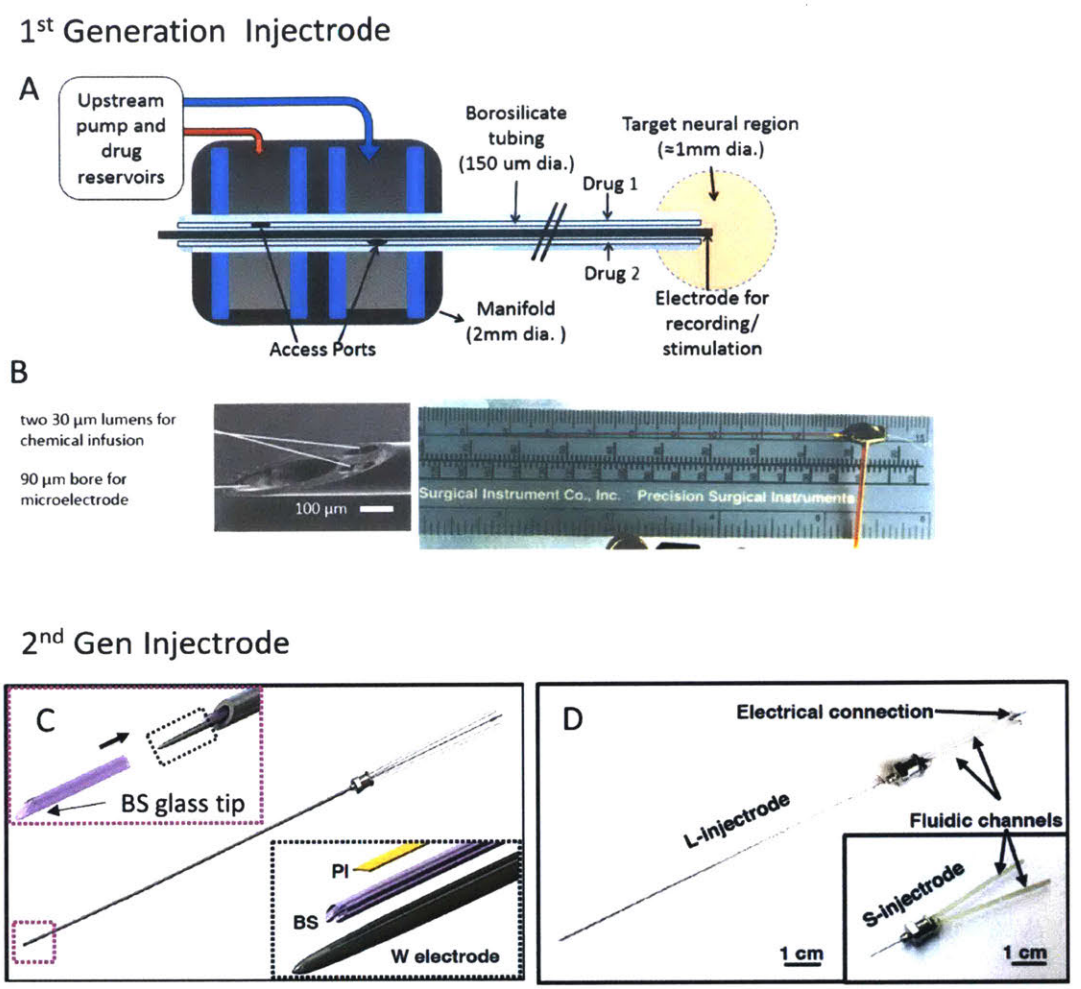

Figure 2-1 Schematic of Injectrode Device Fabrication Procedure
The injectrode core consists of a multilumen borosilicate glass tube. Two lumens are designated for drug delivery to the target neural region, while the larger channel houses an electrode for electrical recording and stimulation. An SEM micrograph of the glass tube is shown in panel B. Fluidic connections were established through a custom machined delrin manifold in 1st generation devices (A), while fluidic connections to radel tubing were established through microfabrication techniques in the 2nd generation devices (C,D). The injectrode devices were threaded through a steel guide tube prior to implantation.

2.2.3 *In Vitro* Device Characterization:

Injectrode devices were attached to a syringe pump and primed with dye/drug containing solution. Devices were primed before beginning the experiment by infusing approximately 1-2 ml of solution through the device. All fluidic lines were visually inspected for air bubbles prior to beginning the experiment. The tips of the devices were lowered into a water bath, and a set amount of dye was infused. Programmed infusion

volumes ranged from 50 nL to 300 nL, as these are volumes we anticipate are necessary to target focal points in neural circuits. The amount of dye which was infused was determined by measuring of the peak absorbance at a given wavelength using a plate reader (Biotek Synergy 2, Winooski, VT, USA) and comparison to a calibration curve. This procedure was conducted with two dyes with distinct absorbance spectra, one delivered through each lumen. The volume of each dye (both the dye infused and the dye in the other lumen) was measured to detect any cross contamination between fluidic channels. Each infusion study was repeated in triplicate.

A similar protocol was used for drug infusion studies. Muscimol (5 mg/ml) was primed in the device, and the total amount of drug infused was quantified via high pressure liquid chromatography (HPLC) (*50*). Briefly, 20 µl of sample was injected into a 4.6 mm (ID) x 25 cm (L) ODS-2 column (Spherisorb, Column Engineering, Ontario, CA, U.S.A) on an Agilent 1200 LC system. The column was eluted with a HPTA 0.5% (V/V%) running buffer at a flow rate of 1 ml/min. The muscimol peak was detected at 230 nm, with a reference wavelength of 360 nm, at an elution time of approximately 8.4 minutes. Known concentrations of muscimol were analyzed to produce a calibration curve. Comparison to this curve enabled the concentration of the drug infusion bath to be determined.

The rate at which muscimol diffuses from the tip of the injectrode when no infusion is programmed was also measured. Devices were primed with muscimol solution (5 mg/ml) and were placed into a water bath. Samples were collected at set time (0-48 hours) points and the drug concentration was quantified.

In Vitro infusion studies were also conducted to assess the capabilities of the iPrecio wirelessly controlled pump. Devices were attached to a pump and placed in a water bath on a precision microbalance (Mettler Toledo, Columbus, OH, USA). The water bath

had a small layer of mineral oil on the surface to minimize the effects of evaporation. The wireless pump was programmed to infuse volumes ranging from 10 nl to 1.67 µl. The amount of fluid infused was determined by monitoring the mass change over time. Dye infusion studies were conducted by B. Masi, PhD, drug infusion studies by K. Spencer, and pump characterization was conducted by K. Ramadi.

2.2.4 Agarose Phantom Infusion

The spatial distribution of infusions was visualized both *in vitro* and *in vivo*. Infusions were conducted into a 0.6% agarose tissue phantom, which is known to resemble the mechanical properties of brain tissue (*51*). Devices were primed with fluorescein and were inserted into the phantom. 400 nL of dye was infused at a rate of 100 nL/min. The trajectory of the dye over time was imaged using an EVOS FL microscope (4x objective, ThermoFisher Scientific, Waltham, MA, USA). Epifluorescent images were taken every 40 seconds for a duration of four minutes. Exposure and gain settings were held constant for the duration of the experiment. The fluorescent intensity as a function of distance from the device tip was quantified using ImageJ analysis software.

2.2.5 Acute *In Vivo* Infusion and Diffusion Analysis via Integrative Optical Imaging

A small craniotomy was made in the rodent skull of an anesthetized animal (+2mm AP, +2mm ML from bregma). Devices were connected to external microsyringe pumps for acute infusion. 1 ul of the near IR dye cardiogreen in PBS (0.5 mg/ml, ICG) was infused at a flow rate of 100 nL/min. The anesthetized animal was then transferred to the IVIS spectrum whole animal imaging system for imaging (Perkin Elmer, Hopkinton, MA, USA). Epifluorescent and transillumination fluorescent images were

acquired. The transillumination images were used to produce a 3D reconstruction of the fluorescent infusion volume using Living Image analysis software.

Integrative optical imaging (IOI) is a method in which a fluorescently tagged molecule is introduced into the brain and the distribution is monitored over time to determine the local diffusion properties of the brain (*52*). The dye distribution is visualized over time and is modeled as a Gaussian point source distribution. Considering contributions from fluorescent molecules out of the focal plane, Nicholson and Tao found that the intensity distribution (I) at time t_i of the fluorescent image is:

$$I_i(r, \gamma_i) = E_i(\gamma_i) e^{-(\frac{r}{\gamma_i})^2}$$

where:

$$\gamma_i^2 = 4D^*(t_i - t_o)$$

By fitting the fluorescent image distribution at multiple times to the equation above, one obtains a linear plot of γ_i^2 vs. time to determine D^*, the effective diffusion coefficient in the brain. The tortuosity, or the degree of hindrance to diffusion that a molecule experiences in the brain, is determined by comparison of D^* with measurements in a 0.6% agarose phantom. The tortuosity is defined as $\lambda=\sqrt{(D/D^*)}$ where D is the diffusion coefficient in free medium, and D^* is the effective diffusion coefficient seen in the brain.

Epifluorescent images were obtained using the IVIS Spectrum live animal imaging system following infusion. Images were taken every 60 seconds for 45 minutes post infusion. Fluorescent intensity line profiles were produced using Living Image analysis software. Line profiles were fit to a Gaussian of the form described above to obtain γ_i^2 using the Matlab curve fitting tool. Linear regression analysis was conducted on a plot

of $\frac{r_i^2}{4}$ vs. time post infusion to obtain a value for the effective diffusion coefficient (D*) in the brain (*52*). Tortuosity values were calculated according to the equation:

$$\lambda = \sqrt{\frac{D}{D^*}}$$

by comparing the values of diffusion coefficients measured in brain and dilute agarose gel.

2.2.6 Acute Electrophysiology Experiments

Adult female rats (F344, 150-175 g) were anesthetized by exposure to isoflurane (2%, mixed with oxygen) and mounted in a stereotactic frame. A craniotomy was performed 2.5 mm posterior and 2.5 mm lateral to bregma. A second craniotomy for the reference electrode was conducted 2.5 mm anterior to bregma. A millmax pin was put into contract with the brain to serve as the reference electrode. Devices prepared with a tungsten tetrode as the electrode component were connected to an electrode interface board (Neuralynx, Bozeman MT, USA). The device was connected to a computer for data recording via an Intan RHD 2000 USB interface board (Intan Technologies, Los Angeles, CA, USA).

The dura was removed and the device was lowered into the brain to a depth of approximately 2.5 mm. The local neural signals were recorded with Open Ephys GUI software. A baseline recording was obtained recorded for 30 mins to ensure the local neural signals were stable. After the baseline recording, 150 nl of muscimol (1.0 mg/ml in saline) or saline was infused into the site at a flow rate of 100 nl/min and the neural activity was recorded for the duration of the experiment. Electrophysiological data was processed offline in Offline Sorter (Plexon Inc, Dallas, TX, USA) to identify single unit activity and in Neuroexplorer to create rate histograms based on these detected units.

2.2.7 Device Chronic Implantation Procedure:

All animal procedures were approved by the MIT Division of Comparative Medicine prior to beginning any experiments. F344 (SAS Fischer) rats were purchased from Charles River laboratories (Wilmington, MA, USA). All materials used in surgeries were sterilized by autoclaving and bead sterilized between animals. Rats were anesthetized with isoflurane (2-4% mixed with oxygen). The head was shaven and disinfected with alternating betadine and 70% ethanol scrubs, three times each. Animals typically underwent bilateral craniotomy. The animal had a device implanted on the left side of the brain and 2-3 ground screws implanted on the right hand side. One ground screw served as the reference electrode for impedance measurements, while the others served to anchor the device in place.

The animals were placed in a stereotactic frame, and a midline incision was made to expose the skull. Two burr holes were created using a dental drill. The ground screw was inserted 3 mm posterior to the bregma and 2 mm lateral to the midline while the injectrode was implanted approximately 5 mm posterior to the bregma and 2 mm lateral to the midline, up to a depth of 8.5 mm, targeting the substantia nigra (*53*). The injectrode and screw were then cemented to the skull using C&B Metabond adhesive (Parkell Inc., Edgewood NY, USA) and Cement-It dental cement (Pentron, Orange, CA, USA). The incision was closed using 5-0 monofilament non-resorbable suture and tissue glue. Custom made caps composed of a 31G stainless steel rod coated with UV-cured epoxy were inserted into the protruding radel tubing, to prevent dust and microbes form entering the fluidic line. Animals were closely monitored during the recovery process. Buprenorphine-SR (1.0 mg/ml) and Meloxicam (2.0 mg/ml) were provided as analgesics to the animals for 72 hours post implantation. For behavioral studies,

multiple iPrecio pumps (primed with muscimol or saline) were connected to the implanted injectrode, and were implanted subcutaneously.

2.2.8 Chronic Impedance Spectroscopy

Impedance spectroscopy is a commonly used method to monitor biotic and abiotic changes at the implant-tissue interface (*54, 55*). This method involves monitoring the impedance of the electrode at a range of frequencies at various times following implantation. Analysis of the complex impedance spectra provides valuable insight into the local inflammatory response as well any changes in the device surface properties (*56, 57*).

Impedance spectroscopy was used to monitor the tissue reaction around implanted devices, and assess changes in the electrical properties of the device. Impedance measurements were made on anesthetized animals by connecting implanted devices, and the ground electrode to an impedance meter (Keysight E4980 A, Keysight Technologies, Santa Rosa, CA, USA). The resistance and reactance of the device was measured at 200 frequencies ranging from 100 Hz to 200 kHz. Impedance measurements were repeated three times for each time animal at a given timepoint point. The impedance was monitored over the duration of implantation for all animals (N=5, approximately 8 weeks). Impedance measurements were also conducted for tungsten electrodes stored in room temperature saline for zero, four, and eight weeks.

2.2.9 PET Imaging Studies

Positron emission tomography (PET) imaging in an imaging modality in which the decay of specialized radiotracers are detected after being introduced into body. The radioactive decay produces two gamma rays produced which are detected by the

imaging system. The gamma electrons move in opposite directions at the speed of light. The simultaneous detection of the gamma particles by an array of detectors in the system enables the location of the positron emitting isotope to be determined. Radiolabled drugs and molecules are commonly used to monitor drug distribution in cancer treatments (*58*). A large advantage of PET imaging is that it provides much greater tissue penetration compared to conventional optical imaging techniques. This enabled the infusion of drugs to deep brain structures to be visualized in a longitudinal manner.

PET imaging was used to assess the chronic drug infusion capabilities of the device. PET infusion experiments were conducted using a G8 PET/CT imaging system (Perkin Elmer) in the Koch Whole Animal Imaging Core. Animals with a chronically implanted device were anesthetized under isoflurane (2-3% mixed with oxygen). The fluidic line was prepared by priming a 31 gauge 25 µl Hamilton syringe connected to radel tubing primed with silicone oil. The end of the line consisted of a 31 gauge blunt needle to directly interface with the device.

The fluidic line was backfilled with approximately 5 µl of the radioactive tracer (Cu64 in 1x PBS, approximately 3 µCi/µl). The line was connected to the fluidic channel and secured in place with UV curable epoxy (Loctite 4305, Henkel, Dusseldorf, Germany). The animal was then transferred to the PET imaging system. A 10 minute baseline scan was conducted prior to infusion. The infusion was programmed via injection pump or iPrecio wirelessly controlled pump. Large volume infusions consisted of a total infusion of 1.0 µl at a rate of 167 nl/min, and small infusions consisted of 167 nl at a rate of 167 nl/min. Programmed infusion values corrected for dead volume in the device (approximately 0.67 µl). Five minute scans were obtained consecutively both during infusion and for 60 minutes post infusion. Control infusions were also conducted in

0.6% agarose brain phantoms. Data was analyzed via Vivoquant software. The infusion site region of interest (ROI) was defined using the connected thresholding tool (10% of maximum intensity). Radioactive intensity was typically normalized to the maximum intensity from infusion to account for differences in the activity level of the infused tracer. All images were decay corrected to the time that the infusion was initiated.

2.2.10 PEG-NOTA Preparation and Cu-64 Labeling

A four armed PEG-thiol (MW 20kD) was conjugated to the chelation agent 1,4,7-triazacyclononane-1,4,7-trisacetic acid (NOTA) using thiol-maleimide reaction chemistry for PET labelling studies. Approximately 20 mg of PEG-thiol was dissolved in 1 ml of degassed PBS. Tris(2-carboxyethyl)phosphine hydrochloride (TCEP, Sigma-Aldrich) was added in 100x molar excess and the solution was equilibrated under N_2 gas for 20 minutes at room temperature to reduce any disulphide bonds. Maleimido-mono-amide-NOTA was then added to the solution in 20x molar excess to the PEG-thiol concentration. The reaction was conducted overnight under N_2 atmosphere at room temperature. The polymer was purified using a Zeba-Spin desalting column (7 kD molecular weight cutoff, ThermoFisher Scientific) prior to chelation with Cu-64.

The PEG-NOTA conjugate was chelated with Cu-64. Cu-64 in PBS was added to the PEG-NOTA solution for a final radioactivity concentration of 18 μCi/μl. The solution was shaken vigorously for 20 minutes at room temperature. The PEG-NOTA-Cu64 complex was then purified via Zeba-Spin desalting column. The total activity of the solution was adjusted to 3 μCi/μl prior to use in PET imaging experiments. The PET imaging experiment was identical to previously described for the Cu64 imaging protocol.

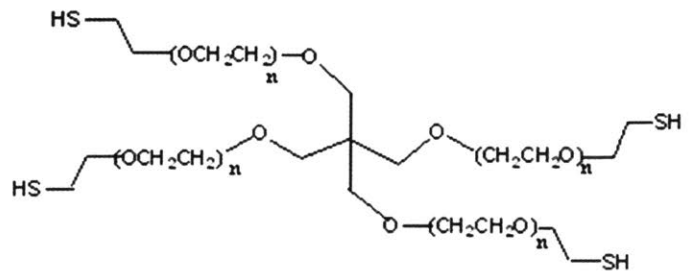

Figure 2-2 Four Arm PEG Thiol Used in Cu64 Labeling Studies

2.2.11 Rodent Behavioral Studies following Unilateral Muscimol Infusion

Animals with chronically implanted devices in the SN and wirelessly controlled iPrecio pumps were placed into a custom made recording chamber ≈30 cm in diameter. Two pumps were implanted – one containing muscimol (0.2 mg/ml) and the other containing saline. The animal's behavior was recorded over time with a GigE digital camera (The Imaging Source, Charlotte, NC, USA). The animal's movement was monitored over the course of approximately 5 hours. No infusion was administered during the first hour to establish a baseline rotation frequency. A saline infusion was then administered (1.67 µl at .167 µl/min) and the animal was monitored for another hour. The other pump then infused muscimol (1.67 µl at 0.167 µl/min). The animal was imaged for another three hours after drug infusion, and then returned to its housing. Videos were imported into Ethovision software (Noldus Information Technology, Wageningen, NL) and the animal's rotation behavior was assessed at different segments of the experiment. A rotation was defined as an 180° turn of the center-nose vector.

2.3 Results and Discussion

2.3.1 *In Vitro* Infusion

In vitro infusion tests were conducted to assess the reliability and reproducibility of infusions in from the injectrode device. It is essential to have precise spatial and temporal control to effectively interface with neural circuits. Therefore both the total volume infused and the fluidic compliance/diffusion of the system were evaluated.

Two different color dyes were infused into a water bath at set volumes between 50-300 nl to assess the ability of the device to controllably infuse nanoliter scale volumes of drug. The data from the dual lumen infusion experiment is presented in Figure 2-3.The measured volumes for each dye are consistent, with standard deviations of approximately 5%. The error observed in this experiment was within the quoted accuracy range for the syringe pumps used in this experiment of 3-5%. This indicates our design does not introduce a large degree of variability in the total volume infused. These experiments show that the device design is capable of isolating the two infusion chambers, and directing each dye to the correct fluidic channel. This ability will enable us to deliver multiple drugs, with opposing effects, to tailor treatment and to the patient's condition at that specific moment.

A

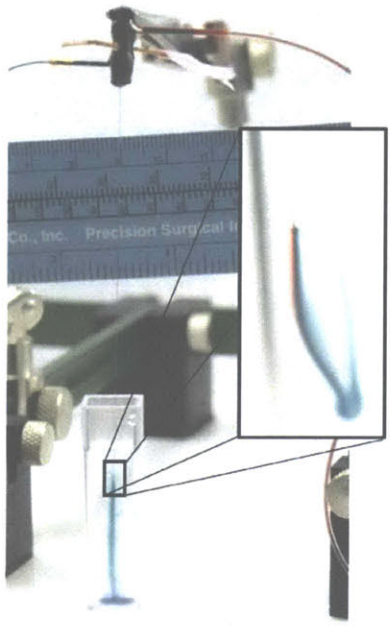

B

Red Dye		
Target Volume (nl)	Average Measured Volume (nl)	Coefficient of Variation (%)
300	305.6	6.6
200	212.5	2.9
100	102.5	2.9
50	59.1	5.1
Blue Dye		
Target Volume (nl) N=3	Average Measured Volume (nl)	Coefficient of Variation (%)
300	262	4.4
200	183	2.5
100	89.1	5.2
50	47.9	2.9

Figure 2-3 *In Vitro* Infusion Data
Multiple dyes with differing absorbance spectra were infused into a water bath and quantified with spectrophotometry. The device was found to be capable of producing reliable infusions between 50-300 nl. (A) An example photograph of the experimental setup during the priming of both fluidic channels. (B) The quantified volume infused as determined by spectrophotometry. Each infusion was conducted in triplicate.

Muscimol infusion experiments were also conducted *in vitro* to confirm effective drug delivery capabilities of the device. HPLC was used to quantify the amount of drug infused into a water bath. The results of this experiment are shown in Figure 2-4. Infusions were found to be reliable and reproducible for programed infusions on this volume scale (50-300 nl). The programmed 50 nl infusion resulted in a measured infusion volume of 50.36 ± 14.4 nl, and the 300 nl resulted in a measured infusion of 301.3 nl ± 5.1 nl. The compliance in the system was tested by changing the amount of time the device was in the water bath after the infusion was complete for a given infusion volume (200 nl). The results of this study are shown in Figure 2-5. There were no changes in the measured infusion volume based on the amount of time the device was left in the water bath. This experiment demonstrates that the device design is such

that there is very little compliance in the system. This is a critical attribute of the device design as it enables the dosing to be turned on and off on-demand based on patient need.

Diffusion leak tests were also conducted. No muscimol was detected in the water bath at any of the time points tested (up to 48 hours). This result highlights another critical aspect of our device design. The small dimensions (approximately 30 μm) of the interface are such that minimal diffusion occurs throughout the system. The amount of drug that is released into the surrounding tissue through simple diffusion is based on both the difference in chemical potential and the surface area of the interface between the device and the water bath. Using a micron scale capillary ensures that the surface area is such that minimal flow occurs when the device is in the "off" state. Furthermore, the hold-up volume of the device is extremely small. On extremely long time scales the maximum amount of drug that is held up in the device (the device dead volume) is 3.14 nl for a 1 cm device, and 30.1 nl for a 10 cm device. This extremely small dead volume is not anticipated to appreciably affect local neural activity, when released over extended time periods (greater than 48 hours).

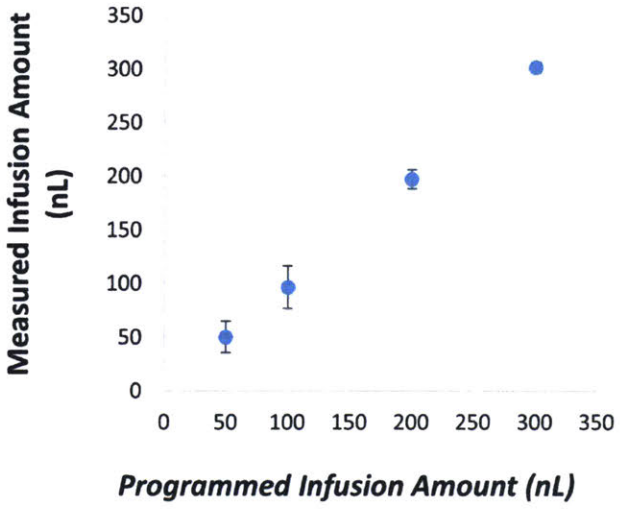

Figure 2-4 Muscimol *In Vitro* Infusion Experiment
Devices were primed with muscimol (5 mg/ml) and then lowered into a 100 µl water bath. Infusions of various volumes (50 nL, 100nL, 200 nL, and 300 nL) were driven at a flow rate of 100 nL/min. The devices were allowed to rest for one minute post infusion before removal from the water bath. The area under the curve of the peak which corresponds to muscimol was quantified. This value was compared to a calibration curve to calculate the amount of drug solution which was infused into the water bath. Each measurement was conducted in triplicate.

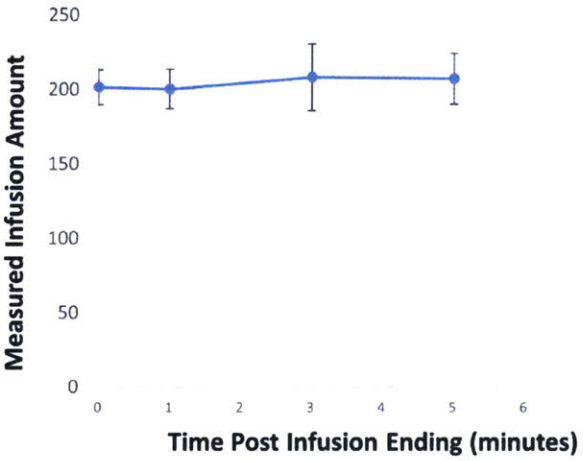

Figure 2-5 Muscimol Infusion Delay Experiment
The amount of muscimol infused after a programmed infusion of 200 nl was quantified to assess the accuracy and compliance in the system. N=3. All data represents mean +/- S.D.

Experiments were also conducted to characterize the infusion profile from wirelessly controlled iPrecio pumps (Figure 2-6). Three infusion profiles at different flow rates (0.1, 1, and 10 µl/hr) and a 10 minute total infusion were investigated, corresponding to infusion volumes, ranging from 16.7 nl to 1.67 µl. Infusions were conducted into a water bath. The total volume infused over time was monitored by recording the mass

change over time, as recorded by a precision microbalance. The wireless pump is capable of producing reliable infusion volumes over this volume range. The total volume infused for the programmed 16.7 nl infusion was 26.3 nl ± 4.8 nl. The total volume infused for the 167 nl infusion was 193.4 nl ± 60.1 nl. The total volume infused for the 1.67 ul infusion was 1.62 µl ± 0.2 µl. These results demonstrate that the use of the wirelessly implantable pump does not affect the performance of the device, or affect the compliance in the system. No additional release was observed after the programmed infusion had ended (after 10 minutes).

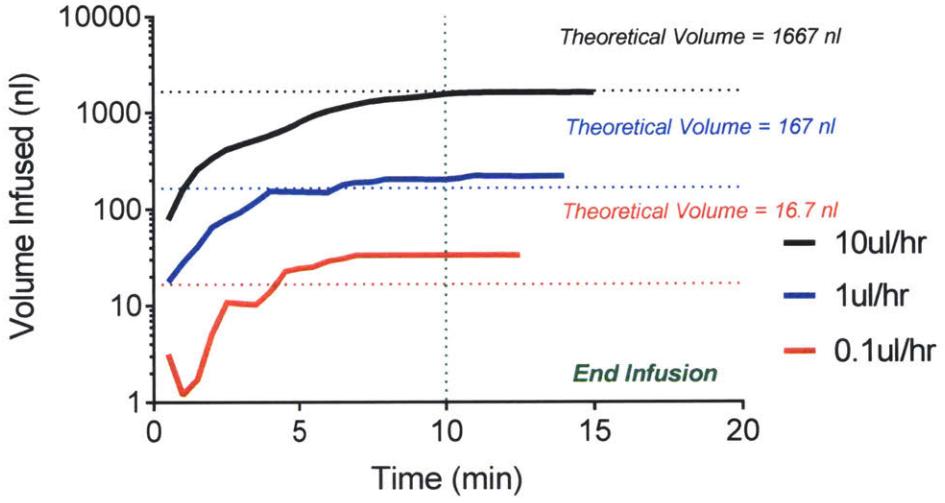

Figure 2-6 *In Vitro* Wireless Pump Characterization
The injectrode device was interfaced with wirelessly controlled iPrecio pumps. In vitro infusion experiments were conducted to assess the accuracy and reliability of the pumps. Various infusion volumes were programmed into the iprecio pumps, and the amount infused was measured by using a high precision microbalance (data was collected by K. Ramadi).

Taken together, these experiments demonstrate that the injectrode platform is capable of administering nanoscale volumes of multiple drugs on demand. The small dimensions and rigid nature of the borosilicate glass capillaries ensure that the infusions have both high temporal and volume resolution, both of which are essential for optimal treatment of circuit disorders. No diffusion occurs when the device is in the "off" state, allowing the dosing to be controlled based on patient need. The use of multiple on-demand

wireless pumps also enable treatment to be conducted in awake, behaving subjects. A proof of concept experiment will be discussed at the end of this chapter (behavioral study).

2.3.2 Agarose Phantom Infusion

Brain tissue phantom experiments were conducted to visualize the spatial distribution of infusions from the Injectrode device. Figure 2-7 depicts the distribution of a 400 nl infusion of fluorescein as a function of distance from the device location at multiple times over the infusion. The fluorescent intensity as a function of distance from the injectrode was quantified using ImageJ analysis software. The fluorescent dye was observed to become distributed over a radius of approximately 0.5 mm from the device lumen. This experiment demonstrates the volume of tissue exposed to the drug can be effectively controlled by both the time infused or total infused volume. Back of the envelope calculation suggests an expected infusion radius of 457 microns which corresponds well with the observed results, assuming a spherical distribution. The tail of the infusion front is likely due to diffusion of the dye that is occurring simultaneously with the infusion in the agarose gel.

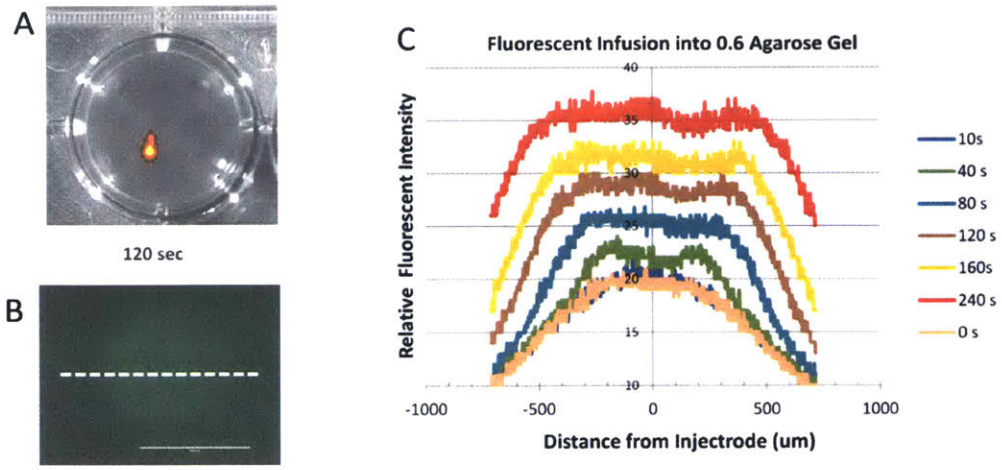

Figure 2-7 *In Vitro* Brain Phantom Infusion
(A,B) Fluorescein was infused (1 µl) into a 0.6% agarose brain phantom and imaged via fluorescence microscopy. (C) Line profiles of the intensity were quantified in imageJ to measure the distribution profiles in the phantom.

2.3.3 *In Vivo* Acute Infusion and Diffusion Measurement

Acute fluorescent infusions were conducted in adult F344 rats to assess the spatial distribution and diffusion properties of solutions introduced into the brain via the injectrode platform. Epifluorescent and transillumination fluorescent images were obtained following a 1 µl infusion of ICG into the striatum (Figure 2-8). The transillumination images were used to produce a 3D reconstruction of the infusion. Measurements of the 3D reconstruction are shown in Table 2-1. The infusion diameter of the fluorescent source was found to be 2.1 mm. This value agrees well with the expected value of 2.2 mm (based on an assumption of an ECS width α=0.2 (*59*). The center of the fluorescent source was found to be 2.4 mm below the surface of the skull. This agrees with the stereotactic coordinates used in the experiment (2mm below the surface of the brain + ≈.5mm thick skull). These results demonstrate that our device is capable of safely infusing a solution to target a specific region of the brain in a rodent model.

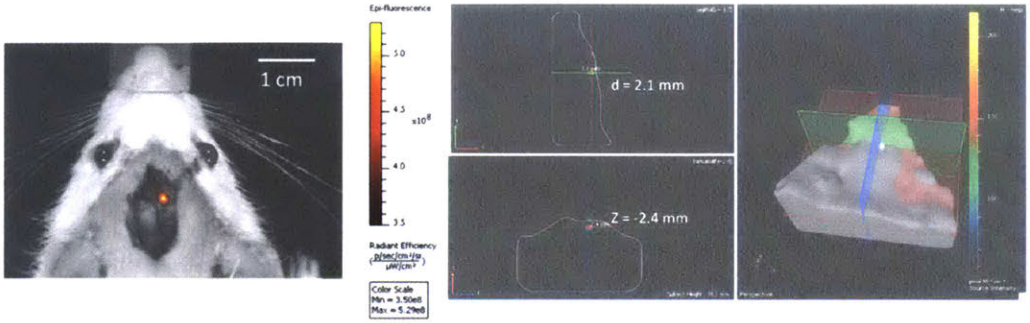

Figure 2-8 Acute *In Vivo* Infusion of ICG into the Rodent Striatum
The IVIS animal imaging system was used to visualize the infusion site in both epifluorescence (left) and transillumination (right) mode imaging. Transilumination mode imaging was used to produce a 3D reconstruction of the infusion site, which was used to determine the depth and diameter of the infusion site. The location and size of the infusion site was quantified using the Living Image analysis software.

	Expected Results	*Experimental Results*
Infusion Diameter (α=0.2)	***2.2 mm***	***2.1 mm***
Depth (.5 mm skull)	***2.5 mm***	***2.4 mm***

Table 2-1 Quantified Infusion Parameters from Acute *In Vivo* Infusion
The infusion diameter and location was quantified using the Living Image software.

The effective diffusion coefficient of the dye was quantified via Integrative Optical Imaging (IOI) (Figure 2-9). Fluorescent images were obtained at set time points following infusion. Line profiles of the fluorescent intensities were obtained, and fit to Gausiann profiles in Matlab. Regression analysis on the values obtained in the fits enabled the diffusion coefficient to be extracted. The effective diffusion coefficient was found to be $8.25*10^{-7}$ cm^2/s. The diffusion coefficient in agarose tissue phantom was found to be $4.5*10^{-6}$ cm^2/s. Comparison of these to values yields the tortuosity, which was found to be 2.3 for the fluorescent dye. The tortuosity (λ) is a factor which accounts for the hindrance to diffusion that takes place in the brain compared to in a free medium. Typical values of λ are about 1.6 in healthy isotropic brain for small molecules

(diffusion in brain tissue is about 2.5 times slower than in a free medium) (*48*). This value is slightly higher than typically observed for small molecule drugs in the brain (typically around 1.6-1.7 (*48*)). One potential explanation for this is that the time scale is much longer in our experimental setup (due to the need for long exposure times to visualize the dye through the skull), compared to typical IOI experiments (60 min vs. 120 seconds) (*60, 61*). Over longer time periods, it is likely that some of the dye becomes internalized and bound to cells. Since diffusion only occurs within the ECS space, these trapped molecules would not undergo diffusion and would thus slow the apparent rate of diffusion.

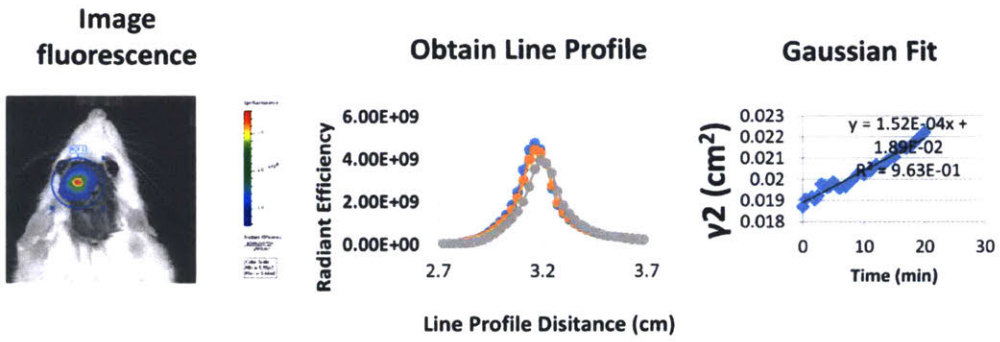

Figure 2-9 Integrative Optical Imaging to Quantify Diffusion in the Brain
Fluorescent images were obtained at set time points following infusion of ICG into the rat striatum. Line profiles of the fluorescent intensities were obtained, and fit to Gaussian profiles in Matlab. Regression analysis on these profiles enabled the diffusion coefficient to be extracted. Comparison between brain tissue and agarose tissue phantom provides an estimate of the tortuosity, or hindrance to diffusion that is present in the brain.

2.3.4 Acute Neural Modulation through Local Infusion of Muscimol

Acute electrophysiology experiments were conducted in a rodent model to demonstrate the ability to modulate local neural activity via focused nanoliter scale infusions. Figure 2-10 shows the results of the muscimol infusion experiment. A well isolated neural unit was located in the rodent hippocampus (CA1). After obtaining a baseline recording, 150 nl of Muscimol (1.0 mg/ml) was infused over the course of 1.5 minutes. The local neural activity was quickly silenced approximately 10 minutes after the end of the

infusion. The local activity was silenced for the duration of the experiment. Musicmol was observed to silence the local neural activity for over six hours, at which point the experiment was ended due to the length of time the animal was under anesthesia. The kinetics of drug activity are similar to previously reported experiments in literature (*62*). Bonnevie et al. found that a 0.24 µl infusion of muscimol silenced local neural units in the hippocampus over the course of approximately 20 minutes and had a lasting effect of greater than 6 hours.

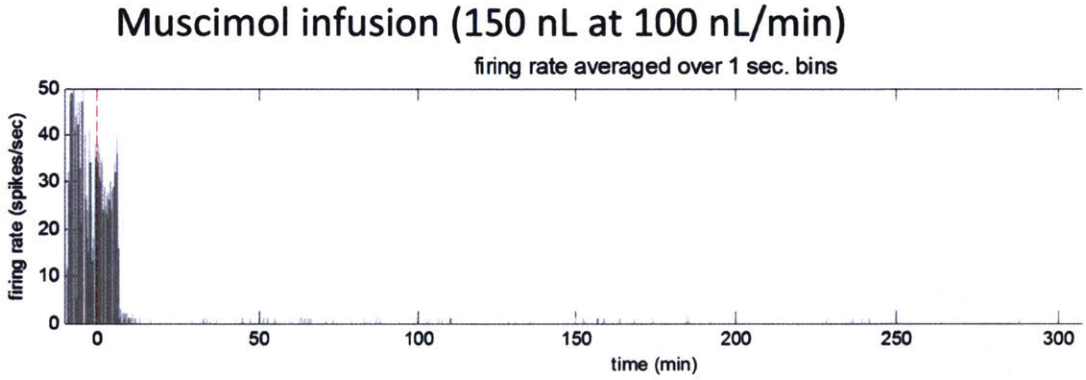

Figure 2-10 Local Neural Activity Silencing following local infusion of Muscimol
The injectrode can modulate and record local neural activity following infusion of a neuromodulatory substance into deep brain structures. Muscimol (1 mg/ml, 150 nl) was infused into the hippocampus of a rodent at time 0 and the firing rate of local action potentials was monitored as a function of time post infusion.

Saline control experiments were also conducted to confirm the infusion did not impact local neural activity (Figure 2-11). The use of tetrodes to record neural signals with our device enabled the neural units to be separated, and their individual waveforms visualized, in a cluster cutting process (*63*). Infusion of saline did not alter the frequency of firing, or the waveforms of the neural units as determined by spike sorting analysis (Figure 2-12).

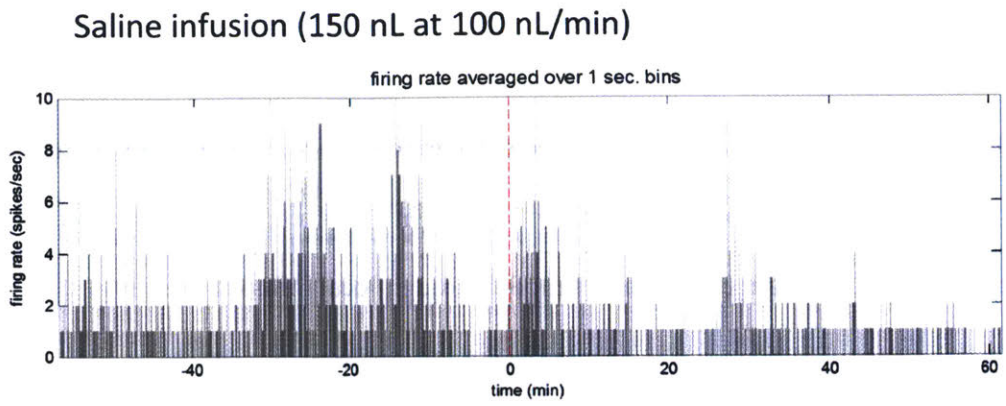

Figure 2-11 Saline Control Infusion Experiment
Local infusion of saline did not have an effect on the local firing rate of neurons in the hippocampus.

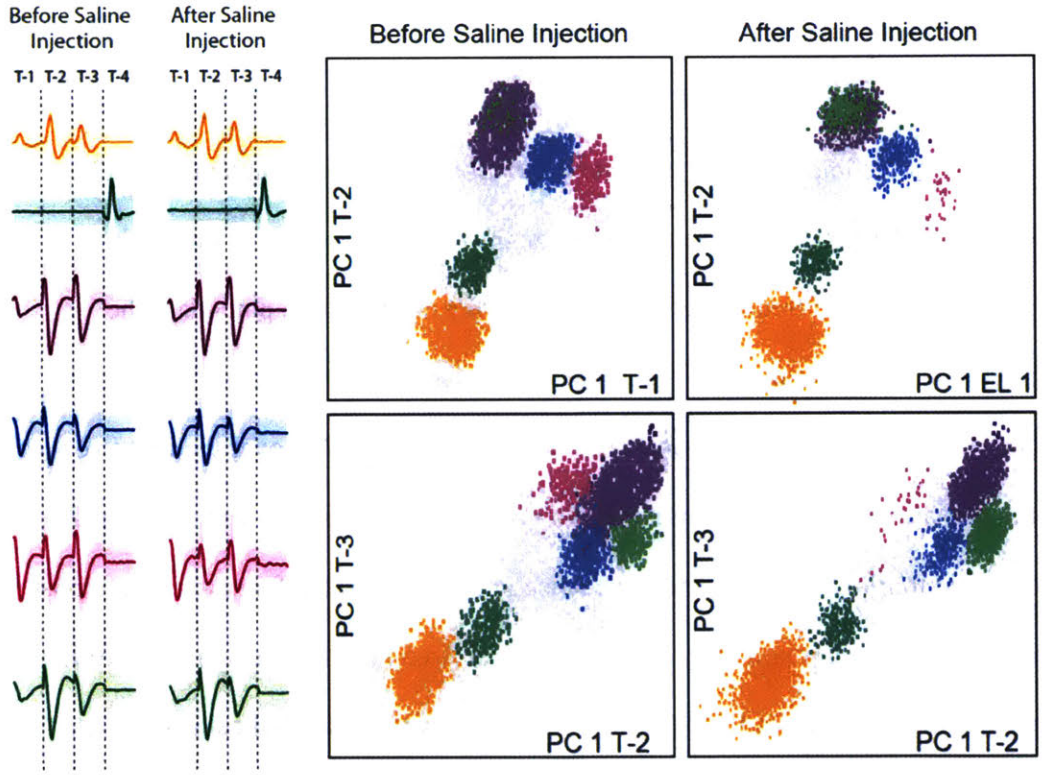

Figure 2-12 Spike Sorting and Isolated Waveforms of Local Neural Activity before and after Saline Infusion
PCA analysis was conducted to confirm that local infusion of saline does not impact the local neural activity. Six well isolated units were located in this study. Local Saline Infusion did not affect the shape or number of the isolated waveforms.

These experiments demonstrate the ability of the injectrode platform to deliver nanoliter scale volumes of drug to locally modulate neural activity. The spike activity was

monitored in real-time using the on board electrode of the device. Different neural circuits or populations of neurons could be targeted by changing the region of implantation and/or the drug that is infused through the device. The behavioral study (section 2.3.7) at the end of this chapter will highlight the potential of this system to produce behavioral changes in a rodent model through local infusion of a drug.

2.3.5 Chronic Impedance Spectroscopy

The chronic reaction to the implanted injectrode devices was monitored via impedance spectroscopy. Animals were implanted with injectrode devices with an onboard FHC tungsten microelectrode (diameter = 75 μm). The impedance was measured from frequencies of 200 Hz to 200 kHz at various timepoints post implantation. Figure 2-13 summarizes the impedance at 1 kHz as a function of days post implantation. The impedance at 1 kHz is a commonly used metric for assessing neural electrode performance, as the frequency is close to that of a neural action potential. The impedance was normalized to the initial value to account for initial differences in electrode properties. The impedance was observed to increase over the first two weeks of implantation. The maximum increase occurred at 10 days post implantation (Z = 2.14 compared to initial values). The impedance remained elevated for seven weeks post implantation (Z approximately 50% higher compared to initial values). This initial increase in impedance is likely due to protein adsorption and glial cells forming a barrier around the device.

After 7 weeks post implantation, the impedance at 1 kHz decreased to approximately the baseline levels, and remained constant for the duration of the implantation. These results are in line with previously reported electrical characterization studies (*55*). Sanker et al. monitored the impedance of 16 channel tungsten electrode microarrays for

200 days post implantation. There was a significant increase in the local impedance (approximately 100% increase in impedance). The impedance was then observed to decrease after approximately 50 days, and eventually returned to baseline. The authors contributed the initial increase in impedance to the tissue reaction around the electrodes. It was confirmed through scanning electron microscopy that corrosion was a main driver to the impedance drop at long time points.

Although the impedance at 1 kHz was similar to the initial values at long timepoints, differences in the electrochemical spectra were observed. Nyquist plots were also produced for each timepoint studied. Figure 2-14 shows representative plots at initial and chronic timepoints. At initial timepoints, the relationship between the reactance and resistance components was linear, indicative of electrode electrolyte impedance dominant behaviour (*64*). At longer timepoints (day 49), there was a shift in the observed behavior, in which the Nyquist plot resembled a semicircle behavior at higher frequencies. The semicircle behavior is representative of capacitance being present in the RC circuit, and is likely due to formation of a glial scar capsule around the implant at long time points(*56*). The tail observed at low frequencies is indicative of a transition to a regime in which the charge transfer is controlled by diffusion (Warburg Impedance) (*64*).

In vitro saline control experiments were also conducted to further elucidate the effect of corrosion on our observed *in vivo* behavior (Figure 2-15). The impedance of electrodes stored in saline were measured at 0, 4, and 8 weeks. The electrodes were observed to have a significant decrease in the impedance at 1 KHz. The average impedance at 1kHz of the electrodes dropped from 300 kΩ to approximately 25 kΩ. The results of the saline control experiment further demonstrate how the tungsten electrodes are susceptible to corrosion, which leads to a decrease in impedance after the initial

increase due to the tissue reaction. Future device designs should incorporate Pt/Ir electrodes which are documented to have less change in impedance over time due to an increased resistance to corrosion (*65*).

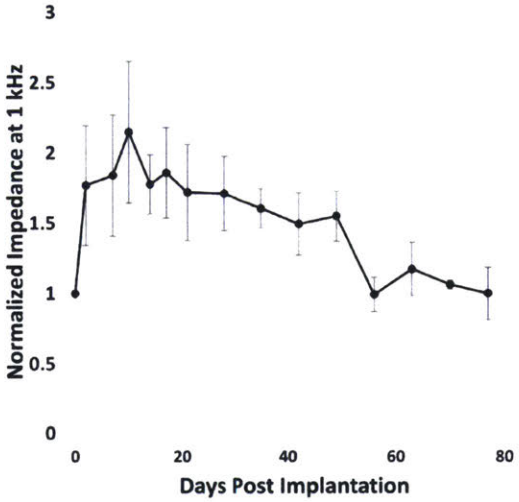

Figure 2-13 Impedance Spectroscopy Results
Normalized Change Impedance at 1kHz around Implanted devices as a function of days post implantation. The data shown represents the mean +/- standard error of the mean. N=5.

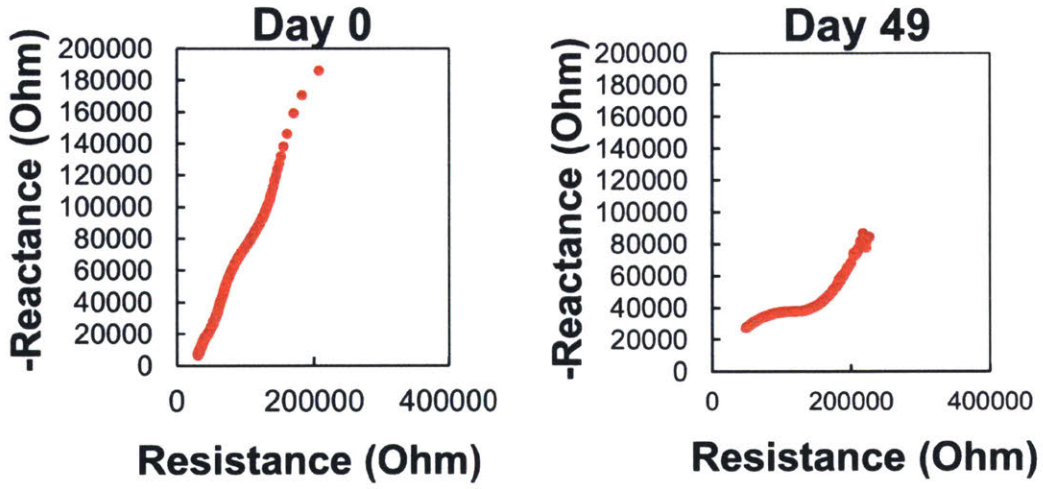

Figure 2-14 Nyquist Plot Behavior at Acute and Chronic Timepoints
The impedance spectra exhibit changes in behavior depending on the time implanted. These plots show representative Nyquist plots for the electrical impedance study. Each point on these plots represent the real and imaginary component of the impedance for a given frequency value in the impedance sweep.

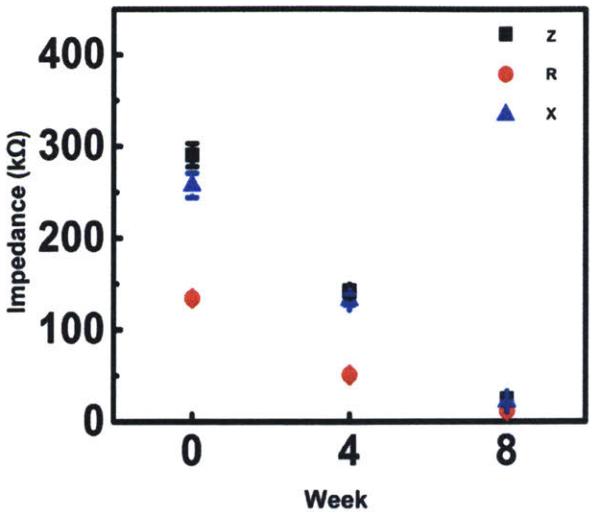

Figure 2-15 *In Vitro* Saline Impedance Measurements.
Devices were stored in 0.9% saline at room temperature for 8 weeks. The impedance was measured using a procedure identical to the in vivo measurements. The impedance at 1 KHz is shown at zero, four, and eight weeks.

2.3.6 PET Imaging of Chronic Infusions

2.3.6.1 Volume Analysis (small and large infusions of Cu64):

3D PET imaging was used to assess the capabilities of the device to target deep brain structures through local chemical infusion after chronic implantation. Two infusion volumes were investigated: small (167 nl) and large volume (1.0 µl) infusions of Cu64 in 1x PBS were conducted into the substantia nigra of F344 rats. The objective of the initial infusion studies was to confirm proper device function and measure the drug distribution volumes for these two infusion volumes. Prior to infusion studies, a syringe injection was conducted to identify the approximately location of the device tip in the field of view as the entire rat could not fit into the CT scanner portion of the system (Figure 2-16). A PET/CT scan was conducted on the decapitated head to identify the approximate location of the substantia nigra in the field of view of the PET imaging system. These results were used to confirm proper operation of the device in subsequent experiments.

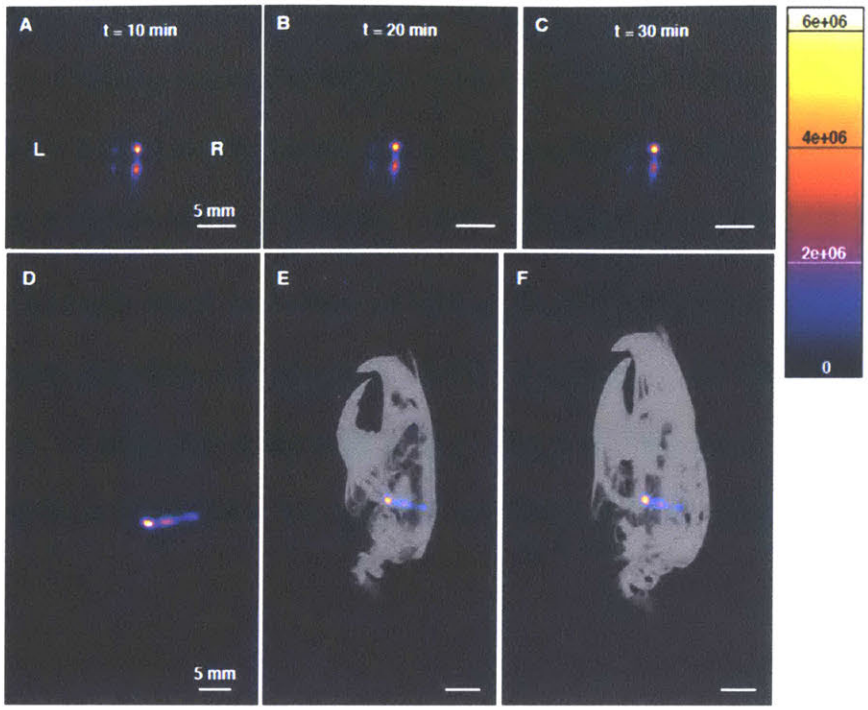

Figure 2-16 Preliminary PET/CT Imaging Experiment to Identify Brain Location in the Field of View.
A preliminary in vitro test was conducted to approximate the location of the the SN in the rodent brain. A craniotomy was performed, and a needle was lowered into the SN. PET/CT scans were conducted to identify the infusion location. Images were obtained at 10 minute intervals (A,B,C). A PET/CT scan on the decapitated head was conducted at the conclusion of the experiment to confirm that the infusion site was within the brain. These experiments served as a guide for future experiments in which CT could not be conducted due to the size of the rat.

Figure 2-17 shows a typical infusion profile for the larger 1.0 µl infusion. Representative images obtained throughout the infusion process, and line intensity profile are shown. The infusion occurred over the first 10 minutes of the experiment. The results from the smaller 167 nl infusions are shown in Figure 2-18. Very little diffusion or clearance occurred in the case of the Cu64 infusion in the brain for both the large and small infusions. We believe this is due to the positively charged Cu64 tracer interacting with cells and ECM proteins, so that no diffusion occurred after infusion.

No significant differences were observed between the infusion profiles resulting from syringe pump and wireless iPrecio pump. Table 2-2 summarizes the measured bolus volumes for the large and small infusions. The volumes were measured via the connected thresholding tool in Vivoquant. The volumes of drug measured for the large

infusion are in line with expected values based on the volume infused ($V_{expected}$=5mm^3) and expected brain ECS width (α = 0.2). These experiments demonstrate that the injectrode device is capable of targeting millimeter scale regions of tissue in the brain.

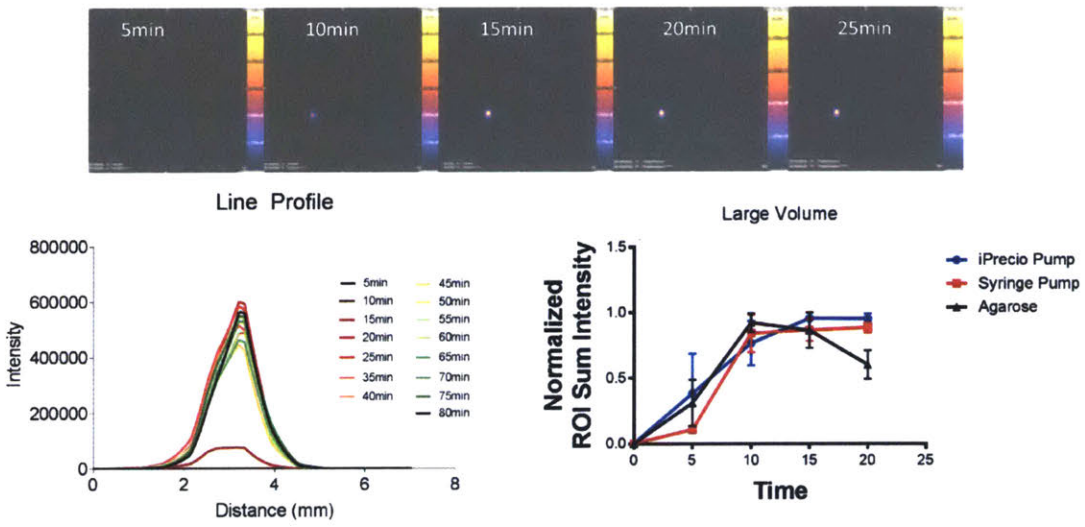

Figure 2-17 PET Imaging of 1.0 µl Infusion of Cu64 into the Rodent Brain
Representative results for the large volume PET infusion experiment. 5 min frames were obtained during and after infusion (shown at the top). Line profile for the infusion are shown. No significant diffusion or clearance occurred following infusion of the Cu64 dye in the brain. The total intensity as determined by ROI analysis was also conducted. Data is representative of three infusions for the iPrecio pump, syringe pump, and agarose phantom infusion.

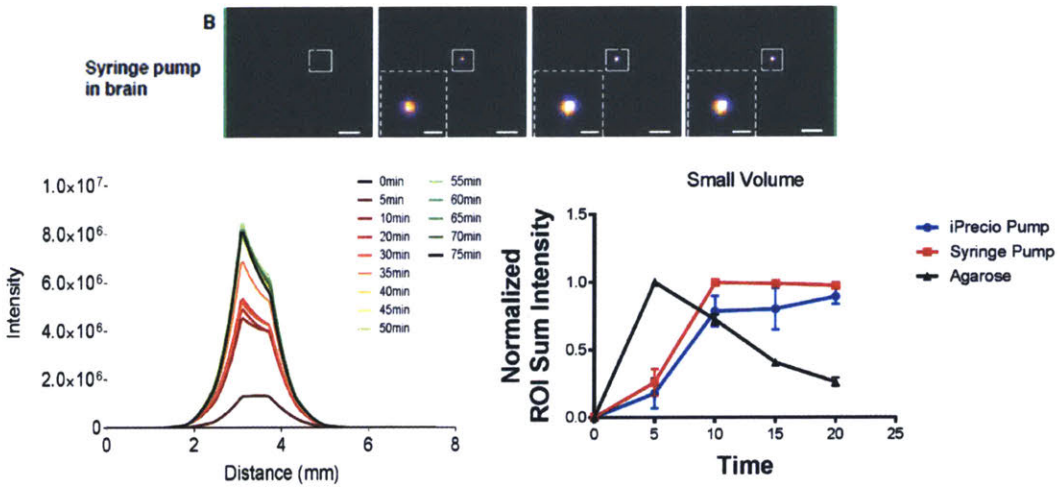

Figure 2-18 PET Imaging of 167 nl Infusion into the SN.
Representative infusion panels from 167 nL infusion. The line profile for infusion into agarose phantom, iPrecio pump into the brain, and syringe pump into the brain are shown (bottom right).

Programmed Infusion	*Large Infusion (1.0 µl)*	*Small Volume (167 nl)*
Syringe Pump in Agarose	***3.78 +/- 2.43***	***2.35 +/- 1.14***
Syringe Pump in Brain	***4.64 +/- 1.43***	***1.84 +/- 0.05***
iPrecio Pump in Brain	***4.36 +/- 0.45***	***2.80 +/- 0.15***

Table 2-2 Summary of Measured Infusion Volumes for Cu64 Infusion Experiments
All values are mm^3. Volumes determined by ROI analysis. N=3 per group.

2.3.6.2 Longitudinal Device Function Assessment:

The capabilities of the device to reliably infuse microliter scale volumes of drug over time was assessed. Figure 2-19 shows the average diameter and volume of the infusion site as a function of implantation time, as determined by analysis of the intensity line profile. There was no significant change in device function throughout the eight week implantation period investigated in this study. The average infusion diameter was 2.2 mm at three days post implantation, and 2.24 mm at five weeks post implantation. The measured average infusion volume, as determined by connected thresholding was also observed to be consistent over the course of device implantation. The measured volume of the infusion site was between 4 and 5 mm^3 for the duration of the implantation. This data demonstrates the reliability of the device, as well as the ability to deliver drugs past any glial scar reaction that has occurred around the device location.

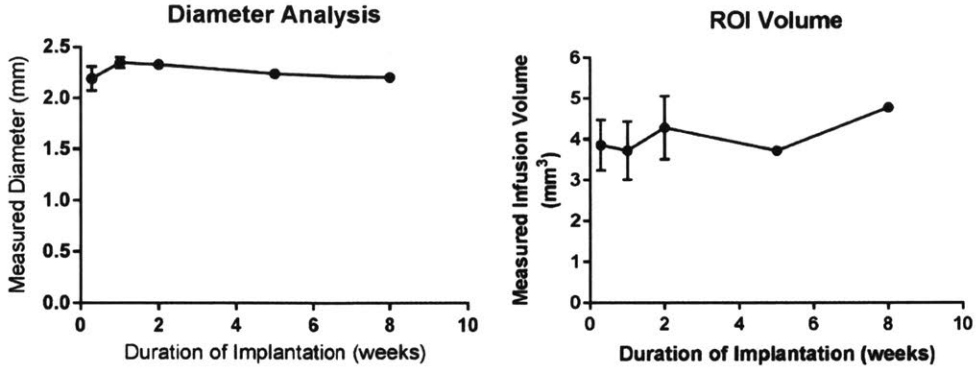

Figure 2-19 Longitudinal Assessment of Device Function
The measured diameter (left) and ROI volume (right) as a function of device implantation time. The diameter was measured by analysing the line profile, and the volume was determined using the connected threshold tool to create a ROI around the infusion site.

2.3.6.3 PET-NOTA Labeling and Infusion Experiments

Cu64 labeled PEG-NOTA were conducted in addition to the Cu64 infusion experiments. Table 2-3 shows the labeling efficiency of the Cu64 labeling process. Approximately 40% of the Cu64 radioactivity passed through the column. No radioactivity passed through the column when no PEG-NOTA was present confirming that all radioactivity infused in this experiment was conjugated to the PEG molecule. 1.67 µl of PEG-NOTA was infused into the substantia nigra. Figure 2-20 shows typical infusion profiles for each radiotracer.

In contrast to the Cu64 infusion studies, PEG-NOTA was observed to spread from the initial infusion site, as well as undergo clearance from the brain. The maximum value of the line profile was observed to decrease from 9.6e5 to 1.7e5 due to diffusion and clearance processes. The region of tissue surrounding the initial infusion site experienced an increase in the radioactive intensity following infusion, suggesting that the tracer spread from the initial infusion site. Figure 2-21 summarizes the average decrease in infusion intensity for three separate infusion experiments. The average half-life for PEG-NOTA in the infusion site was found to be 68.6 minutes.

This experimental setup demonstrates the utility of the PET imaging experiment to monitor drug infusions longitudinally. PET provides great tissue penetration compared to optical techniques, enabling infusions to deep brain structures to be visualized. The specific drug distribution/clearance can be monitored for a specified drug allowing the proper dose/targeting to be achieved in the patient. PEG-NOTA was chosen as the model drug in this case, but any therapeutic molecule could theoretically be targeted and monitored with this approach.

Polymer Concentration	*Starting Activity (μCi)*	*Spin Column Holdup (μCi)*	*After Isolation (μCi)*	*Final Activity Concentration (μCi/μl)*
20 mg/ml	***1270***	***687***	***511***	***6.81***
Control (no PEG-NOTA)	***560***	***513***	***N/A***	***0***

Table 2-3 Cu64 Labeling Efficiency of 4-arm PEG-NOTA

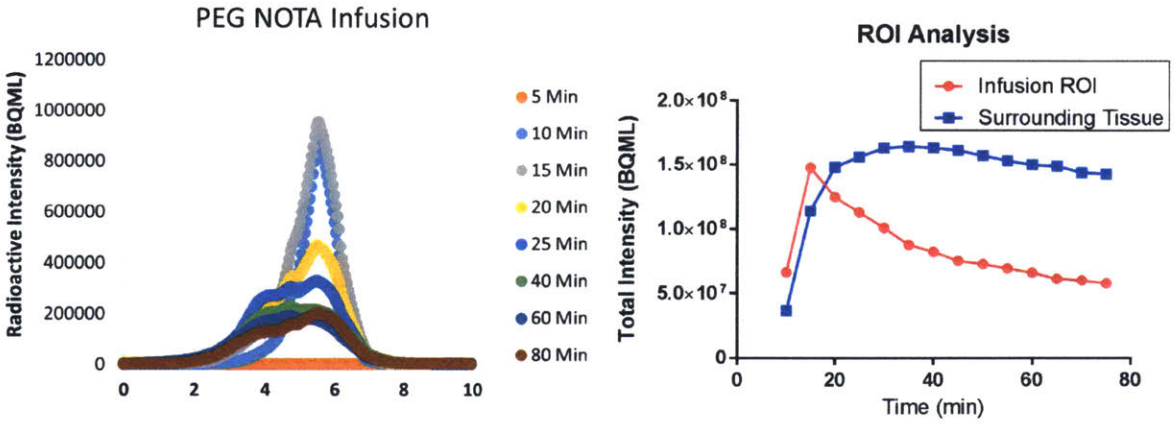

Figure 2-20 Representative Infusion Profile for PET-NOTA Infusion in the Rodent Brain

Line profile for the Cu64 labeled PEG-NOTA infusion is shown on the right. ROI analysis quantifying the total radioactive intensity at the infusion site, and in surrounding brain tissue is also calculated. The radioactivity at the infusion site was observed to decrease as a result of diffusion and clearance mechanisms.

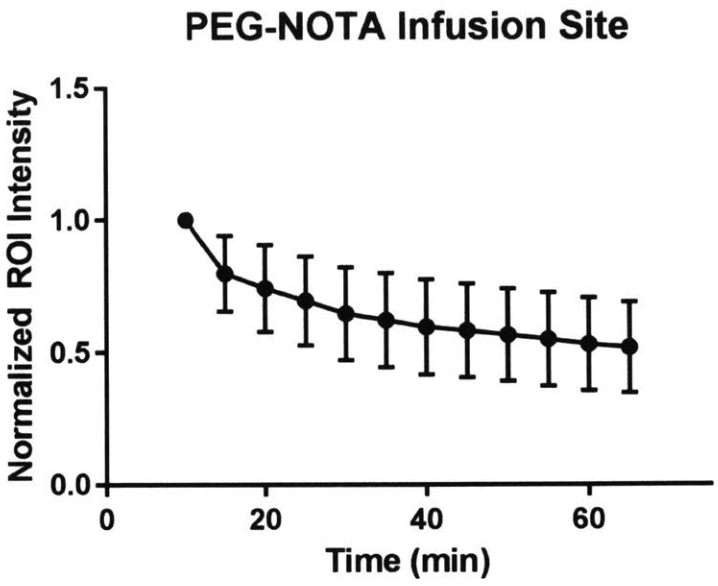

Figure 2-21 PEG-NOTA Infusion Site ROI Analysis
This plot summarizes the drop in radioactive intensity following infusion of 1.67 µl of PEG-NOTA into the brain. The data is normalized to the initial intensity after infusion. The half-life was calculated to be 68.6 minutes. N=3.

2.3.7 Rodent Behavioral Study

Behavioral studies were conducted to demonstrate the ability of the injectrode device to modulate animal behavior through targeted infusion of microliter scale volumes of drug. Animals (N=3) were implanted with injectrode devices that were connected to two wirelessly controlled implantable pumps. The devices were implanted into the substantia nigra in the left hemisphere. Figure 2-22 shows the quantified turning behavior in each of the experimental segments (pre-infusion, post-saline, and post-muscimol). The data is displayed as a rate (turns per 20 minutes) to account for differences in recording time for each of the experimental segments. The number of turns in the clockwise (CW) and counter-clockwise (CCW) directions were roughly equal in the pre-infusion segment. The saline infusion did not have any effect on the animal's behavior. There was a significant change in animal locomotive behavior following the muscimol infusion. The animal showed a much greater tendency to turn

CW compared to CCW. There was a 52 fold increase in the number of CW rotations, and there was no change in the number of CCW rotations.

The results shown here are in agreement with those previously reported in literature (*66*). Unilateral infusion of the GABA agonist Muscimol silences the local neural activity in the substantia nigra. This impacts locomotor control in the rodent for one side of the body, causing the animal to rotate contralaterally, reflecting a Parkinsonian behavior. These experiments demonstrate the ability of the wirelessly controlled system to controllably interface with neural circuits that are implicated in neurological disorders through microinfusion of drugs to deep brain structures. Future work will investigate device operation in rodent disease models for Parkinson's disease (*67*). These experiments will involve infusing dopamine to the substania nigra in 6-OHDA lesioned rodents. Future work is discussed in more detail in chapter 5.

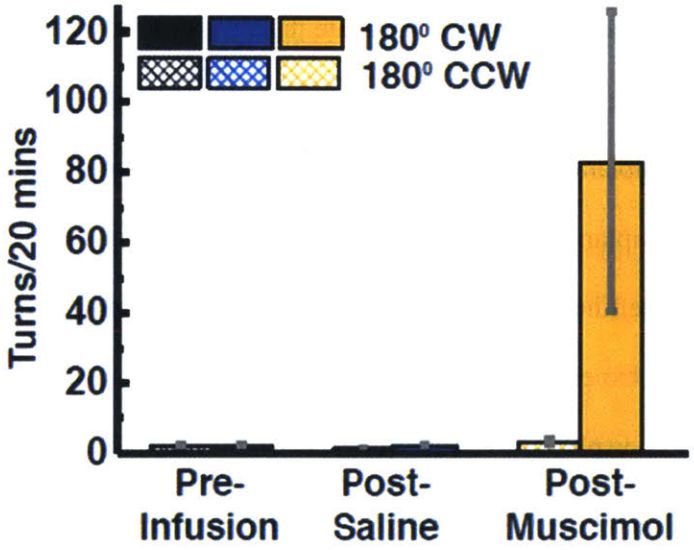

Figure 2-22 Rodent Behavioral Study Results
Devices were implanted into the rodent striatum and interfaced with two wirelessly controlled iPrecio pumps. The animal behavior in an open field chamber was monitored via video recording. No changes were observed after saline infusion. Infusion of muscimol (1.67 ul, 0.2 mg/ml) into the SN had a drastic effect on the animal's behavior. The frequency of counter clockwise turns significantly increased after infusion of muscimol. The number of clockwise turns post muscimol is statistically significant compared to post saline and pre-infusion values ($p<.05$).

2.4 Conclusion

This chapter has highlighted device characterization studies that were conducted to validate the design of the injectrode platform. In order to chronically treat neurological disorders, a device should be able to reliably infuse micron scale volumes of drug on demand to the site of interest. The *in vitro* and *in vivo* infusion studies demonstrate the ability of the injectrode device to reliably deliver volumes of drug ranging from 16 nl to 1.0 µl. Assuming a spherical distribution, these infusions correspond to approximately .5 mm – 2 mm diameter of tissue in the brain. The PET infusion experiments demonstrate that the injectrode platform can reliably delivery multiple volumes of drug to target mm scale volumes of tissue throughout the duration of implantation. The PEG-NOTA studies demonstrate the utility of using this approach the monitor the real time distribution of drugs following infusion into deep brain structures. These experiments are the first known instances of using 3D PET imaging to longitudinally monitor brain infusions. Lastly, this chapter provides evidence on the potential of the injectrode platform to modulate neural circuit behavior through local infusion of neuromodulatory drugs. We were able to silence local neural activity through infusion of the $GABA_A$ agonist Muscimol as shown in rodent electrophysiology experiments. The ability to modulate behavior though local silencing of neural circuit nodes through wirelessly controlled drug delivery in awake-behaving rodents.

These experiments highlight several key material design elements of the injectrode which help to ensure success in the treatment of neurological disorders. The use of rigid borosilicate tubing and non-compliant PEEK tubing ensure that there is no fluidic compliance in the entire system. The small dimensions of the borosilicate channels enables the device to be in the "off state" when no infusions are programmed. This allows the infusions to more effectively interface with the highly dynamic nature of the

neural environment. Another key element is the ability to accurately target precise structures of the brain, such as the substantia nigra. The inclusion of the stainless steel guide tube during implantation ensures that the device is sufficiently rigid so that the device is capable of penetrating brain tissue with minimal deflection occurring.

3 THREE DIMENSIONAL *IN VITRO* GLIAL SCAR MODEL TO PROBE THE EFFECTS OF MICROMOTION AROUND NEURAL IMPLANTS

3.1 Introduction and Background

Implantable neural implants are being developed for many applications including the treatment of neurological disorders, control of brain machine interfaces, and to understand the connections within neural circuits (*68*). A universal barrier to the long term success of these implants is the formation of glial scar around the implant, in which reactive astrocytes surround and isolate the device from viable neurons, negatively impacting device function. Many studies have been conducted to understand the glial scar formation process *in vivo* and are reviewed elsewhere (*69-71*).

A large contributor to the glial scar response is thought to be mechanical factors related to micromotion around the implant. Small displacements of the brain occur due to respiration, vascular pulses, and rotational accelerations and create strain fields around the device (*72-74*). The repetitive motion surrounding the implant is thought to be mostly axial, as it arises from respiration and vascular pulsations when devices are implanted perpendicular to the skull (5). Gilletti et al. measured the magnitude of micromotions present in the rodent skull by placing a displacement sensor on the brain; respiration caused surface displacements up to 30 μm in magnitude, while vascular pulsatility caused displacements up to 4 μm in magnitude. The constant relative motion is thought to drive the chronic response through the constant aggravation of local inflammatory cells. Furthermore, most implants used in experimental animal models are fixed to the skull, thus potentially increasing the magnitude of displacement relative to the brain surface (*75*). Micromotion may also damage local vasculature which can

further drive the inflammatory response through activation of microglia and extravasation of circulating inflammatory cells from the blood, negatively affecting probe function (*76*).

Finite element analyses have modeled local strain fields around neural implants which result from micromotion (*72, 73*). Subbaroyan et al. conducted simulations which showed that the local strain fields, and thus the chronic tissue response, could be drastically reduced by incorporating soft materials into neural implants (*74*). Several studies have been conducted which have aimed to mediate this response by incorporating implant design elements such that the effects of micromotion are reduced. Approaches include incorporating flexible leads (*77*), constructing implants out of flexible materials (*78, 79*), and using novel mechanically adaptive composites which soften when implanted in the brain (*80, 81*).

The performance of these implants is typically evaluated in rodent implantation models. These experiments involve implantation of the devices in the skull and sectioning the brain at various time points post-implantation. Immunohistochemical staining of the sections is used to analyze for inflammatory markers implicated in the glial scar process. These experiments are an essential part of the development process, but are time consuming and costly. The complexity of *in vivo* systems also makes it difficult to resolve inflammatory pathways on a molecular scale and visualize the dynamics of the cellular response. *In vivo* studies also introduce confounding variables such as surgical technique, device placement and large blood vessel damage, and tissue heterogeneity.

In vitro models have been developed over the past decade which have made high-throughput methods possible for assessing neural implant biocompatibility. Initial models involved culturing glial cells on a two dimensional (2D) substrate. Polikov et al. demonstrated that primary glial cells grown in culture exhibit many of the hallmarks of

glial scar formation following mechanical insult (*82*). Astrocytes were shown to increase production of glial fibrillary acidic protein (GFAP), and microglia were found in proximity to a microwire device placed on top of the cell layer or a scrape would. Models such as these are planar in nature and are thus not fully representative of the native environment in the brain.

Recent studies have improved upon this model by constructing three dimensional (3D) growth environments for the neural cells (*83-85*). East et al. demonstrated that astrocytes can be grown in a collagen matrix, and exhibit glial scar characteristics when exposed to inflammatory cytokines (*86*). Another advantage of 3D models, as highlighted by this study, is that glial cells are less reactive in 3D environments, compared to being grown on a 2D, rigid substrate (*86, 87*). This enables a more dynamic range to be investigated within the model, as the glial cells are less reactive at the start of the experiment. 3D architecture supports more representative cell-cell communication and cells show less signs of cellular stress (*88*).

Significant progress has been made towards establishing improved *in vitro* glial scar models. Few have, however, directly investigated interactions between the implant and glial cells. Those that do incorporate neural implants are predominately static in nature, in which the devices are placed in the culture and then analyzed a set time later (*89*). Mechanical stresses in existing models are typically present throughout the whole culture and therefore do not assess device-tissue mechanical interactions (*90, 91*). Any potential mechanical design benefits that the device has to minimize micromotion effects are not captured within such models. Mechanical stimuli have long known to be critical elements tissue engineering applications including vascular tissue engineering (*92*), bone tissue engineering (*93*), and muscle tissue engineering (*94*). The forces present in these systems seek to replicate the *in vivo* environment and have profound

impacts on tissue development and underlying biology in all of these cases. Our objective was to bridge the gap between neural engineering strategies which seek to modulate scar formation through device mechanical factors and existing *in vitro* glial scar models.

In this study, we have developed a novel 3D *in vitro* culture model which produces micromotion around the device. Devices inserted into a 3D collagen matrix are cyclically displaced for one week in culture to simulate axial micromotion. As mentioned above, axial micromotion from respiration and vascular pulsations is thought to be the most chronic contributor to the relative motion of the devices. This culture system will enable researchers to rapidly optimize mechanical design constraints for neural implants prior to beginning *in vivo* studies.

3.2 Materials and Methods

3.2.1 Materials

Poly-d-lysine (PDL), Hoechst 33258, sodium hydroxide, 10x minimum essential media, and lipopolysaccharides (LPS) were purchased from Sigma-Aldrich (St. Louis, MO, USA). Cell culture media, B27 supplement, fetal bovine serum (FBS), antibiotic/antimycotic (anti/anti), Glutamax, normal donkey serum, trypsin-EDTA, live/dead stain for mammalian cells, and transforming growth factor – beta (TGF-β) were purchased from ThermoFisher/Life Technologies (Waltham, MA, USA). Basic fibroblast growth factor (bFGF) was purchased from R&D systems (Minneapolis, MN, USA). Bovine serum albumin was purchased from Rockland Inc. (Limerick, PA, USA). Fluorescent polymer microspheres (6.0 μm polystyrene particles, yellow green) were purchased from Polysciences Inc. (Warrington, PA, USA). Mouse-anti GFAP antibody was purchased from Millipore Inc. (Billerica, MA, USA).

3.2.2 Poly-D-Lysine Coating

T-175 flasks were coated with PDL prior to seeding with primary neural cells. A 50 μg/ml stock solution of poly-D-lysine hydrobromide (MW 70000-150000) was prepared in sterile tissue culture grade water. Approximately 25 ml of solution was placed in the flask and incubated overnight at room temperature. The PDL solution was removed and the plates were rinsed once with tissue culture water. The plates were then allowed to dry before plating cells.

3.2.3 Glial Cell Isolation

Mixed primary embryonic neural cell cultures were established according to a protocol adapted from Liu et al. (*95*). All procedures were approved by the MIT Committee on Animal Care prior to beginning any experiments. Timed pregnant F344 rats (Charles River Laboratory, Wilmington, MA, USA) were euthanized via CO2 asphyxiation followed by cervical dislocation at days E14-E15. The cell isolation procedure was performed in a designated biosafety hood to maintain sterility throughout the process. The dam's abdomen was sterilized with 70% ethanol, and the embryos were removed. Each embryo was quickly decapitated and placed in ice cold sterile hanks buffered salt solution. The brain of each embryo was removed under microscope, and placed in dissection media (DMEM cell culture media mixed supplemented with anti/anti). The midbrain section of the brain was isolated. Large blood vessels and connective tissues were removed with a fine pair of forceps. The dissection media was removed and 0.25% trypsin-EDTA was added to the brains for 5-10 minutes at 37°C once all of the midbrain sections were collected. FBS containing cell culture media was then added to neutralize the trypsin. The brain sections were centrifuged at 1000 rpm for 5 minutes and resuspended in cell culture media (Neurobasal media supplemented with B-27,

glutamax, anti-anti, 10% FBS). Tissue sections were triturated with 10 ml, 1ml, and 0.2 ml pipette tips (3-5 times each). The cell count was then measured using the Countess II Automated Counter (Invitrogen, Carlsbad, CA, USA) and the cell density was adjusted to 1x106 cells/ml. Cells were seeded in T-175 flasks and maintained for approximately 1 week before seeding in 3D culture.

3.2.4 3-D cell culture formation.

Three dimensional mixed neural cell cultures were formed using a protocol adapted from East et al. (*86*). Cells were detached from the T-175 flasks via trypsin-EDTA exposure for 5-10 minutes, and suspended at a density of 3.75 x 107 cells/ml (10x of final concentration). This density was chosen, as it was previously shown to result in maximal cellular viability in 3D neural cell cultures (*85*). The gel mixture consisted of 10% part concentrated cell mixture, 80% parts type-I rat tail collagen (2mg/ml in .01 N acetic acid), and 10% 10x minimum essential medium. The mixture was neutralized with 1 M sodium hydroxide, until the phenol red pH indicator changed to red. The cell mixture was plated into 24 well plates at a volume of 0.6 ml/well. Final gel dimensions were 16.3 mm in diameter, and 2.9 mm thick. The gels typically adhered to the side walls of the plate throughout the course of the experiment. Samples were excluded if delamination from the side wall due to cellular compaction was observed before or during the micromotion experiment.

The gels were allowed to set at 37 °C for 30 minutes, and were then topped with 0.75 ml of media (Neurobasal media supplemented with B-27, glutamax, anti-anti, 10% FBS). Cultures were maintained with 50% media change every 2-3 days. TC multiwell plates were modified with a hole drilled in the side of the plate to facilitate insertion of the neural implants at the start of the experiment. Plates were resterilized by soaking in

70% ethanol and UV light exposure for 1 hour, followed by 3 washes with sterile DI water. Plates were allowed to dry before seeding with cells. The hole was temporarily plugged shut with a polyimide tube sealed with UV medical grade epoxy prior to beginning the micromotion experiment.

3.2.5 Live Dead Cell Staining

Cell viability within the 3D collagen cell culture construct was assessed by using the Live/Dead stain for Mammalian cells. Briefly, calcein-AM (2.5 μM) and eithidum homodimer-1 (2.5 μM) in sterile PBS without calcium and magnesium were added to cultures after 1 week in culture, and incubated for 60 minutes at 37°C. A dead cell control was included by wells to methanol for 30 minutes prior to staining. Stained cultures were imaged via Nikon A1R confocal microscope in the Koch Institute Microscopy Core. Images at 100 μm steps progressing inward towards the center of the gel were obtained at both the top and bottom surface of the gel. The top surface was imaged by flipping the gel after staining. Live/dead cells were manually counted as a function of depth into the gel via ImageJ.

3.2.6 Micromotion Apparatus Construction

The micromotion apparatus was constructed to simulate micromotion within the tissue culture model (figure 1). Custom designed Delrin components were machined using a computer numerical control mill (Cameron Micromachining Center, Sonora, CA, USA) in our lab. The parts served to interface the devices, held in place with a Teflon lined fiber check (Newport Corporation, Irvine, CA, USA), with two high precision linear actuators (Haydon Kirk Motion Solutions, Milford, NH, USA). The linear actuators were controlled by an Arduino microcontroller (see appendix on for electrical configuration and the open source code used for this system). The distance and

frequency travelled for the *in vitro* experiments were chosen to simulate micromotion effects that have been measured in the brain (30 μm, 2 Hz) (*72*). A calibration curve was obtained characterizing the relationship between the programmed number of motor steps and the distance travelled by obtaining images under bright field microscopy.

3.2.7 Strain Field Measurement

A 2.0 mg/ml collagen gel was embedded with fluorescent latex beads (0.05% w/v, Flouresbrite 6 μm). A probe was loaded into the gel and located under an inverted epifluorescence microscope (Zeiss Axiovert 200, Oberkochen, Germany). The device was coupled to the micromotion simulation device. The device was displaced at a frequency of 2 Hz. A series of fluorescent images were obtained throughout the micromotion process.

The images at the extremes of motion were analyzed via the Particle Image Velocimetry (PIV) plugin for ImageJ to construct the displacement fields around the device. Strain fields were obtained in the in/out axial direction for multiple steps (8, 80, and 130 μm). Line profiles were obtained both in the perpendicular and axial directions to the device.

3.2.8 *In Vitro* Glial Scar Experiment

One week experiments were conducted to demonstrate the utility of our in vitro glial scar model. At the start of the experiment, the sealed polyimide tubes were removed and replaced with new, sterile polyimide tubes. Devices were placed approximately 6 mm into the collagen gels. Experimental groups included device with micromotion, device with no motion, positive control, and negative control. Positive control wells were TGF-β (10 ng/ml) and lipopolysaccharide (LPS 10 μg/ml).

The table below (table 3-1) shows an example setup of a typical experiment. Figure 3-1 shows a photograph of a typical experimental setup for the *in vitro* glial scar model. The media was changed to include bFGF (10 ng/ml), which was previously shown to improve the reliability of *in vitro* glial scar model (*96*). The cultures were placed in a 37 °C incubator and were maintained with 50% media changes every other day. The motion wells were examined under microscope, at the beginning of the experiment, and during media changes to ensure that devices were moving as intended within the collagen gel. The 3D collagen gels were fixed with 4% paraformaldehyde in PBS after one week in culture. The gels were washed 3x in PBS, and stored in PBS prior to immunofluorescent staining.

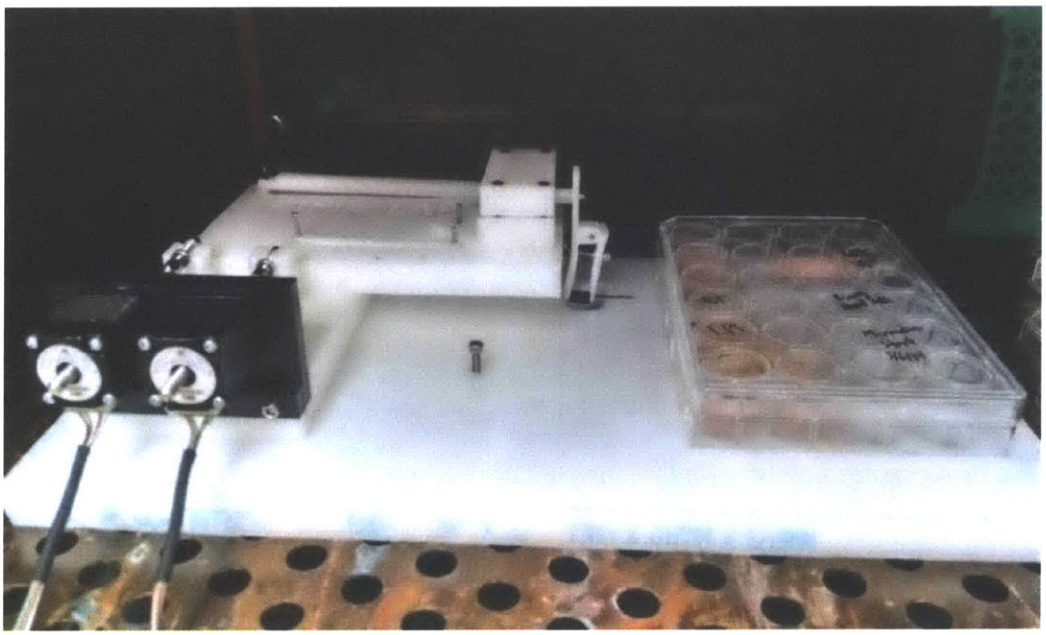

Figure 3-1 Photograph of *In Vitro* Glial Scar Model Experiment in Incubator
Primary neural cell cultures were mechanically stimulated with repetitive micromotion for one week at 37° C.

LPS	LPS	TGF-β	TGF-β	Control	Control
Device μmotion	Device μmotion	Device μmotion	Device No Motion	Device No Motion	Sham

Table 3-1. Example Experimental Setup For *In Vitro* Glial Scar Experiment.

3.2.9 Immunohistochemical Analysis

3D collagen gels were stained for the expression of GFAP after fixation. Gels were transferred to a glass bottom 24 well plate (#1.5 glass, Cellvis Inc, Mountain View, CA, USA) for improved imaging. Fixed gels were permeabilized in 0.5% triton-x100 in PBS for 30 minutes. Gels were washed three times in 0.05% PBS-tween. Gels were then blocked in 5% donkey serum for 1 hour at room temperature, and washed in PBS-tween. Mouse anti-GFAP-AF488 was diluted in antibody incubation buffer (1:300), and the gels were incubated for 48 hours at 4°C to allow for uniform antibody diffusion into the gels. Antibody incubation buffer consists of 1% bovine serum albumin (BSA), 1% donkey serum, 0.3% triton-x, and 0.01% sodium azide in PBS. Gels were washed in PBS-tween three times for 10 minutes following primary antibody incubation. Gels were then counter stained with Hoechst 33258 (2 μg/ml) for 30 minutes. Gels were then washed in PBS three times, and stored at 4 °C in PBS prior to imaging.

3.2.10 Confocal Microscopy

Confocal microscopy was used to analyze the GFAP expression within the gels after immunofluorescent staining. Z-stacks were obtained using the Nikon A1R confocal microscope in the Koch Institute Microscopy Core. 200 μm z-stacks (7.14 μm optical sections x 28 images per stack) were obtained at three different locations within each

well at 10x magnification. Images were obtained in the area directly surrounding the devices, as well as in regions far (≈5-8 mm from the device location) from the device for micromotion device wells. Image exposure settings and resolution were maintained between experimental samples. Images were not manipulated in any way prior to image analysis.

3.2.11 Image Analysis

Maximum intensity projections of the GFAP confocal z-stack images were analyzed via ImageJ. A threshold was applied to the image to define the border between cells and background. The particle analysis tool was used to analyze the size and shape of the cells. All objects with an area greater than 40 μm2 (to threshold for cells) were included in the analysis. Metrics including total object area, total object perimeter per image were measured. A minimum of three images per well was analyzed and averaged to get the total average for each experiment. A total of 9 independent experiments were conducted to obtain the final values for each experimental group unless otherwise indicated.

3.2.12 Statistical Analysis

Observed experimental differences were assessed for statistical significance across all experimental groups through a one-way ANOVA test using Prism 6 (In Stat Graphpad, La Jolla, CA, USA). Post hoc analysis (Tukey's multiple pairwise comparisons test) was performed to compare GFAP size between different groups. Statistical significance was considered $p<.05$. All data presented represents mean ± standard error of the mean unless otherwise indicated.

3.3 Results:

3.3.1 Micromotion Equipment Calibration

The micromotion apparatus was constructed using a combination of custom machined parts, two high precision linear actuators, and an Arduino microcontroller (Figure 3-2a). A 150 device was attached to the apparatus, and programmed to move certain amounts of steps in the in and out (along device axis) and side to side (perpendicular to the device axis). Images were captured at the extreme ends of motion and analyzed to produce a calibration curve in both direction modes (Figure 3-2, Figure 3-4). It was found there was a linear relationship between distance traveled and the number of steps programmed for both in/out and side/side motions. There was minimal backlash in the system, as indicated by the trend line passing near the origin (95% confidence interval for the y-intercept is (-2.6,+2.9 μm). 85 steps in the In/Out direction (approximately 30 μm) at a frequency of 2 Hz was chosen for subsequent *in vitro* glial scar measurements. A test was also conducted to ensure there was minimal variation between the three device holders in the micromotion model (Figure 3-3)

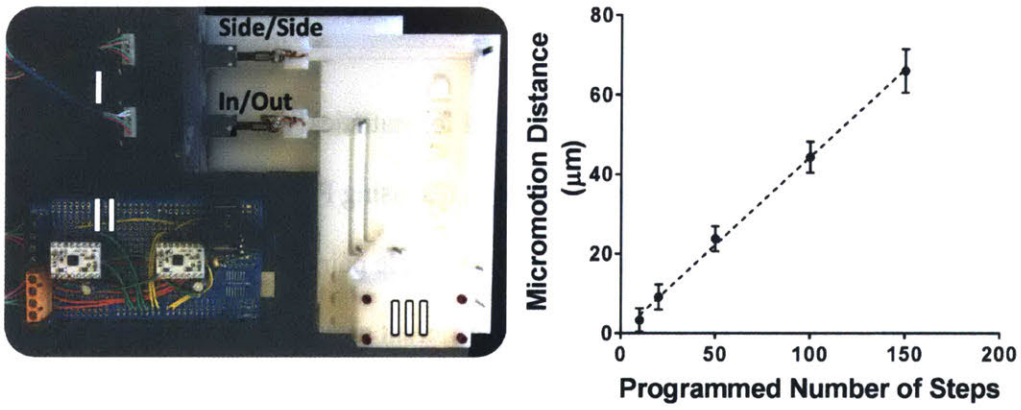

Figure 3-2 Micromotion Simulation Device.
(A) A custom device was built to replicate the effects of micromotion in a 3D glial scar model. The device consists of two high precision linear actuators (II) that are driven by an Arduino microcontroller (III). Mechanical coupling components link the device to the actuators and produce displacements both along the device axis and perpendicular to the device orientation (I) ***(B)*** *The device was calibrated by measuring the distance traveled for various step sizes.*

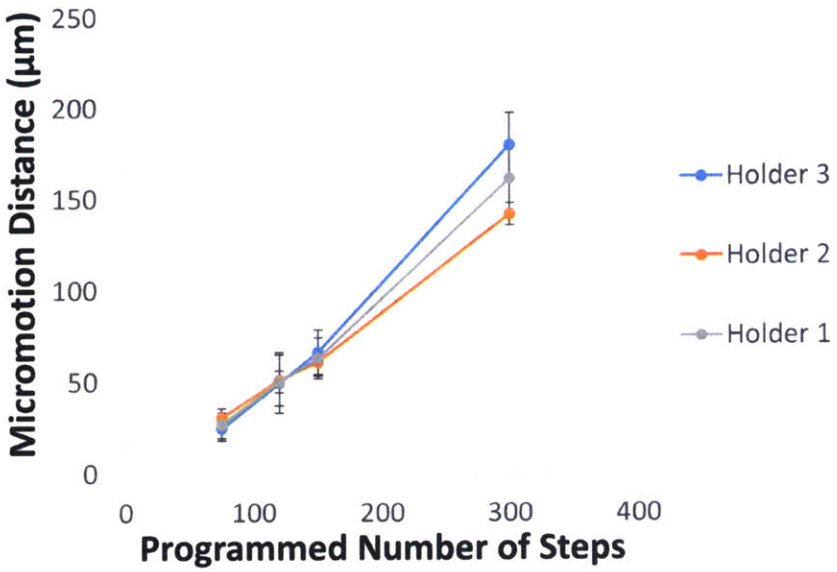

Figure 3-3 Calibration Curve Examining Holder Variation within Model
A test was conducted to ensure that there was minimal variation between the three device holders within the in vitro glial scar model. A programmed number of steps was chosen, and the resulting motion at each of the holders was quantified via image analysis.

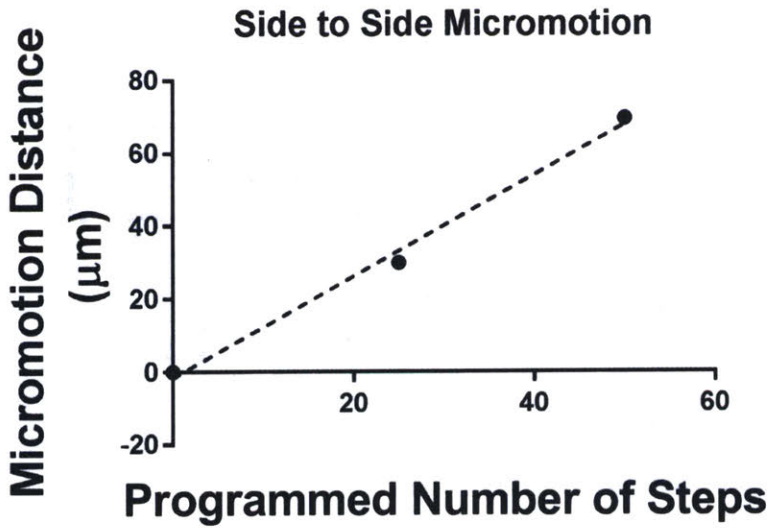

Figure 3-4 Side to Side Calibration Curve
A calibration curve was also obtained for device motion perpendicular to the device axis. Perpendicular micromotions are more representative of rotational accelerations due to head movements.

3.3.2 *In Vitro* Strain Field Measurements:

The strain field was measured following the displacement of a rigid device implanted in a three dimensional collagen gel embedded with fluorescent particles. Images were obtained for three different magnitudes of displacements (8 μm, 80μm, and 130 μm) throughout the course of the displacement. The PIV plugin from ImageJ was used to construct the strain field surrounding the device (Figure 3-5). Line profiles were obtained from these plots (Figure 3-6). Displacements at the surface of the device ranged from 4.23 μm to 84.8 μm. The degree of strain decreased as a function of distance from the device for all three displacement magnitudes investigated. The displacement was 2.8 μm, 28.6 μm, and 51.8 μm at a distance of 400 μm from the implant interface for the 8 μm, 80 μm, and 130 μm displacement respectively.

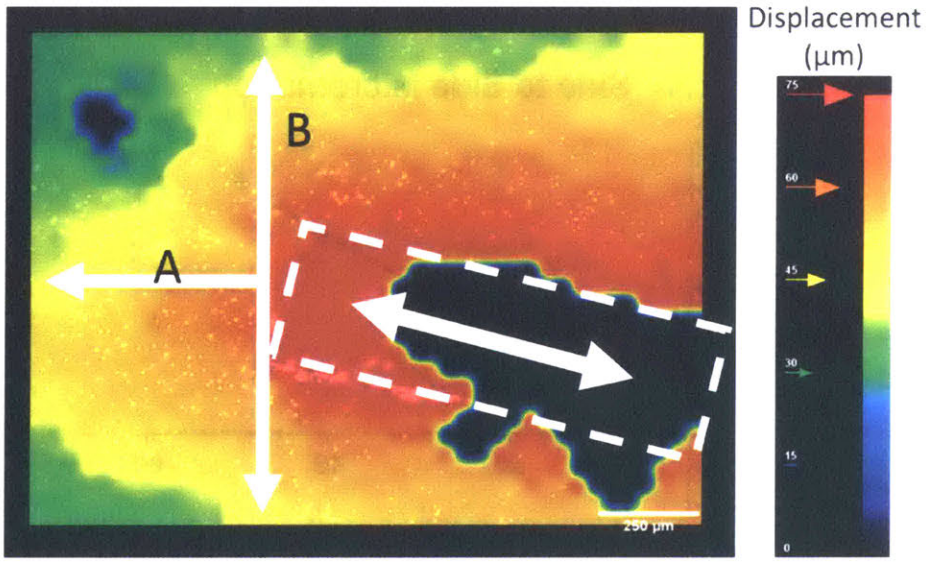

Figure 3-5 Strain Field Map around Device Inserted into a Collagen Gel
Fluorescent polystyrene mircoparticles (6 μm diameter, yellow green) were embedded in a collagen gel (2.0 mg/ml) to measure the strain fields produced around devices during micromotion. ImageJ software was used to calculate the particle displacement following micromotion using the PIV plugin. Shown here is the displacement map for an 80 μm displacement.

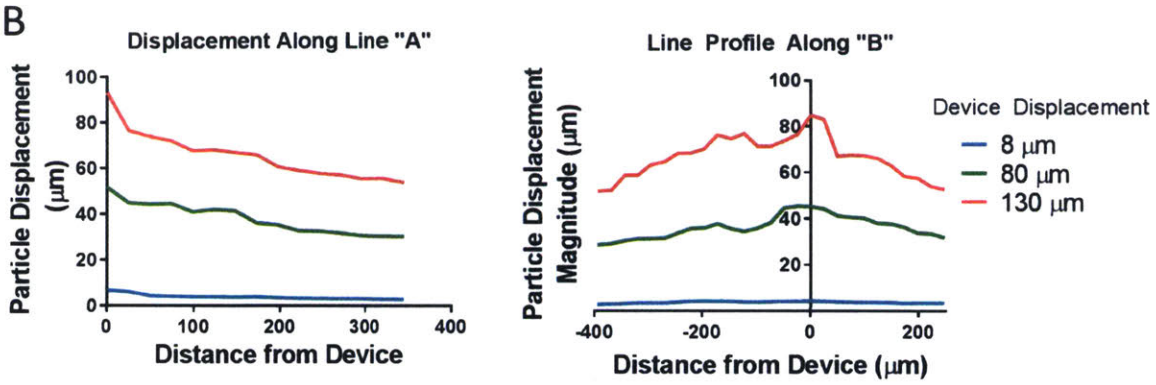

Figure 3-6 Line Profiles from Strain Field Mapping.
The line profiles were calculated for three different displacements in the micromotion model along and perpendicular to the device axis.

3.3.3 Live Dead Cell Staining

Live/dead cell staining was conducted to confirm that neural cell viability could be maintained throughout the course of the experiment. The cells were stained with calcein-AM and ethidium homodimer-1 after one week in culture. Confocal microscopy was used to obtain fluorescent images at various depths into the gel from both the top surface and bottom surface (Figure 3-7). Images were obtained up to 1 mm into the gel from both the top and bottom surface of the gel. Cells could not be effectively imaged beyond this depth due to poor light penetration throughout the gel. The number of live cells (green) and dead cells (red) were counted to produce the total percent viability as a function of depth into the gel (Figure 3-8). The cell viability was found to be around 90% at both surfaces of the gel. The viability at the top surface was slightly higher than the bottom surface (vs. 93.8 ± 2.7% vs 90.7 ± 2.0%). There was minimal variation in the viability as a function of depth in the gel. At a depth of 1 mm from the surface of the gel, the bottom surface was found to have a viability of 89.4 ± 3.4% and the top surface was found to have a viability of 88.7 ± 2.5%. The dead cell control samples had an average viability of 2.0 ± 3.3%. All values discussed in this section represent the mean ± S.D.

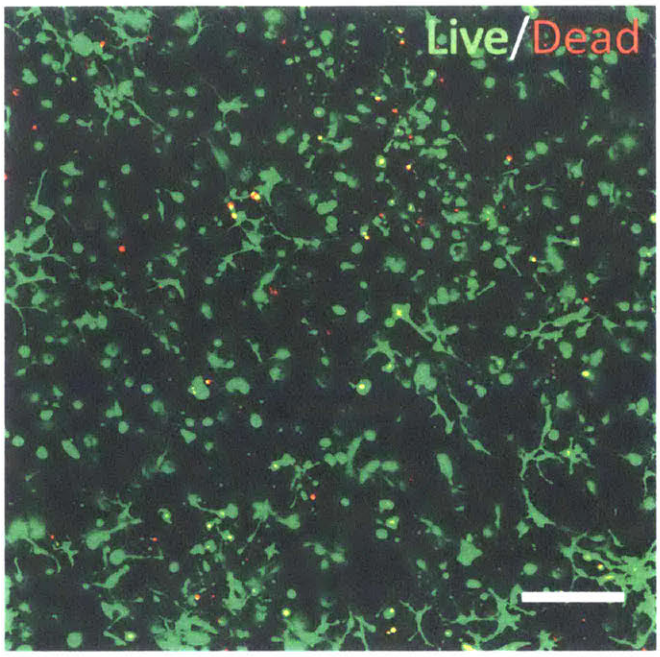

Figure 3-7 Representative Live/Dead Stain after One Week in Culture
The percentage of live cells was determined using Calcein-AM/Ethidium Homodimer-1 cell staining. Representative live/dead immunofluorescent image obtained via confocal microscopy. Image was taken 300 μm into the gel. Green=live. Red=dead. Scale bar 200 μm.

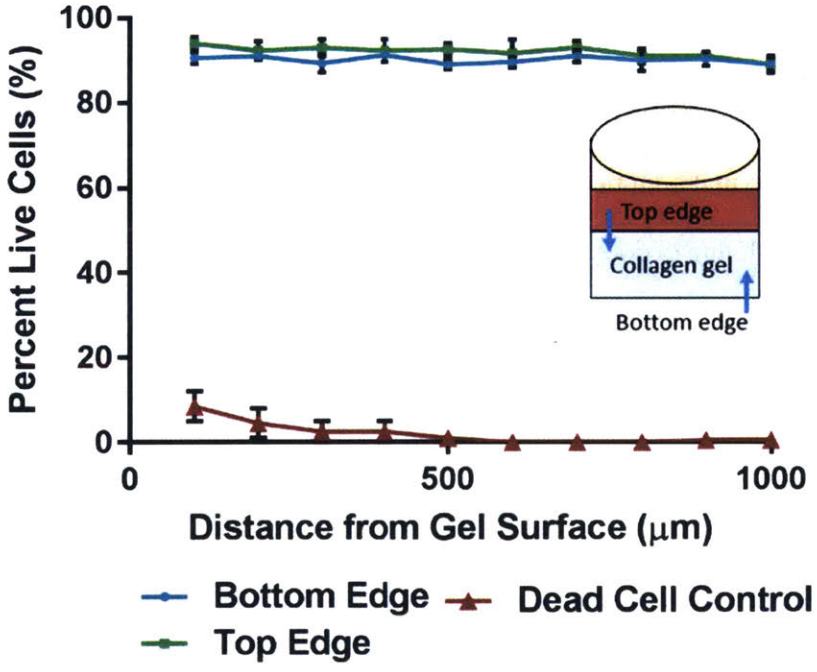

Figure 3-8 Calculated Cell Viability from Live/Dead Stain.
Cell viability as a function of depth into the gel from both the top and bottom edge of the gel (with respect to the media layer). A dead cell control (30 min exposure to methanol) was also included to confirm proper operation of the assay.

3.3.4 Immunohistochemical Analysis

Cells were fixed and stained for the astrocytic marker GFAP to assess changes in the reactivity following 1 week in 3D culture. Antibodies were able to effectively penetrate through the thick collagen gel, and confocal microscopy enabled the region directly surrounding the device to be clearly imaged (Figure 3-9). Extended focus images were obtained from 200 μm z-stacks and analyzed via ImageJ. A threshold was applied to the images to distinguish the cellular boundaries from background (Figure 3-9).

Astrocyte reactivity was compared between groups by assessing the cellular area and perimeter, an approach that has been used in previous *in vitro* glial scar models (*86*). The total perimeter and area of GFAP staining was calculated using the ImageJ particle analysis tool (Figure 3-10). A statistically significant increase in the total GFAP perimeter was observed in the LPS (43936.5 ± 20543 μm), TGF-β (44360.5 ± 19680 μm), and the micromotion around the device (39151.1 ± 15367 μm) compared to the control wells (19066 ± 6997 μm). There was a slight, but not significant, increase in the wells in which a device was inserted but no motion occurred (23009.6 ± 5640.4 μm), as well as in the regions in the micromotion device wells which are a distance away from the device location (21782.72 ± 6092.98 μm).

Similar trends were observed in the total average GFAP area per image measurements. There was a statistically significant increase in the TGF-β wells (186703 ± 134700 μm^2) compared to control wells (65040 ± 26530 μm^2) ($p<.05$). The GFAP area per image was also found to be statistically greater in the regions surrounding the micromotion devices (179200 ± 106720 μm^2) compared to the control wells ($p<.05$). The difference between the LPS positive controls (150838 ± 101495 μm^2) and the control wells was not found to be statistically significant in this experiment ($p=.14$). The no motion well (85600 ± 33400 μm^2), and regions far from the device location in the micromotion wells (70100 ±

24024.8 μm^2), were slightly increased compared to controls, although this difference was not found to be statistically significant. All values discussed in this section represent the mean ± S.D.

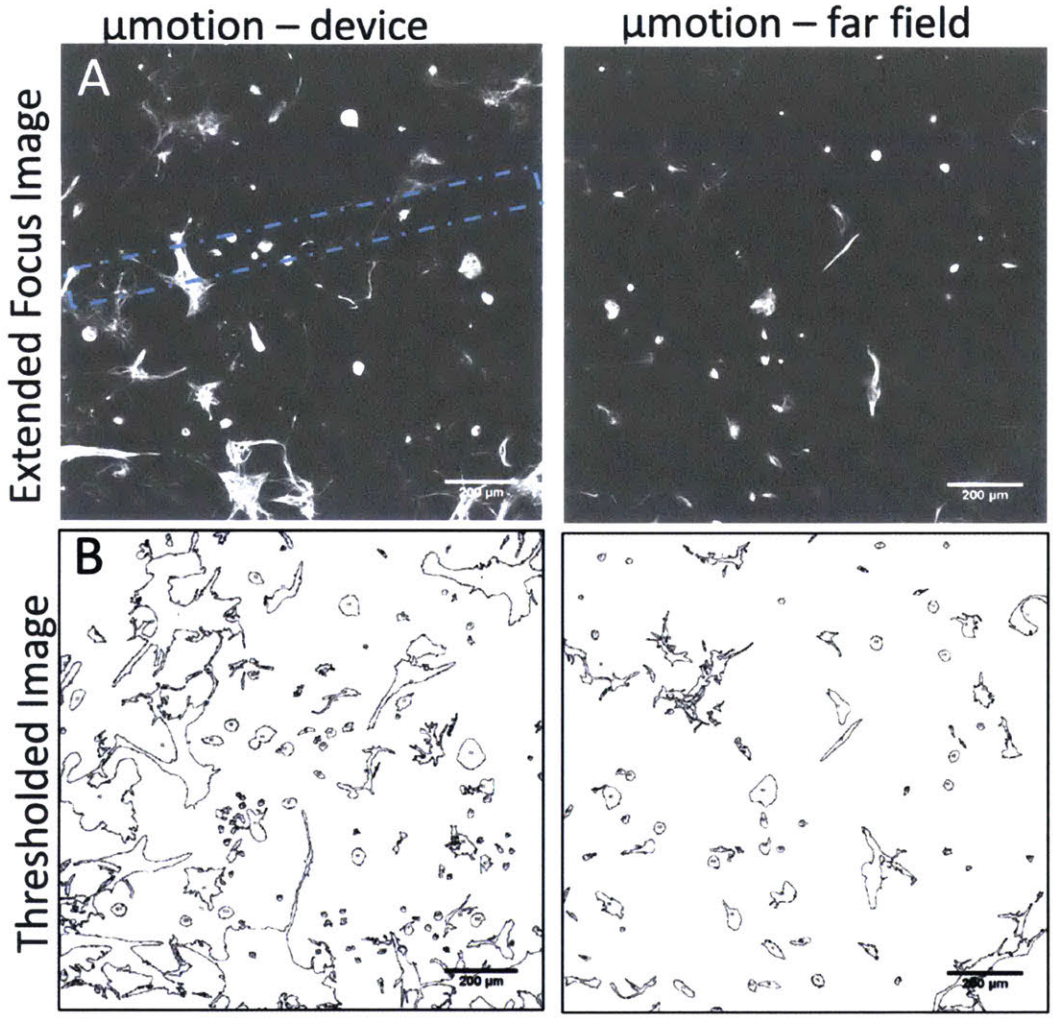

Figure 3-9 Characteristic Confocal Image Obtained Following Glial Scar Experiment

(A) Example extended focus confocal images of the GFAP staining after 1 week of micromotion in a region directly surrounding the implant (left) and a region far away from the device location (right). Scale bar 200 μm. The device location is shown with the dotted line in the left image. ***(B)*** *Cells were identified after thresholding the image with ImageJ. These shapes of these images was analyzed using the particle analysis tool to assess differences in cellular morphology after running the experiment.*

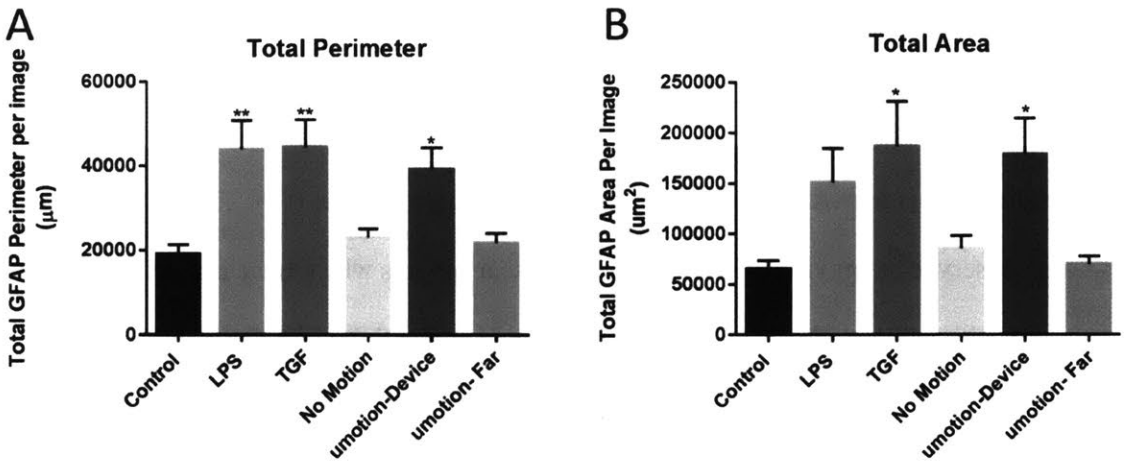

Figure 3-10 Quantified Astrocyte Morphology from Image Analysis.
Astrocytes demonstrate hallmarks of glial scar formation after 1 week in culture for positive control wells and micromotion wells. ***(A)*** *The total GFAP perimeter per image and* ***(B)*** *total GFAP area per image as determined by ImageJ analysis for control, positive control (TGF-B and LPS), and device wells (no motion and micromotion). *p<.05, *p<.01. All sample sizes are N=9, besides for no motion which is N=7.*

3.4 Discussion

There is an ongoing discussion in the field regarding the role that micromotion plays in driving glial scar formation around neural implants (*71*). Evidence to support this hypothesis has been limited to finite element simulation studies (*73, 74*) and *in vivo* studies which rely on histological analysis (*75, 97-100*). These studies highlight the importance mechanical effects at the tissue-implant interface, but are also confounded by the presence of other factors that are present when using *in vivo* models including damage from surgical implantation (*101*), blood-brain barrier breach (*76*), and the presence of blood-derived macrophages (*102*). All of these components are likely to play a role in the scar formation process. The results obtained in this *in vitro* study, however, clearly demonstrate the major contribution that strain fields from micromotion around neural implants have towards driving the glial scar response.

Astrocytes were found to be mechanically responsive in our glial scar model following one week of micromotion. The cells directly within the region of micromotion, as well

as the positive control wells exhibited elevated cellular area and perimeter. The total GFAP area increased 2.75-fold in micromotion samples compared to the control wells, and 2.1-fold compared to wells in which devices were present and no motion had occurred. This hypertrophy is typical of the glial scar response (*69*). This behavior was also observed in previously established glial scar models which have also used TGF-β as a positive control (*86*). The increase in astrocyte reactivity was primarily isolated to regions directly around the device location in which the local strain was greatest, further highlighting the role that micromotion plays in driving the glial response. Areas within the micromotion-strained wells that were far from the device location were only observed to have marginal increases in area and perimeter compared to controls. This slight increase in reactivity far from the motion devices is likely due to an increased production of inflammatory cytokines within the well in response to the mechanical stimuli (*90*). Static wells only showed a slight increase in area and perimeter compared to control wells. This response is likely due to the damage from insertion into the well as well as the presence of a foreign body in the culture. Borosilicate glass is generally regarded as biocompatible (*103*), which potentially explains why the no motion samples did not produce an extensive reaction. The results obtained in this study suggest that strategies which aim to mitigate strain effects from micromotion are essential to improving the long term response to neural implants.

This study was made possible through the creation of a novel *in vitro* model, in which strain fields resulting from micromotion are replicated using high precision linear actuators. All mechanical and electrical components of the model are relatively inexpensive (total cost <$1000) and are open source. A mixed primary neural culture was used, so that the all of the main cell types involved in the glial scar formation processes were present, and therefore critical inflammatory pathways maintained (*69*).

The 3D nature of the model enables strain fields to be created around the neural implant which resemble those that are observed *in vivo*. The magnitude and frequency of the displacements were chosen to resemble the micromotion that were measured in the brain (*72*). Devices were chosen to be displaced in the axial direction as this is most representative of repetitive motion which arises from respiration and vascular pulsations, when devices are implanted perpendicular to the skull (*72*). Future experiments may explore the response to motion perpendicular to the device to resemble rotational acceleration and large scale displacements from concussions (*104, 105*). Future work will also involve expansion of the model so that more devices can be tested simultaneously as well as incorporation of hyaluronic acid components into the culture system to make the cellular environment more representative of the brain extracellular matrix (*106*).

The primary objective in this experiment was explore changes in astrocyte response in the presence of mechanical micromotion, as GFAP is arguably the key factor used in assessing chronic neural implant biocompatibility (*69*). Future work will investigate the interplay between additional cell types present in the culture such as neurons and microglia. Potential future studies may also examine drug interactions (anti-inflammatory drugs that modulate macrophage (*107, 108*) or astrocyte behavior (*109*)), BBB breach (by incorporating IgG or blood borne macrophages in the culture), and incorporation of live cell imaging techniques to further understand the drivers and dynamics of glial scar formation within this model. Potential future studies are discussed in more detail in chapter 5 (section 5.2.3.1).

3.5 Conclusion

Astrocytes grown in a 3D *in vitro* glial scar model were found to be mechanically responsive to local strain fields. These results clearly illustrate the role that local strain fields have in driving glial scar formation. These results highlight the impact that neural probe mechanical factors have on affecting the long term performance of the system. Incorporation of material based strategies (i.e. coating, flexible materials, softening materials) which reduce local strain from micromotion should provide key benefits in improving chronic device function. *In vitro* strain field measurements provide a technique to assess the strain field reductions of these approaches. The use of mechanically matched coatings to reduce scar formation through a strain reduction mechanism will be investigated in the next chapter.

Previously established *in vitro* glial scar models have not incorporated local strain fields surrounding the device, either because they are two-dimensional in nature or produce strain throughout the entire culture. The model presented in this study will enable mechanical design factors (such as coatings, mechanically adaptive composites, serpentine connectors etc.) to be tested prior to *in vivo* work. The tunable nature (adjustable direction, magnitude, and frequency) of our model will enable researches to optimize neural probe design over a wide range of motion conditions.

4 MECHANICALLY MATCHED HYDROGEL TO REDUCE SCARRING AROUND NEURAL IMPLANTS

4.1 Introduction and Background

Neural implants developed in recent years have shown great promise to improve and restore quality of life for millions of patients around the world. These implants have been demonstrated as potential solutions to treat neurological disorders (*110-113*), restore limb function (*114, 115*), and unravel the complexities of neural circuits (*116, 117*).

These devices can interface with neurons both chemically and electrically and need to operate chronically, especially considering the invasive nature of the implantation process (*118*). The implant must operate safely and effectively in the presence of any biological response to the implant for months to years. Many studies have characterized the brain's immune response to the presence of the neural implant known as astrogliosis, which results in the formation of glial scar directly surrounding the implant (*69*). The immune response can be divided into two phases – the acute phase and the chronic phase.

The acute response is primarily dominated by microglia and occurs over the first few weeks following implantation. The microglia release pro-inflammatory cytokines and reactive oxygen intermediates (ROIs) in response to the implantation injury. These species promote inflammation, negatively affect neuron viability in the vicinity of the implant (*69*), and may impact device integrity (*119*).

The chronic response is observed at longer implantation times (>4 weeks). The most notable feature of the chronic immune response is the formation and densification of

glial scar around the implant. Reactive astrocytes, characterized by up-regulation of glial fibrillary acidic protein (GFAP) and the increased production of chondroitin sulfate proteoglycans, surround and isolate the injury site from the rest of the neural tissue (*69, 120, 121*). The glial sheath which is typically a few hundred microns thick becomes dense around 4-6 weeks and remains stable for the duration of the implantation (*122, 123*). This process is analogous to the fibrous encapsulation that is observed around implants in other parts of the body (*124-126*).

Glial scar forms with the intent to protect the rest of the CNS from the foreign body within the tissue as well as reactive species released following injury to the brain (*69, 127, 128*). Despite these acute benefits, glial scar formation is a key contributor to neural implant failure. Nearly half of all recording implants fail within 6 months of implantation despite initially operating correctly due to glial scar formation (*129, 130*). Glial scar displaces neurons near the implant. Neurons typically need to be within 100 μm of an electrode to be recorded (*131*). The presence of glial scar decreases the probability that neural signals can be detected by recording electrodes (*54*). Glial scar is also known to increase the impedance of the tissue. This effect reduces the volume of tissue activated by electrical stimulation by up to 50% for a typical set of Deep Brain Stimulation (DBS) parameters (*132*). A higher current is then required to produce a therapeutic effect on a given neural circuit. These higher charge densities can lead to local tissue damage through electrochemical reactions or physiological changes in response to neural excitation (*44, 131, 133*). Glial scar is also known to negatively affect chemical diffusion properties in the tissue surrounding the implant which could negatively affect drug distribution surrounding neural implants. Sykova et al. used ion selective electrode measurements to determine that astrogliosis locally increases tortuosity, ECS volume fraction, and decreases cellular uptake (*120, 134, 135*).

Conventional neural implant materials have moduli that are many orders of magnitude higher than that of brain tissue (Table 4-1). Brain tissue is constantly undergoing micromotion (up to 40 μm in magnitude in rats) due to respiration, vascular pulses, and rotational accelerations (*72, 104*). This persistent relative motion between the implant and tissue is thought to play a role in directing the chronic response through constant aggravation of local inflammatory cells and damage to local vasculature. The data presented in Chapter 3 demonstrates that astrocytes are mechanically responsive to the strain produced from micromotion. Micromotion around neural implants was simulated using high precision linear actuators within a 3D neural culture. Astrocytes directly around the implant were found to undergo hypertrophy (increased area and perimeter) compared to control wells after one week in culture.

The local strain from micromotion results in local mechanical damage which drives scar formation. Finite element analysis (FEA) simulations have been conducted to model the effect that mechanical mismatch has on the surrounding tissue (*73, 74*). These simulations estimate the amount of strain that the brain tissue experiences as a result of brain micromotion in the presence of neural implants with various mechanical properties. A probe composed of a hypothetical soft material with modulus of 6MPa results in a strain two orders of magnitude less than that of a silicon probe (E=200GPa) (*74*). Future neural implant designs could incorporate materials with lower mechanical stiffness and/or coatings that promote adhesion with neural tissue to reduce the extent of glial scar formation.

There have been many studies conducted with the goal of reducing the scar response to implanted electrodes with results of varying success (*123, 136-140*). These studies provide insight into the mechanisms of scar formation, and provide suggestions regarding device properties that are important to consider when designing chronic

neural implants. There is, however, a clear need for additional guidance on how key implant design parameters affect the glial scar response around the implant, specifically when considering strategies to modulate the mechanical effects from micromotion.

This study investigates the how device dimensions and mechanical properties modulate the immune response in the brain, specifically in the context of using hydrogel coatings to mitigate mechanical damage from micromotion. Thick (25-100 μm) polyethylene glycol dimethacrylate (PEG-DMA) hydrogel coatings, with mechanical properties close to that of brain tissue, were formed on neural implants. The mechanical properties of these coatings was characterized. The ability to reduce local strain fields was investigated *in vitro*, and the acute and chronic *in vivo* response to these coatings was investigated in a rodent cranial implantation model. Previous studies have only explored polymer coatings at a certain dimension, therefore comparing implants with both differing diameters and mechanical properties. To that end, this study incorporates size based controls to decouple the size and mechanical effects of 10-100 μm scale coatings. Together these experiments seek to elucidate a clear framework for ideal neural implantation parameters for optimal device performance.

Material	Elastic Modulus (GPa)
Borosilicate Glass	69
Gold	80
Silicon	200
Titanium	107
Polyimide	2
Brain	.000005

Table 4-1 Moduli of Common Neural Implant Materials
Typical neural implant materials are many orders of magnitude stiffer than brain tissue (141) (142) (74).

4.2 Materials and Methods

4.2.1 Materials

Polyethylene glycol (MW 2000, 4000, 8000), methacrylic anhydride, triethyl amine, 3-(trichlorosilyl) propyl methacrylate, 2-Hydroxy-4′-(2-hydroxyethoxy)-2-methylpropiophenone, agarose, and all solvents used in this study were purchased from Sigma Aldrich (St. Louis, MO, USA) and were ACS grade or better. All chemicals and antibodies were used as-received unless noted otherwise. 150 μm and 400 μm OD glass capillaries were purchased from Vitrocom, Inc (Mountain Lakes, NJ, USA). 200 μm capillaries were purchased from Hampton Research (Aliso Viejo, CA, USA). All glass capillaries were sterilized via autoclave upon receiving from manufacturer prior to any handling.

4.2.2 Synthesis of PEG-Dimethacrylate

Polyethylene glycol dimethacrylate (PEG-DMA) was synthesized according to a procedure adapted from Lin-Gibson et al. (*143*). Briefly, 10 g of PEG (MW 700-8000) was dissolved in approximately 30 ml of anhydrous dichloromethane. The solution was reacted with 2.2 molar equivalents of methacrylic anhydride and triethyl amine (0.4 ml) over activated molecular sieves (3 g). The reaction was allowed to proceed to completion under nitrogen atmosphere (4 days at room temperature). The solution was filtered via vacuum filtration, and approximately 20 ml of dichloromethane was removed via rotary evaporation. The PEG-DMA was precipitated in ice cold diethyl ether. The product was dried under vacuum at room temperature overnight to remove residual solvent prior to subsequent use.

4.2.3 Formation of PEG Hydrogel on Glass Capillaries

PEG-DMA hydrogel coatings were formed on the surface of the glass capillaries (Figure 4-1).

Glass capillaries were etched in piranha solution (3:1 ratio of concentrated sulfuric acid to 30% hydrogen peroxide) for five minutes. The capillaries were then washed three times in DI water, and dried under nitrogen atmosphere.

The cleaned, glass capillaries were treated with 1 mM 3-(trichlorosilyl) propyl methacrylate (TPM) in a 4:1 ratio of heptane-carbon tetrachloride under N2 atmosphere for 10 minutes. The capillaries were then washed in hexane, acetone, and water. The TPM treatment covalently functionalized the glass surface with methacrylate functional handles to improve hydrogel adhesion. The TPM-functionalized glass capillaries were stored under inert gas prior to hydrogel formation.

Hydrogel precursor solution was prepared by combining PEG-DMA in water (5-20% weight/volume) with the photo initiator 2-Hydroxy-4′-(2-hydroxyethoxy)-2-methylpropiophenone (0.5% w/v). Treated capillaries were placed in a cylindrical glass mold (200-400 μm I.D.). The mold was filled with hydrogel precursor solution. The solution was exposed to a UV light source (Cure Spot 50, Dymax Corp, Torington, CT, USA) for 60s to crosslink the polymer network and form the hydrogels on the glass device. The coated capillaries were removed from the mold, and stored in PBS until experimental use. The main defect observed throughout the gel formation process were shearing of the coating during removal of those mold, as well as the glass device not being centered in the mold. Both of these defects were easily identified through visual inspection and were not used in subsequent experiments.

Devices were cut to approximately 5mm in length, attached to micromachined Delrin caps for easy handling, and were sterilized by soaking in 70% ethanol for 24 hours, followed by UV exposure (λ=254 nm) for one hour prior to implantation. Devices were washed three times in sterile tissue culture grade water, and hydrogel coatings were dehydrated by exposure to air prior to *in vivo* implantation studies.

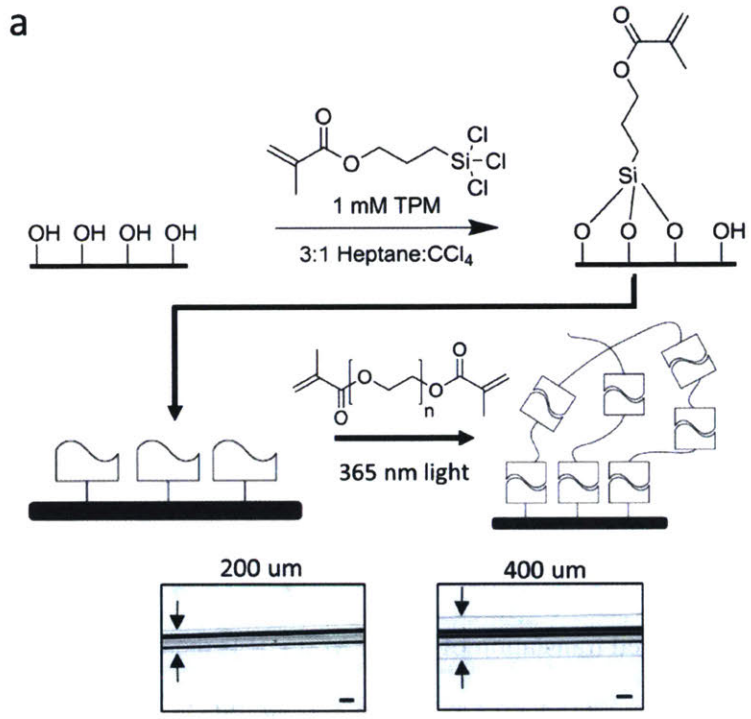

Figure 4-1 Reaction Scheme to Form Hydrogel Coatings on Borosilicate Glass Capillaries
Soft PEG hydrogel coatings were formed on borosilicate glass capillaries through a multistep process. The surface of the glass is piranha etched followed by treatment with 1 mM TPM. An aqueous PEG dimethacrylate solution is then filled into a cylindrical mold containing the treated capillaries. Exposure to UV light crosslinks the polymer network and forms the hydrogel on the surface of the device. The thickness of the hydrogels can be readily controlled by adjusting mold geometry. Representative BF images of the hydrogel images are shown below the reaction scheme (scale bar =150 μm)

4.2.4 Mechanical Characterization of PEG Hydrogels

The Young's modulus of the PEG-DMA hydrogels was measured via analysis of atomic force microscopy (AFM) force curves. Planar hydrogels (approximately 100 μm thick) were formed on TPM treated borosilicate glass slides for use in the AFM

measurements. Hydrogels were loaded into the AFM (Veeco, Nanoscope IV with picoforce scanner head, Oyster Bay, NY), and the tip (k=14N/m with functionalized 45 μm polystyrene bead tip, Novascan) was brought into contact with the sample surface. The tip deflection was measured as a function of indentation depth over the course of a 1.5 μm z-displacement. The elastic modulus was then determined via Hertzian analysis of the force displacement curve (*144*). Briefly, force-displacement curves were obtained by calculating the force applied to tip by the equation:

$$F = k_c(d - d_0)$$

where k_c is the spring constant of the cantilever, d is the measured tip deflection, and d_0 is the tip deflection at the point when the tip contacts the material surface. A characteristic force-displacement curve is shown below (Figure 4-2). For a hemispherical tip geometry, the modulus may be extracted from the following equation:

$$F = \frac{4\,E\,R^{\frac{1}{2}}}{3(1-\upsilon^2)}[(z - z_0) - (d - d_0)]^{3/2}$$

where z is the measured translation of the AFM tip, R is the radius of the tip, ν is the Poisson's ration (assumed to be 0.5 for an incompressible hydrogel sample), and E is the elastic modulus.

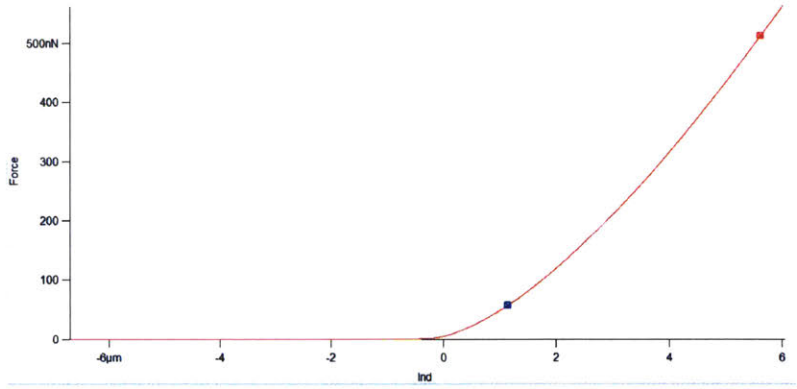

Figure 4-2 Characteristic Force Displacement Curve for Elastic Modulus Measurement

The elastic modulus of the hydrogels was determined via Hertzian analysis of AFM force curves. The y-axis is the force required to produce the measured tip displacement for a given amount of tip displacement (x-axis).

4.2.5 *In Vitro* Strain Field Measurements

A 0.6% agarose brain phantom with embedded polystyrene beads (0.005% w/v, 6 µm, Polysciences Inc, Warrington, PA) was formed around uncoated and hydrogel coated devices, which were mechanically linked to a linear actuator. The devices were displaced 30 µm at a frequency of 2 Hz in the perpendicular and axial directions to simulate micromotion due to rotational accelerations and respiration/vascular pulsations respectively (27, 28). A series of bright field images were obtained before and after displacement. The images were analyzed via the Particle Image Velocimetry (PIV) plugin for ImageJ to construct the displacement fields around the device. Strain fields were measured for uncoated devices (GC150), 200 µm hydrogel coated devices (P10-200), and 400 µm hydrogel coated devices (P10-400) in both directions of motion.

4.2.6 Device Implantation in Rodent Brain

All animal studies were conducted in accordance with the guidelines of the Committee on Animal Care at Massachusetts Institute of Technology. No experiments were conducted until protocol approval was received. All instruments used in the surgical procedures were autoclaved and sterilized between animals using a glass bead heat

sterilizer. Two devices were implanted (one per hemisphere) for each animal used in this study.

Adult female Fisher F344 (150-175 g, Charles River Laboratory, Wilmington, MA) were anesthetized via isoflurane (2-3% mixed with oxygen). The animals head was shaved and disinfected with alternating scrubs of betadine and isopropanol (3x each). The animal was transferred to a stereotactic frame. An incision was made along the midline to expose the skull. A high speed drill was used to perform the two craniotomies at coordinates of 2mm posterior, 2mm lateral to Bregma. The dura mater was removed using a bent 31 gauge needle. Bleeding was stopped before device implantation and the brain surface was irrigated with saline. The devices were slowly lowered into the brain until the plastic handling cap was in contact with the skull. The devices were fixed to the skull using Metabond and Cement-It dental cement (Pentron, Orange, CA). The skin was pulled over the dried cement and sealed with 5-0 monofilament nylon sutures. Buprenorphine-SR (1.0 mg/kg) was provided to the animal as an analgesic for 72 hours post implantation. No meloxicam was administered to the animals in this study to avoid the NSAID from affecting the inflammatory processes.

The naming convention used in this study for the hydrogel coated samples is P(Concentration)-Swollen Thickness. For example, P10-200 refers to a device coated with a 10% PEG hydrogel, with a total thickness of device plus hydrogel was 200 μm. All hydrogel coatings were formed on 150 micron diameter glass capillaries. Samples that start with GC refer to unmodified glass capillaries followed by the diameter in microns (i.e. GC150 = 150 micron, uncoated glass capillary).

Experimental groups for the animal studies consisted of glass capillaries with diameters ranging between 150 μm, 200 μm, and 400 μm (GC150, GC200, GC400) and PEG-DMA 10% hydrogel coated capillaries with a total thickness of 200 μm and 400 μm

(P10-200, P10-400). An initial pilot study of non-coated and P10-200 samples was used to estimate the sample sizes required for statistical power (n=6). $n \geq 6$ for each experimental group and time point unless otherwise noted. The sample size for each cohort is indicated in the figure legend.

4.2.7 Animal Euthanasia and Tissue Harvesting

Animals were euthanatized at set time points following device implantation (1 week, 4 weeks, 8 weeks) via CO_2 asphyxiation. Animals were perfused with approximately 50 ml of PBS followed by 100 ml of 4% paraformaldehyde in PBS. The brains were allowed to post fix for 48 hours after perfusion prior to removing the devices from the tissue. The brains were placed in sucrose sinking solutions of increasing concentration (10%, 20%, 30% sucrose in PBS) until sinking was observed. Brains were frozen in optimal cutting temperature compound by immersion in liquid nitrogen chilled 2-methyl butane. 20 μm thick sections, cut perpendicular to the device axis, were obtained with a cryostat (Leica Microsystems, Buffalo Grove, IL, USA). Tissue sections were stored at -80° C prior to immunostaining.

4.2.8 Immunohistochemistry

Tissue sections were stained for glial scar/ inflammation markers including glial fibrillary acidic protein (GFAP, 1:100 mouse anti-GFAPx488 Alexaflour, EMD Millipore, Billerica, MA, USA) to assess the extent of scarring, ED1/CD68 (1:300, clone ED1, EMD Millipore, Billerica, MA, USA) to assess activated macrophages, IgG (1:250, Donkey Anti-Rat IgGx647 Alexafluor, Abcam, Cambridge, MA, USA) to assess blood-brain barrier (BBB) permeability, and local neural nuclei NeuN (1:300, rabbit anti-NeuN, EMD Millipore, Billerica, MA, USA). Frozen sections were equilibrated to room temperature, and rehydrated for 10 minutes in PBS-0.5% tween.

Sections were incubated in PBS with 5% donkey serum for 1 hour at room temperature to prevent non-specific staining. Primary antibodies were diluted in antibody incubation buffer (PBS containing 1% bovine serum albumin, 1% normal donkey serum, 0.3% triton x-100, and 0.01% sodium azide). Sections were incubated in the primary antibody overnight at 4° C. Sections were washed three times, and incubated with secondary antibody diluted in incubation buffer (1:300 Donkey Anti-Rabbit x Dylight 650, Abcam, 1:300 Donkey-AntiMousex488 Alexafluor, Millipore) for 1 hour at room temperature. Slides were washed three times and counterstained with Hoechst 33258 (2 μg/ml, Sigma Aldrich, St. Louis, MO, USA) for 15 minutes. Slides were rinsed in PBS and coverslips were mounted with Prolong Gold (Invitrogen, Carlsbad, CA, USA). Slides were stored at 4 °C prior to imaging.

4.2.9 Imaging and Data Analysis

Fluorescent stained sections were imaged on the EVOS Fl automated microscope (Thermo Fisher Scientific, Waltham, MA, USA). The device location was identified and stitched images (approximately 5mm x 5mm) were obtained in the area surrounding the implant site. Exposure settings were chosen to avoid saturation and were maintained for each individual marker. Images were not altered in any way prior to image analysis.

The staining intensity as a function of distance from the tissue-implant interface was quantified using the MINUTE program, provided by the Capadona lab at Case Western Reserve University (CWRU, Cleveland, OH, USA) (*101*). Briefly, the implant interface was defined by the user, and the fluorescent intensity was quantified in 2 μm rings extending from the implant. The total fluorescent intensity was normalized to a region far from the implant site (>1mm) to account for differences in section thickness/staining efficiency. Four sections were imaged for each animal to produce an average intensity

profile which was used for subsequent statistical analysis. The area under the curve was segmented into 50 μm binned intervals around the device location.

No randomization or blinding was conducted in this study. The use of the automated MINUTE analysis program helped ensure user bias was minimized throughout the analysis process. No data exclusion criteria was applied. The only animals excluded from analysis were animals in which severe surgical trauma had occurred (e.g. excessive blood observed under implant, (n=3), or major tissue damage occurred during device retrieval (n=2).

4.2.10 Statistical Analysis

Observed experimental differences were assessed for statistical significance across all experimental cohorts through a two-way ANOVA test using Prism 6 (In Stat Graphpad, La Jolla, CA, USA). Post hoc analysis (Tukey's multiple pairwise comparisons test) was performed to compare marker expression between groups at different distances from the device-tissue interface. Statistical significance was considered $p < 0.05$. All data presented represents mean ± standard error of the mean unless otherwise indicated.

4.3 Results

4.3.1 Hydrogel Formation and Characterization

PEG-DMA hydrogel coatings were formed on 150 μm borosilicate capillaries via a UV polymerization process (Figure 4-1). The thickness of the coating was controlled by changing the mold geometry. Coatings were produced with a total final diameter of 200 μm and 400 μm, and had minimal variation in thickness along the length of the device (Figure 4-1). It was determined that coatings could be dehydrated prior to implantation to maintain coating integrity. The kinetics of coating rehydration was measured in water

and an agarose brain tissue phantom (Figure 4-3). The coating returned to its original dimensions in approximately two minutes, with no significant difference in thickness or morphology. No major differences in the kinetics of swelling were observed between water and tissue phantom.

The elastic modulus of the hydrogels was measured via Hertzian analysis of AFM force curves. The hydrogel formulations tested in this study spanned three different polymer concentrations before crosslinking (5%, 10%, and 20% w/v%) and three different PEG-DMA molecular weights (MW = 2000, 4000, and 8000). These hydrogels had elastic moduli ranging from 1.6 kPa to 171.5 kPa.

Trends observed in the modulus data demonstrate that the elastic modulus may be easily controlled based on reaction conditions. Increasing the polymer concentration before crosslinking increases the resulting modulus of the hydrogel (Figure 4-4). A major increase (approximately 10x) in the modulus was observed between 10% and 20% polymer concentration. A slight decrease in elastic modulus was observed when producing hydrogels with longer length PEG-DMA molecules (Figure 4-4). For subsequent *in vivo* experiments, 10%, MW8000 hydrogels were used which were found to have an elastic modulus of 11.64 +/- 2.0 kPa.

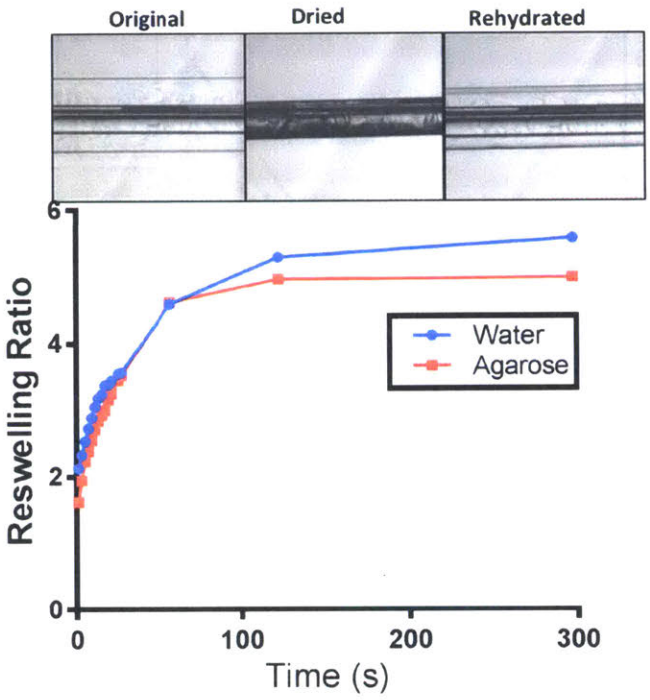

Figure 4-3 Hydrogel Coating Swelling Kinetics
The hydrogel coatings are dehydrated prior to implantation to maintain coating integrity. The kinetics of rehydration was monitored in water and a 0.6% agarose brain tissue phantom.

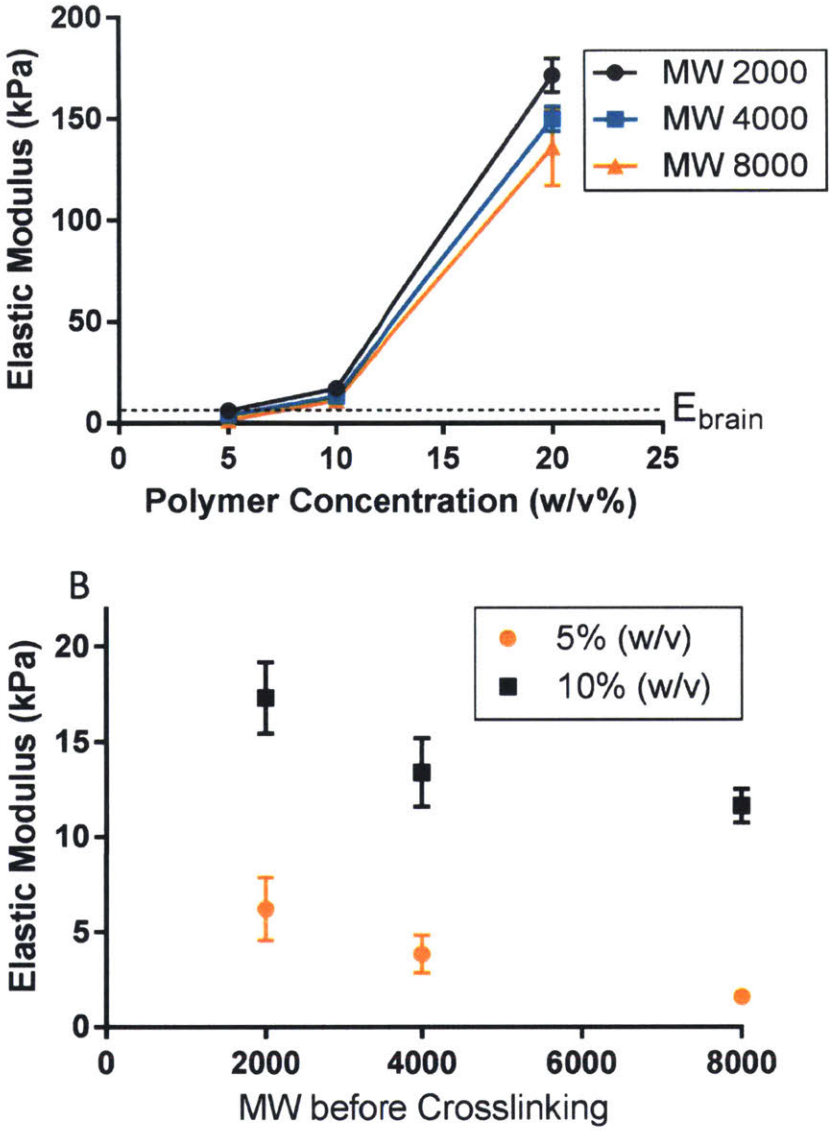

Figure 4-4 Hydrogel Mechanical Characterization
The elastic modulus of the hydrogel was measured via Hertzian analysis of AFM force curves at several polymer concentrations and PEG-DMA chain lengths. The elastic modulus of the coatings is controlled by adjusting the polymer concentration before crosslinking and the PEG-DMA molecular weight.

4.3.2 *In Vitro* Strain Field Reduction

The ability of hydrogel coated devices to reduce the local strain fields which result from micromotion was measured using a custom built *in vitro* micromotion simulation set up (29). Devices coated with PEG-hydrogels of two thicknesses (200 μm and 400 μm) were coupled to a high precision linear actuator, embedded in a 0.6% agarose brain

tissue phantom, and 30 μm displacements were applied along and perpendicular to the device axis. Series of images were taken throughout the motion process. Images at the two extremes of motion were analyzed via the ImageJ PIV plugin to construct the displacement fields around the device (Figure 4-5,Figure 4-7). A clear reduction in the local strain field around hydrogel coated devices was observed for both hydrogel thicknesses both in terms of size and magnitude for both directions of motion. The average displacement at the surface of the device for the non-coated control was 10.9 ± 2.3 μm, 6.7 ± 1.4 μm for the P10-200 group, and 3.2 ± 0.64 μm for the P10-400 group for the side to side motion direction (Figure 4-6). The thicker hydrogel was observed to have reduced strain for all distances from the device investigated in this study.

A slightly different behavior was observed when the devices were displaced in the axial direction. The P10-200 hydrogel samples produced less strain than the P10-400 and non-coated samples (Figure 4-8). The average displacement at the surface for the non-coated control was 24.0 ± 1.2 μm, and was 17.25 ±3.5 μm for the 400 μm hydrogel sample, and was 8.4 ± 4.8 μm for the 200 μm hydrogel sample (mean ± S.D.). There was a significant reduction ($p<.05$) between NC and P10-400 up to 190 μm away from the device-tissue interface. The difference in average displacement between the P10-200 hydrogel sample and the non-coated sample was found to be statistically significant ($p<.01$) for all distances investigated in this study.

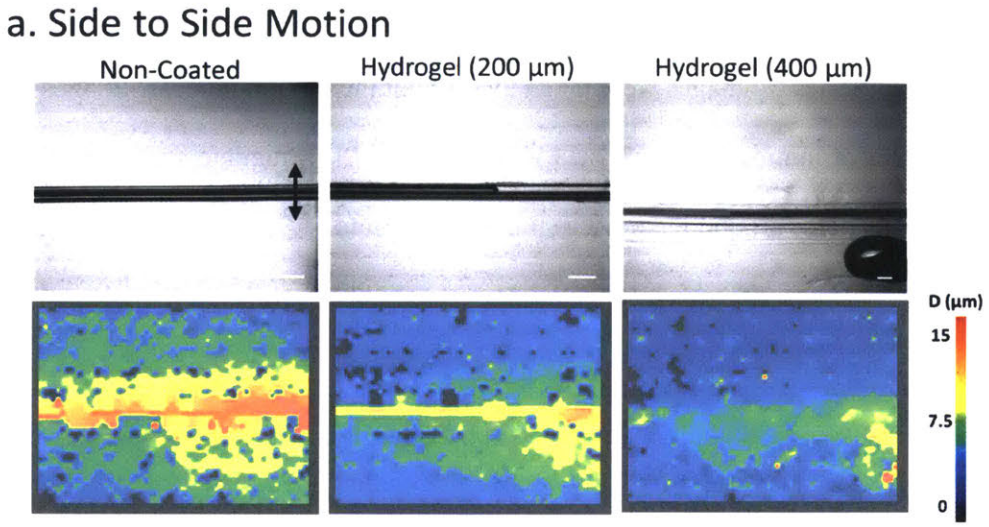

Figure 4-5 *In Vitro* Strain Field Magnitude Maps for Side to Side Micromotion
Hydrogel coated devices reduce local strain fields which result from micromotion compared to non-coated controls. Particle image velocimetry was used to quantify the displacement surrounding the device. (A) BF images and strain field plot overlays following a 30 micron perpendicular displacement which was applied to devices embedded within an agarose tissue phantom to mimic micromotion which arises from rotational accelerations (scale bar 150 µm).

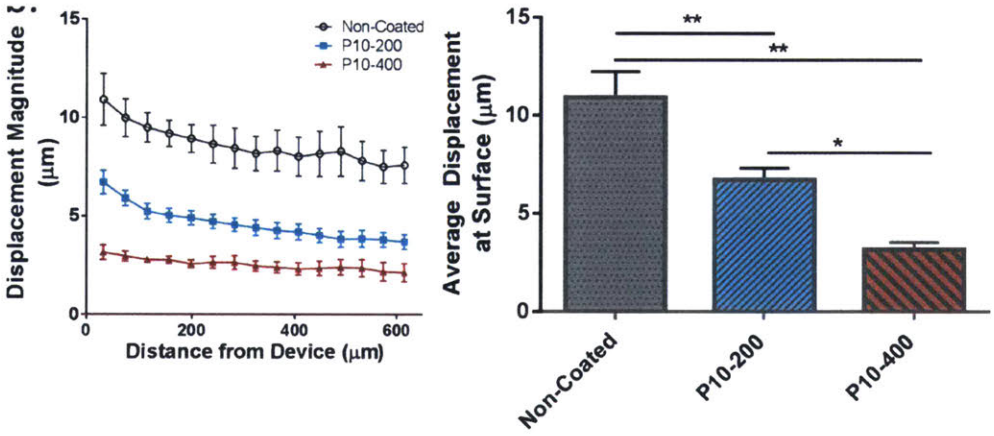

Figure 4-6 Hydrogel Strain Field Line Profiles for Side to Side Micromotion
*Average line profiles of the displacement magnitude as a function of distance from the device and (C) the average displacement at the surface were calculated. Hydrogel coated samples significantly reduced strain fields around the device. *p<.05, **p<.01, ***p<.001.*

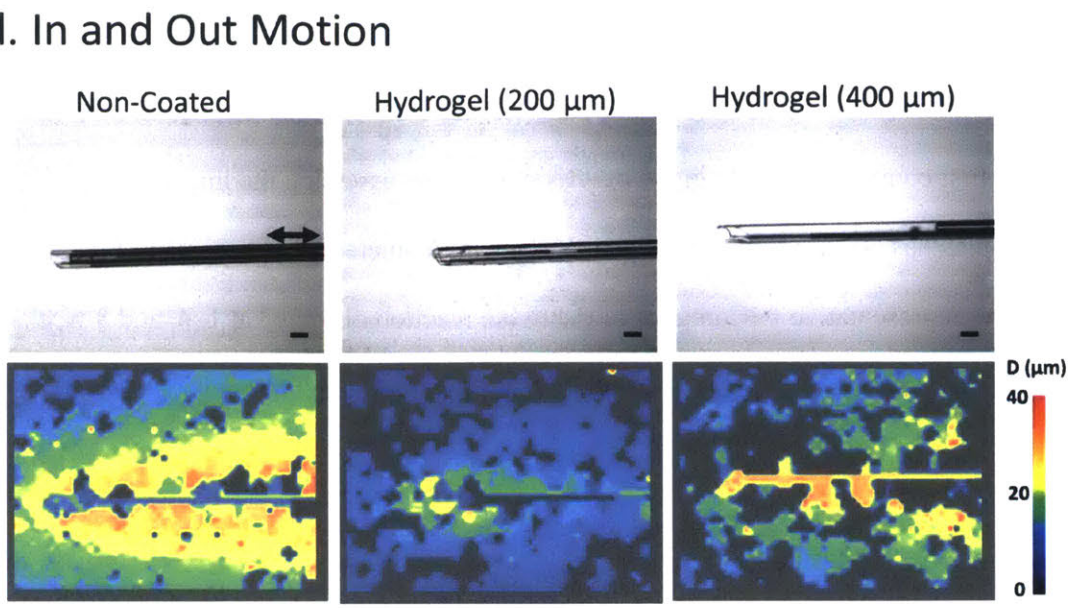

Figure 4-7 *In Vitro* Strain Field Magnitude Maps for Axial Micromotion
Hydrogel coated devices reduce local strain fields which result from micromotion compared to non-coated controls. Particle image velocimetry was used to quantify the displacement surrounding the device. (A) BF images and strain field plot overlays following a 30 micron displacement which was applied to devices embedded within an agarose tissue phantom to mimic micromotion (scale bar 150 µm).

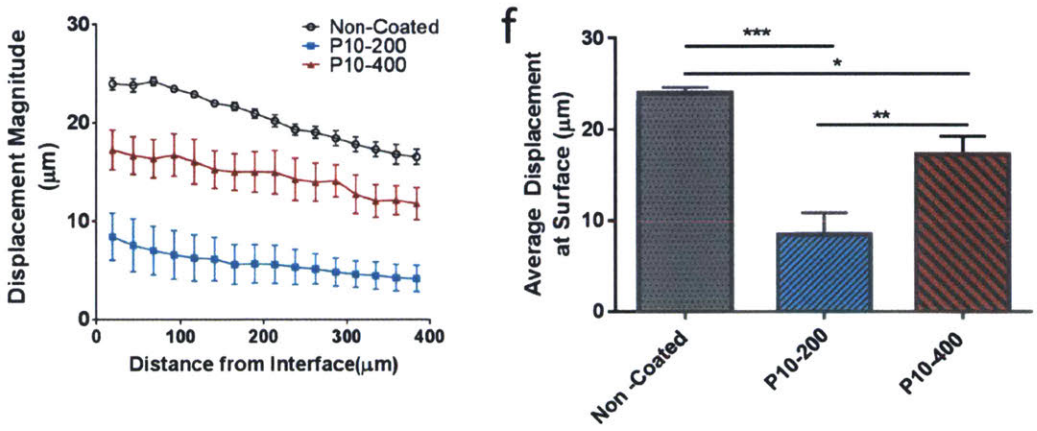

Figure 4-8 Hydrogel Strain Field Line Profiles for Axial Micromotion
*Average line profiles of the displacement magnitude as a function of distance from the device and (C) the average displacement at the surface were calculated. Hydrogel coated samples significantly reduced strain fields around the device. *p<.05, **p<.01, ***p<.001. Samples sizes: Non-coated: N=4, 400 µm hydrogel: N=3, 200 µm hydrogel: N=4*

4.3.3 *In Vivo* Animal Study Results

4.3.3.1 Size Control Hydrogel Study

The first comparison made in the *in vivo* studies was assessing the impact that implant modulus has on scar formation when the implant diameter is held constant. Figure 3 shows representative IHC images of the tissue reaction observed at 1, 4, and 8 weeks post implantation for glass capillaries (GC200, GC400) and hydrogel coated samples (P10-200, P10-400) (Figure 4-9A, Figure 4-9B). The MINUTE program (provided by the Capadona Lab at CWRU) was used to quantify amount of GFAP staining as a function of distance from the device-tissue interface (Figure 4-10). Both hydrogel coated samples (P10-200 and P10-400) samples showed reduced GFAP reactivity at 1, 4, and 8 weeks post implantation when compared to the glass capillary implants (GC200 and GC400). P10-200 was significantly reduced compared to GC200 up to 100 μm from the implant at 1, 4, 8 weeks post implantation. The scarring in the P10-200 samples was reduced by 50% at four weeks post implantation, and 40% at eight weeks compared to the GC200 samples. P10-400 was had significantly reduced scarred compared to GC400 up to 200 microns away from the implant at one week post implantation. At four weeks post implantation, GFAP staining for the P10-400 samples was significantly reduced (approximately 60%) in the 100 microns surrounding the implant interface. At eight weeks post implantation, P10-400 samples were found to have a 60% decrease in GFAP staining up to 200 microns away from the implant.

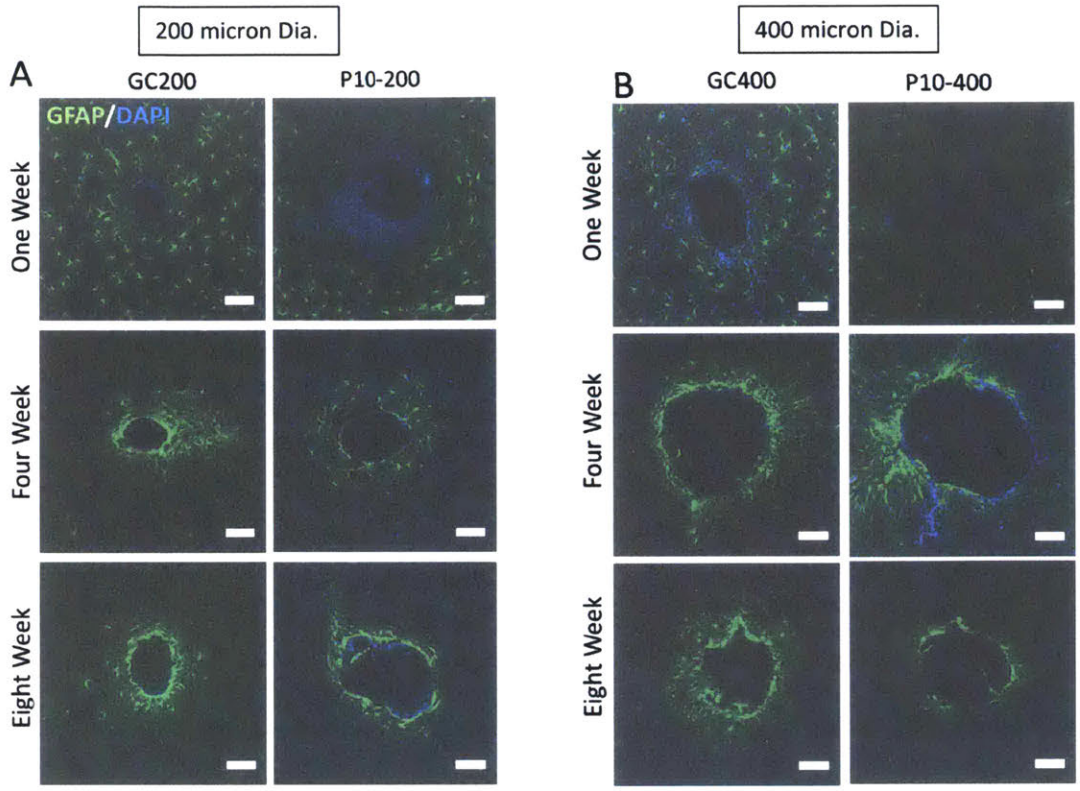

Figure 4-9 Effect of Implant Modulus on Scarring.
Representative IF images of the implant location for glass capillary implants and hydrogel coated implants with identical final diameter at 1, 4, and 8 weeks post implantation. Scale bar = 100 μm.

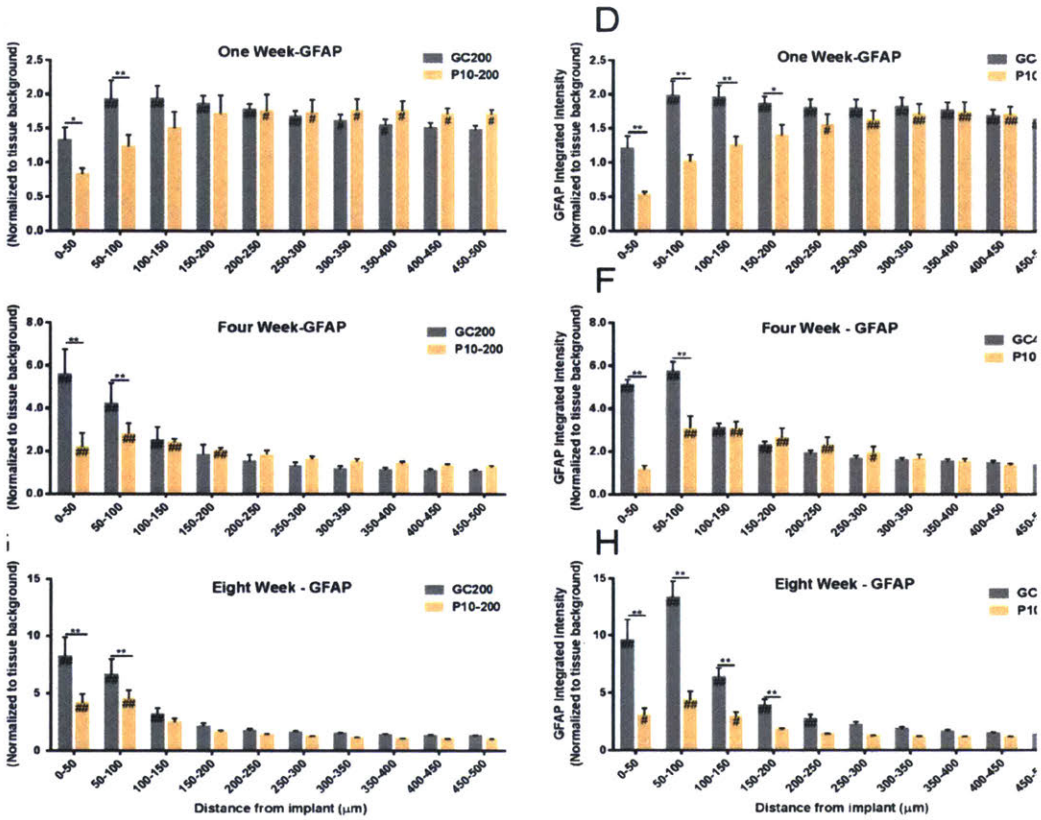

Figure 4-10 Line Profile Analysis for Size Control Hydrogel Study
*Soft implants produce less glial scarring compared to hard implants when diameter is held constant. GFAP expression was quantified as a function of distance from the device tissue interface for implants for PEG hydrogel coated implants (E≈10 kPa) and glass capillaries (E≈70 kPa) of identical diameter (d=200 um and d=400 um) at 1, 4, 8 weeks post implantation. (C,D) The average GFAP reactivity as a function of distance from the device at 1 week post implantation. (E,F) The average GFAP reactivity as a function of distance from the device at 4 weeks post implantation. (G,H) The average GFAP reactivity at eight weeks post implantation. Glial scarring was reduced for the hydrogel coated implants for both implants at all time points. **p<.01, *p<.05 indicates a statistically significant difference between cohorts at a given distance from the implant interface. ##p<.01, #p<.05 indicates a statistically significant difference compared to background. Cohort sizes (1wk, 4wk, 8 wk), GC200 = (6,5,7) P10-200 = (6,7,7), GC400 = (6,5,10), P10-400 = (6,6,6).*

4.3.3.2 Glass Capillary Size Study

GFAP:

Three different sized glass capillaries (GC150, GC200, and GC400) were implanted into the rodent brain for 1, 4, and 8 weeks in order to investigate the effect that implant diameter has on the glial scar reaction, when implant modulus is held constant. Figure 4-13 shows BF images of the glass capillaries used in this study as well as

representative IF images of the GFAP reactivity around the three different implants at 8 weeks post implantation. The size of the implant did not have a major impact on GFAP staining at one week post implantation (Figure 4-11). The GC400 had a 30% significant reduction in GFAP intensity compared to the GC150 sample in the 50 microns surrounding the implant. No other significant differences were observed at one week post implantation. At four weeks post implantation, the GC400 had a slightly larger tissue reaction compared to GC150 with a 1.4 fold increase in GFAP intensity being observed 50-100 microns away from the implant (Figure 4-12). A clear size effect in the scar reaction was observed at eight weeks post implantation (Figure 4-14). GC200 had increased GFAP staining compared to GC150 up to 100 microns away (1.5 fold increase) from the implant-tissue interface. The 400 micron capillary showed the greatest scar reaction with statistically significant increase over GC150 up to 250 microns away from the implant. The GC400 samples were observed to have a 2.3 fold increase in GFAP intensity compared to GC150 samples over this distance. GC400 had approximately 1.5 fold higher GFAP levels compared to GC200 in the 100 microns surrounding the implant.

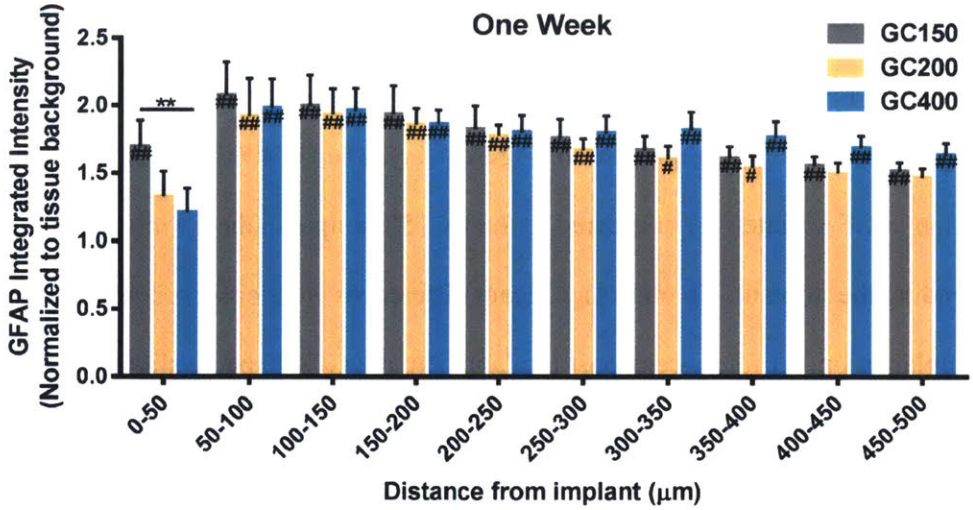

Figure 4-11 Glass Capillary Study – One Week GFAP Analysis

*Glass capillaries with diameters ranging from 150 μm to 400 μm were implanted into the rodent brain and analyzed at 1,4, and 8 weeks post implantation. This plot shows the GFAP activity as a function of distance from the implant at 1 week post implantation. **p<.01, *p<.05 indicates a statistically significant difference between cohorts at a given distance from the implant interface. ##p<.01, #p<.05 indicates a statistically significant difference compared to background.*

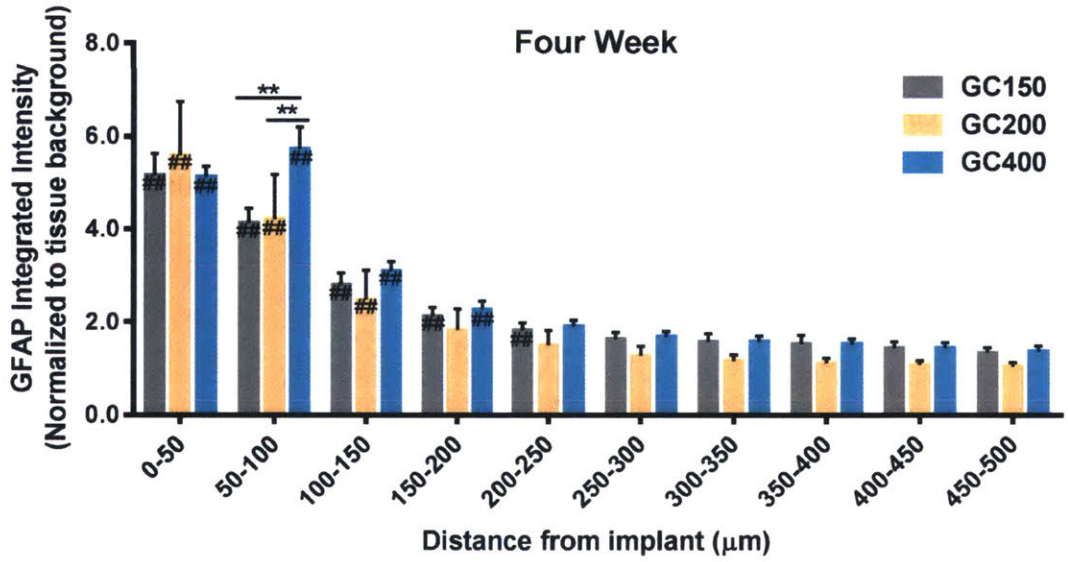

Figure 4-12 Glass Capillary Study - 4 Week GFAP Analysis

***p<.01, *p<.05 indicates a statistically significant difference between cohorts at a given distance from the implant interface. ##p<.01, #p<.05 indicates a statistically significant difference compared to background.*

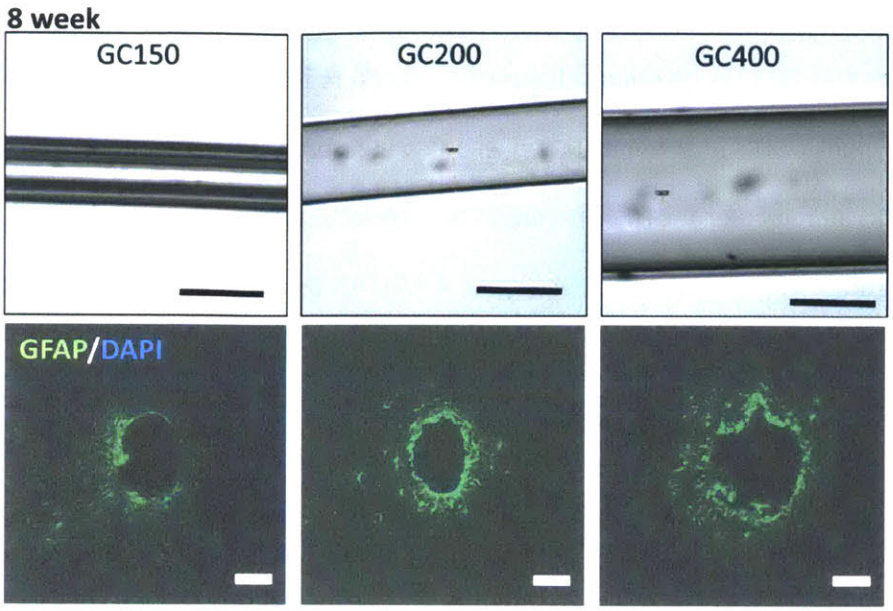

Figure 4-13 Representative Images of GFAP Reactivity around Glass Capillary Implants at 8 Weeks Post Implantation

Representative BF (scale bar =200 μm) images of the glass capillaries and IF images (scale bar (100 μm) of the GFAP reactivity at 8 weeks post implantation.

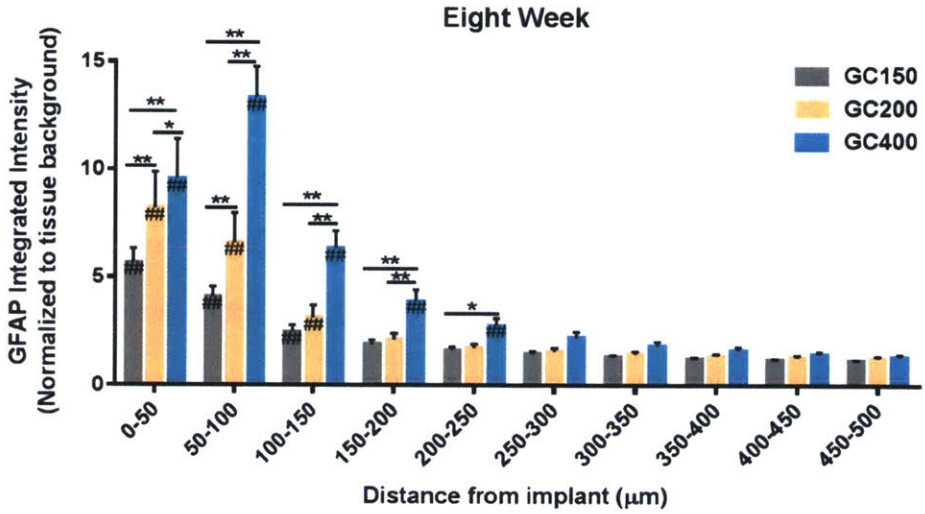

Figure 4-14 Glass Capillary Study - Eight Week GFAP Analysis

*GFAP reactivity at 8 weeks post implantation. Increased diameter (200 μm and 400 μm) implants were found to produce increased scarring at eight weeks post implantation. **p<.01, *p<.05 indicates a statistically significant difference between cohorts at a given distance from the implant interface. ##p<.01, #p<.05 indicates a statistically significant difference compared to background. Cohort sizes (1wk, 4wk, 8 wk). GC150 = (11, 11, 18), GC200 = (6,5,7), GC400 = (6,5,10).*

Additional Size Effects:

The effect that size has on other inflammatory markers including IGG, ED1/CD68, and NeuN at eight weeks post implantation was also measured. Tissue sections were stained for IGG as an indicator for BBB permeability. Tissue sections were stained for IGG and ED1 (Figure 4-15) as well as NeuN (Figure 4-17). All three diameter implants showed some evidence of elevated BBB permeability with IGG > 2.5 x of background levels in regions directly surrounding the implant (Figure 4-15). IGG values were statistically greater up to 200 μm away from the implant for all implants. Larger implants were found to have greater BBB permeability compared to the smaller diameter implants. The GC400 implant had greater a 1.5 fold increase in IgG staining up for 150 microns from the tissue interface compared to the GC150 group. The GC200 group had a 1.3 fold increase in IgG staining in the 50 microns directly surrounding the implant interface ($p<.05$) compared to the GC150 group. Implant diameter also had an effect on the presence of activated macrophages around the device-tissue interface. The GC400 group had a 1.4 fold increase ED1 staining in the 100 microns around the implant compared to the GC150 group (Figure 4-16). No statistically significant difference between the GC200 and GC150 implants was observed. Larger implants showed a slight, but statistically significant decrease in the neural nuclei density in the 100 microns surrounding the implant (Figure 4-17). In the immediate vicinity of the implant (0-50 microns away), GC150 had NeuN staining which was 65.6% of background, GC200 had NeuN staining of 56% of background, and GC400 was 51.2% of background.

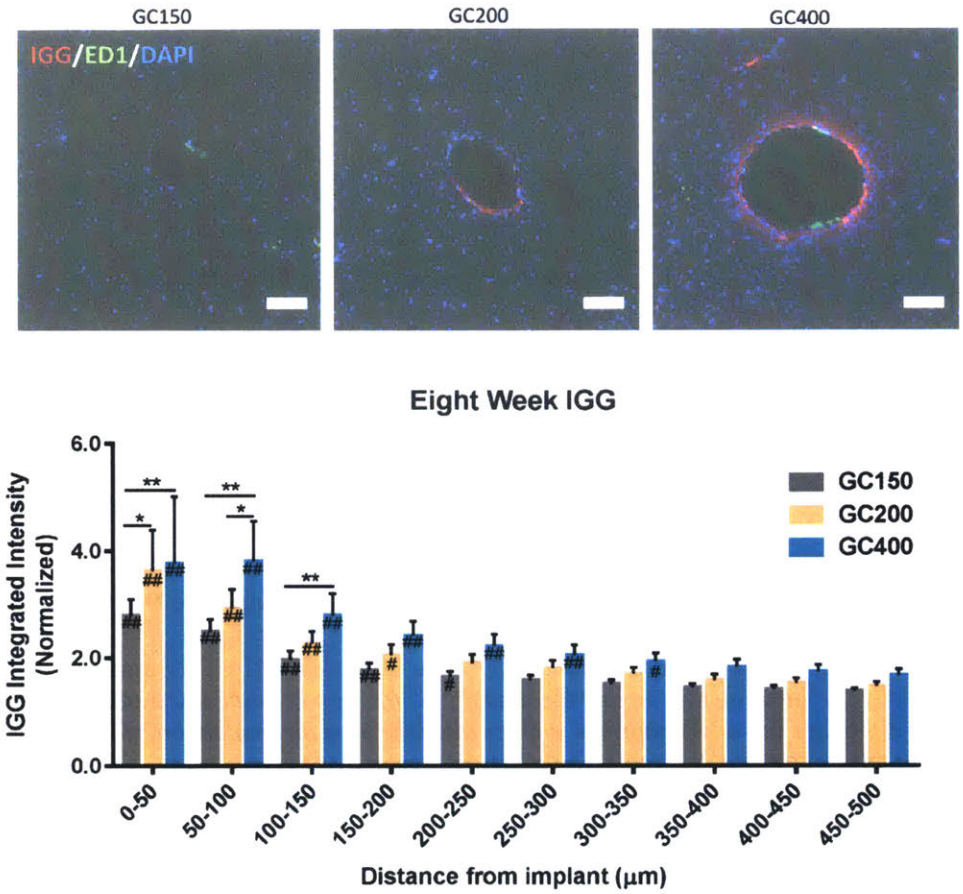

Figure 4-15 Effect of Implant Diameter on Blood Brain Barrier Permeability at Eight Weeks Post Implantation

*Representative IF images (top) of the IGG and ED1 reactivity around implants at 8 weeks post implantation (scale bar 100 μm). Glass capillary implants with increased diameter have increased IGG staining. **p<.01, *p<.05 indicates a statistically significant difference between cohorts at a given distance from the implant interface. ##p<.01, #p<.05 indicates a statistically significant difference compared to background. Cohort sizes: GC150: N = 18, GC200: N=7, GC400: N=10.*

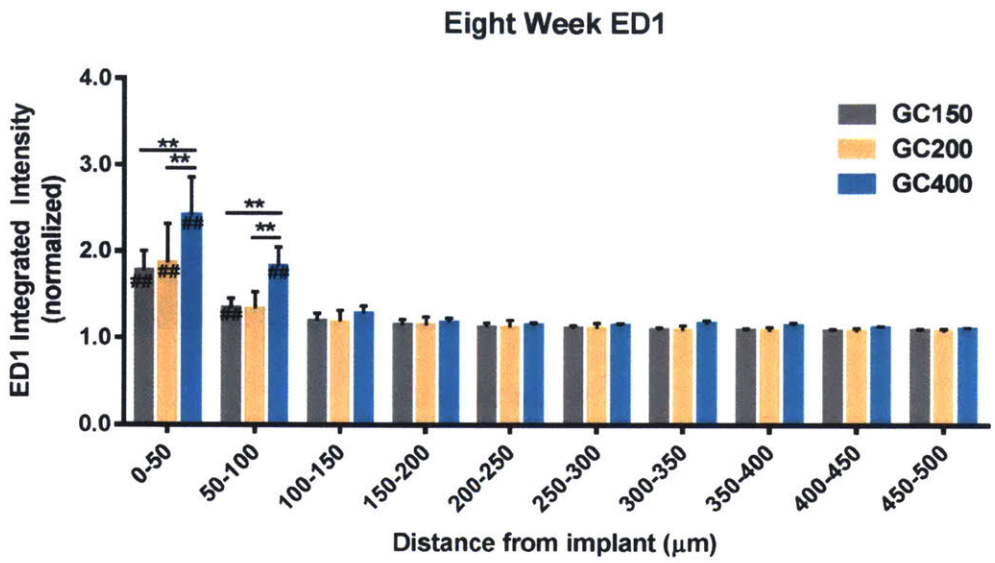

Figure 4-16 Effect of Implant Diameter on Activated Macrophage Density at Eight Weeks Post Implantation

*Glass capillary implants with increased diameter have increased ED1/CD-68 staining in the region directly surrounding the implant location. **p<.01, *p<.05 indicates a statistically significant difference between cohorts at a given distance from the implant interface. ##p<.01, #p<.05 indicates a statistically significant difference compared to background. Cohort sizes: GC150: N = 18, GC200: N=7, GC400: N=10.*

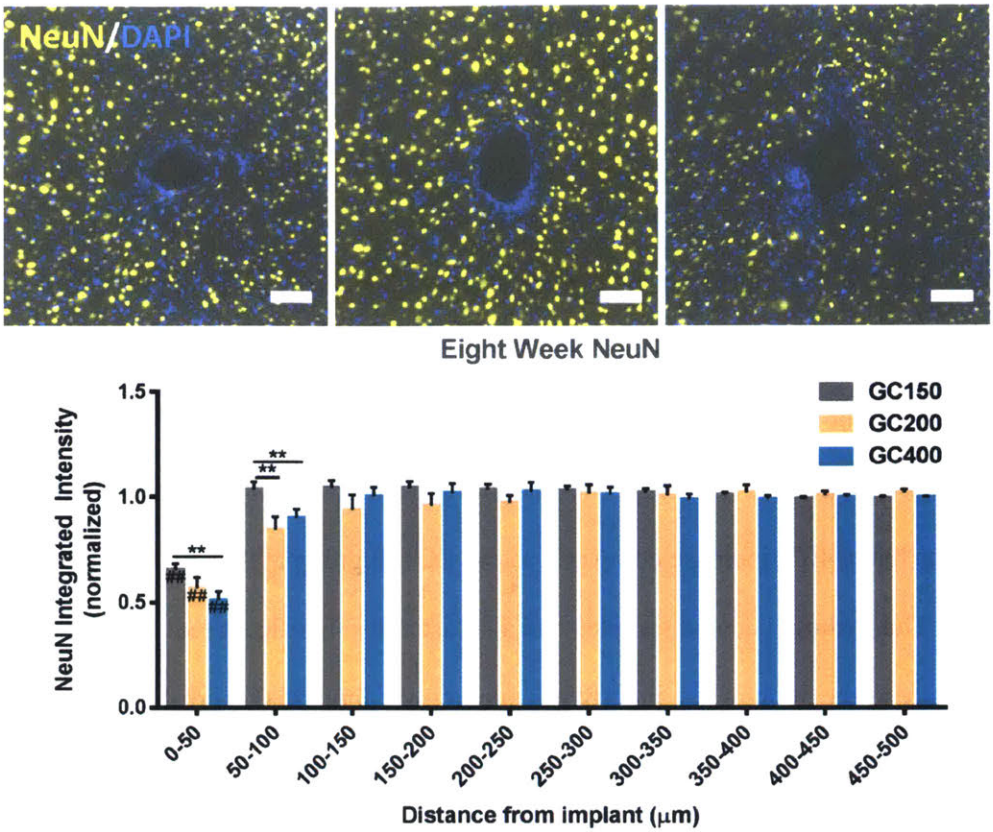

Figure 4-17 Effect of Implant Diameter on Neural Density at Eight Weeks Post Implantation.

Representative IF images of the NeuN staining around glass capillary implants at 8 weeks post implantation. (Scale bar 100 μm). Increased diameter glass capillary implants produce decreased neural density around the implant. ##p<.01, #p<.05 indicates a statistically significant difference compared to background. Cohort sizes: GC150: N = 18, GC200: N=7, GC400: N=10.

4.3.3.3 *In Vivo* Hydrogel Coating Comparison

The final comparison made in this study was between GC150 capillaries and hydrogel coated samples. At eight weeks post implantation, both the P10-200 and P10-400 hydrogel sample were found to have reduced GFAP immunoreactivity in the 50 microns directly surrounding the implant (Figure 4-18). The P10-200 group was found to have a 22% reduction compared to the GC150 capillaries. The P10-400 group was found to have a 46% reduction compared to the GC150 capillaries. There was no significant difference in regions farther from the implant between any of the three groups. The larger, hydrogel coated implants showed elevated levels of IgG in the tissue

surrounding the implant (Figure 4-19). The P10-400 group had a 1.9 fold increase in IgG staining compared to the GC150 group in the 150 μm surrounding the implants. The P10-200 group was found to have a 40% increase in IgG staining in 100-150 μm from the implant interface. Hydrogel coated samples also had a larger region with activated macrophages compared to the non-coated GC150 sample (Figure 4-20). There was no statistical difference between the three groups immediately surrounding the implant, while both hydrogel coated samples had elevated ED1 staining 50-100 microns away from the interface ($P<0.05$). The P10-200 group had a 25% increase and the P10-400 group had a 40% increase compared to the GC150 group at this distance from the implant. The hydrogel coated samples had a statistically significant reduction in neural cell density in the 50 microns directly surrounding the implant (Figure 4-21). The NeuN staining was 50% of background levels for the P10-200 group, and 48% of background for the P10-400 group, compared to 65% for the GC150 group. No differences in NeuN staining were observed farther away from the device tissue interface.

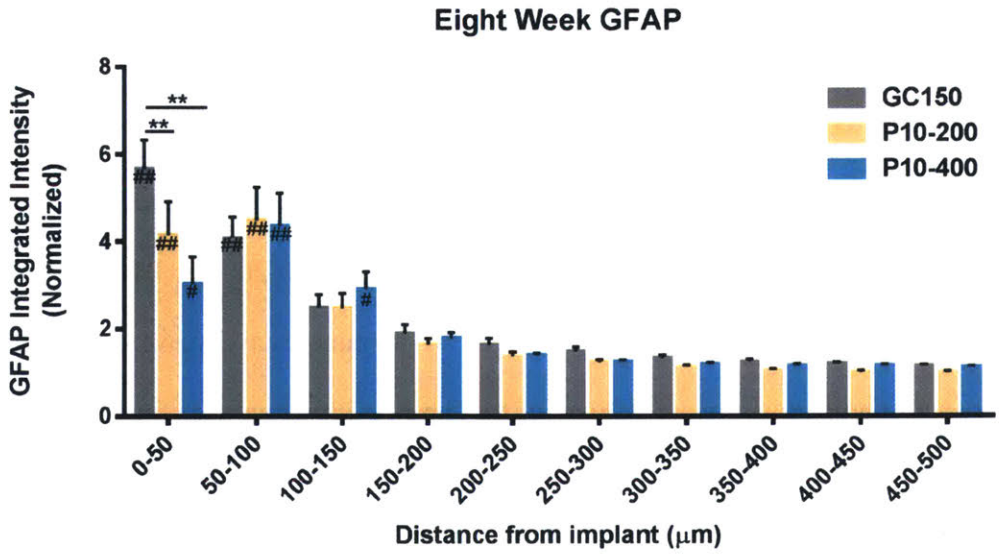

Figure 4-18 Hydrogel Coating Study – GFAP Reactivity at Eight Weeks Post Implantation

Mechanically matched hydrogel coatings reduce GFAP at 8 weeks post implantation compared to smaller diameter hard implants.

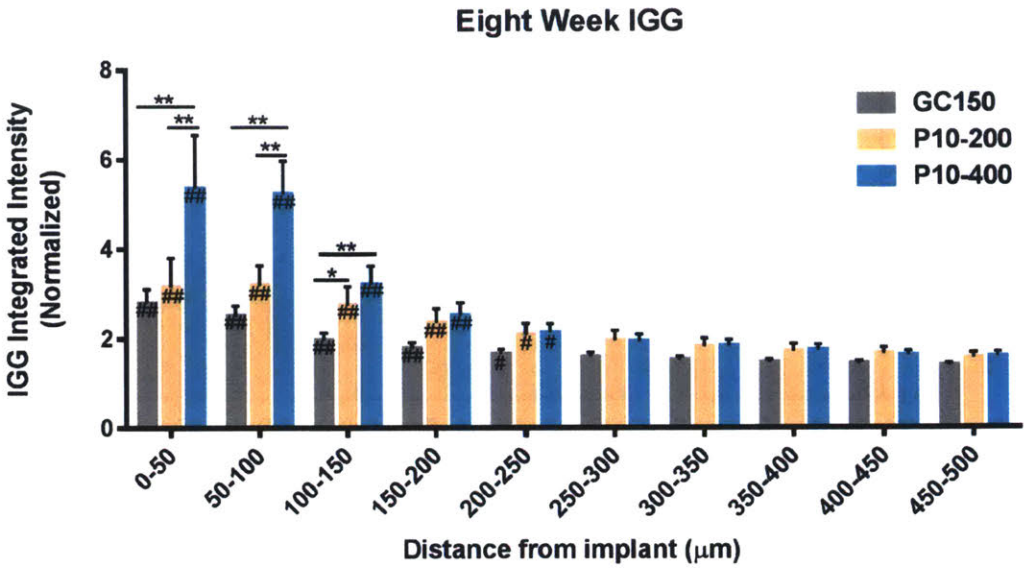

Figure 4-19 Hydrogel Coating Study - Blood Brain Barrier Permeability at Eight Weeks Post Implantation

Effects from the increased implant size were also observed. The hydrogel coated implants had increased IGG staining directly surrounding the implant,

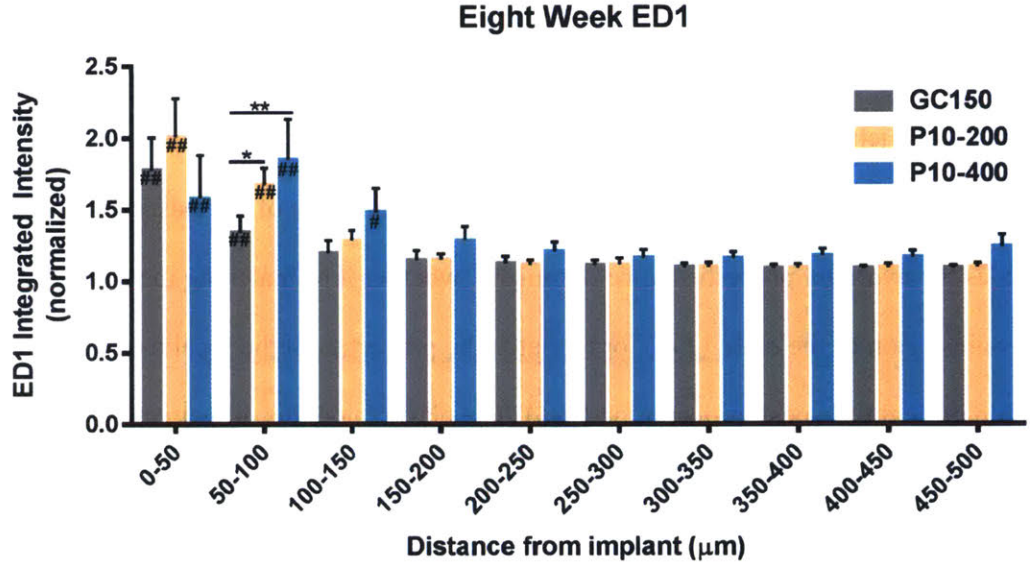

Figure 4-20 Hydrogel Coating Study – Activated Macrophage Density at Eight Weeks Post Implantation

The hydrogel coated implants had increased ED1 staining directly surrounding the implant.

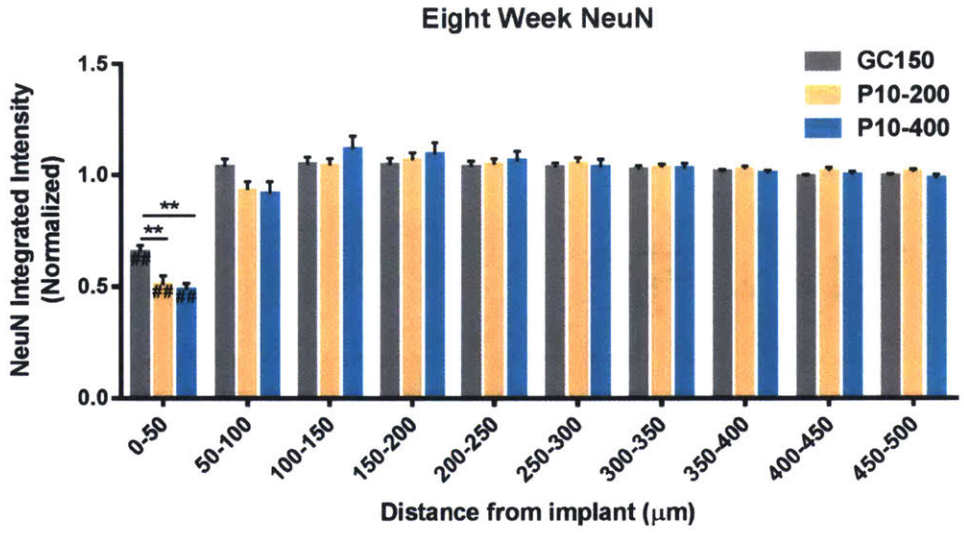

Figure 4-21 Hydrogel Coating Study – Neural Body Density at Eight Weeks Post Implantation

Hydrogel coated implants were found to have decreased neural density compared to the 150 micron diameter glass capillaries in the 50 microns directly around the implant location.

4.3.4 Discussion

The PEG-DMA hydrogels formed in this experiment have controllable mechanical properties which are on the order of brain tissue (*74*), and many orders of magnitude less than those of conventional neural implants. The tunability of the elastic properties enables the hydrogel properties to be optimized, whether it be matching the modulus to a certain region of the brain (*145*), or to match the properties of the local tissue at a certain critical time post implantation (*146*). The elastic modulus measurements and trends observed in our studies are similar to those that have been previously reported in literature (*143*). There is a significant increase in the mechanical properties as the polymer concentration increases (Figure 4-4), due to an increase in the number of physical crosslinks in the material. The modulus decreases with increasing PEG-DMA molecular weight, for a given polymer concentration. This effect is less pronounced compared to adjusting the polymer concentration, suggesting that physical crosslinks play a major factor in the molecular structure of this hydrogel. The large increase

between 10% and 20% w/v before crosslinking, is suggestive of a transition in hydrogel microstructure which has been previously described in literature (*147*).

An essential characteristic of the PEG-DMA hydrogel coating system is the ability of the coating to be dehydrated prior to implantation, preventing damage to the gel from the shear forces produced during implantation. The two minute time scale for swelling (Figure 4-3), was sufficient time to stereotactically implant the device in the region of interest. No damage was observed to coated implants when removed from the brain at the end of the experiment. The swelling observed *in vivo* may be slower than observed in the agarose gel as the free water content in brain tissue is less than the agarose tissue phantom. The time to complete swelling could be increased through addition of a soluble coating on top of the hydrogel layer. The use of a silane-methacrylate surface treatment enables the gel to be covalently bond to the surface of the implant, helping to ensure integrity of the coating throughout the duration of implantation. Both coating thicknesses investigated in this study were observed to be intact throughout the duration of implantation. No damage to the coatings was observed. The average device diameter measured in histological sections matched the approximate diameter of the hydrogel coatings suggesting that minimal damage or degradation had occurred during the implantation process and throughout the 8 week implantation period investigated in this study (Figure 4-23).

The coating process used in this study yields coatings which are conformal and have minimal variation in thickness. A similar approach could be used to coat metal implants (*148*), silicon chips (*149*), or polymer implants (*150, 151*) by slightly modifying the chemistry. The cylindrical symmetry of the devices used in this experiment lent itself well to the cast molding process. More complex geometries could

be coated with PEG-DMA hydrogels through a dip coating, or spray coating process (Figure 4-22).

A 400 micron coating thickness was used based on estimations using PEG hydrogel mechanical properties. PEG hydrogels can undergo at least 25% strain (*152*) within the elastic deformation regime, thus in order to fully absorb 30 micron displacements (typical maximum displacements observed by Gilleti et al.(*72*)), the hydrogel coating should be at least 120 microns thick according to the following equation:

$$target\ thickness = \frac{d_{micromotion}}{\varepsilon_{Max}} = \frac{30\ \mu m}{0.25} = 120\ \mu m$$

The results in a total thickness of approximately ~400 micron diameter implants (2*120 micron thick coatings + 150 micron glass).

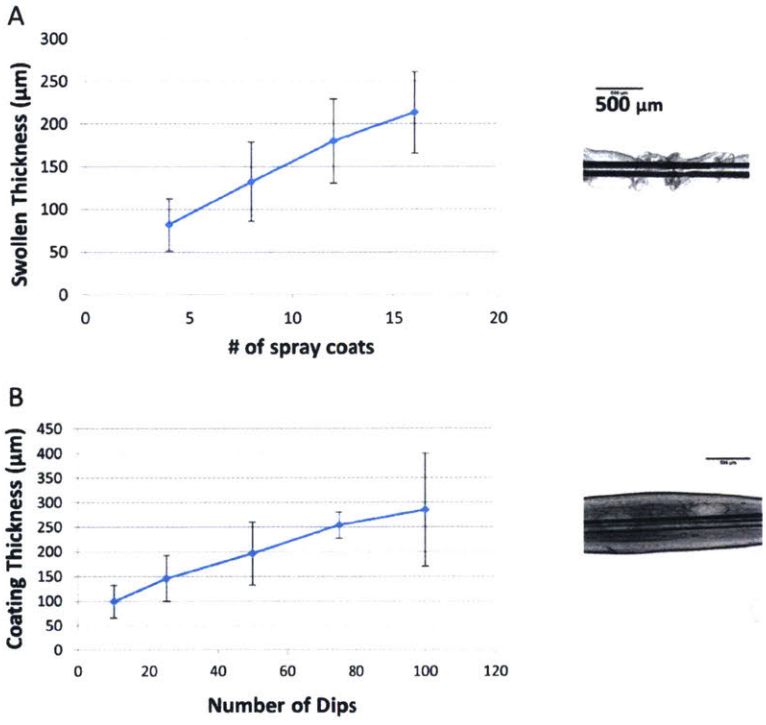

Figure 4-22 PEG-DMA Hydrogel Coatings Formed by Spray Coatings and Dip Coating

Pilot tests were conducted to demonstrate that devices could be coated via spray coating and dip coating. For each method, the thickness as a function of coat repetitions was measured via image analysis. Sample photographs are shown to the right of each plot.

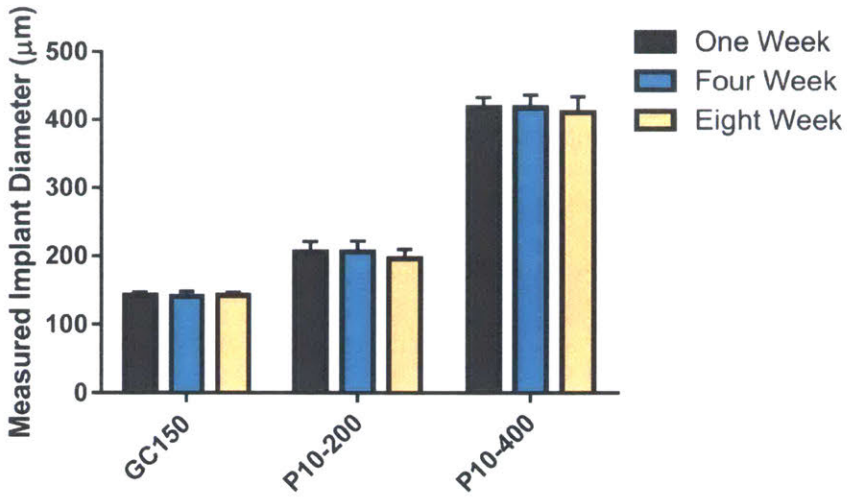

Figure 4-23 Average Implant Diameter for Hydrogel Coated Samples at One, Four, and Eight Weeks Post Implantation
The average implant diameter at the time of device removal was determined by analyzing histological sections during the imaging process. No significant decrease in coating thickness was observed over the course of implantation.

The use of an agarose brain phantom and high precision linear actuator enables the user to simulate the local effects of micromotion which are difficult to observe *in vivo*. Previous strategies to estimate micromotion effects include simulation studies (*74*), as well force measurements conducted *in vivo* (*153*). An *in vitro* approach, such as the one developed in this experiment, has advantages as it enables different engineering parameters related to device geometry and mechanical properties to be rapidly optimized without the need for large scale animal studies. The results of the strain field study clearly show that the reducing the effective elastic modulus through the addition of a thick hydrogel coating significantly reduces the local strain around the device. It is logical that these diminished strains should result in less glial reactivity and scarring around the implant based on the documented mechanical responsiveness of astrocytes (*90*). Both hydrogel thicknesses had reduced strain compared to controls in both axial and perpendicular displacement. Differing behavior was observed between the two modes of motion. The thicker P10-400 group had greater reduced strain compared to the P10-200 group when the devices were displaced perpendicular to their axis. The

increased coating thickness provided an increased mechanical buffer to reduce the strain from the micromotion. The 200 μm hydrogel produced less strain than the 400 μm hydrogel coating around the implant when the implants were displaced in the axial direction. This behavior possibly highlights the role of friction and shear between the implant and tissue when the device is displaced in the axial direction. Axial micromotion predominantly arises *in vivo* from respiration and vascular pulsation, while perpendicular displacements occur as the result of rotational accelerations (*72, 104*). These results suggest that it is important to consider both modes of displacement when incorporating features to mitigate the effects of micromotion *in vivo*.

The *in vivo* animal data presented in this study identifies several key factors that one should consider when designing neural implants to minimize scarring around neural probes. Softer implants with a lower elastic modulus produce less scarring at 1, 4, and 8 weeks post implantation (Figure 4-9) at both diameters investigated (200 micron and 400 micron). This effect has been observed in literature before in studies which demonstrated mechanically adaptive devices produce less scarring at 8 weeks post implantation (*99*). Softer implants reduce scarring due to the decrease in strain around the implant, supported by our *in vitro* data and previously conducted studies (*72, 153*). Less mechanical aggravation of the glial cells is occurring directly surrounding the implant. The relative difference between the hard and soft implants was greater in case of the 400 micron implants. The GC 400 produced 3.13x more scarring within 100 μm of the implant compared to the P10-400 implants, while the GC200 samples produced 1.7x more scarring than the P10-200 implants at 8 weeks post implantation. This is likely due in part to a greater relative difference in strain fields as the implant footprint increases.

The glass capillary study highlights the significance of neural probe diameter with regards to the chronic glial response. Larger implants have increased scarring at 8 weeks post implantation (Figure 4-14), a finding that is in line with previously published studies. Thelin et al. found that larger diameter tungsten electrodes had GFAP scarring at 6 and 12 weeks post implantation, as well as increased ED1 and decreased NeuN staining (*97*). Our findings show that the effect that size has on glial scarring becomes more pronounced at longer time points. The initial injury which is comparable between the three groups on this size scale, while the response at longer time points is dominated by differences in local strain. In addition to the increased GFAP staining, larger implants also produced greater numbers of activated macrophages, increased BBB permeability (Figure 4-15,Figure 4-16). Previous studies have suggested that soluble factors released from activated macrophages may drive changes in local BBB integrity (*154*). The increased presence of activated macrophages may also negatively affect the implant over time (11, 65). The additional inflammation for larger implants also leads to a decrease in the amount of viable neurons around the implant which could reduce the effectiveness of the implant.

The tradeoff in mechanical benefits and strain reduction must be balanced with size effects from increasing the implant footprint when considering using this materials systems as a coating (Figure 4-18, Figure 4-19, Figure 4-20, Figure 4-21). A thick, hydrogel coating reduces scarring around the implant at 8 weeks post implantation. This will provide benefits to implant function including a reduction in local impedance, an increase in drug diffusivity, and an improvement in the recording capabilities of the implant. Size effects similar to the glass capillary study, such as increased BBB permeability and increased activated macrophage presence, were observed in the larger hydrogel coatings groups. The reduction in the number neurons adjacent to the device

could also impact the ability to successfully modulate neural activity both locally and on the circuit level. Whether the decrease in neural cell density leads to a clinically significant decrease in device function, should be further investigated within the framework of the intended application. Additionally, many neural implants record primarily from the tip of the device and therefore the neural density at the just beyond the end of the device should also be considered. A reduction in scarring around the length of the device could improve recording capabilities near the tip of the device; reactive cells along the length of the device contribute to the overall inflammatory response through release of proinflammatory cytokines and ROS.

The primary focus of this study was to investigate the mechanical, and size effects of hydrogel coatings. The aqueous nature of the PEG-hydrogel formation process could, however, be adapted to encapsulate therapeutic molecules to further improve the biological response to implants. Cells (*155*), proteins (*156*), adhesion molecules (*157*), small molecule drugs (*158*) could either be linked to the hydrogel surface, or encapsulated for controlled release to further improve the biological response to the neural implant. Drug delivery strategies could be targeted to reduce macrophage activation (*108, 159*), astrocyte reactivity(*160*), or BBB permeability (*161*). Flexible implants (*79*), engineering features to reduce local strain (*78*), or mechanically adaptive composites (*99*) could be alternative strategies to capture some mechanical benefits without significantly altering the dimensions of the implant. The *in vitro* strain model discussed here would be a good tool to compare the strain reduction capabilities of each of these approaches. Addition of conducting polymers to the hydrogel could further improve the recording capabilities of the neural implant (*162*), thus diminishing the effect of displacing neurons from the probe surface.

The benefits and drawbacks of using mechanically matched coatings which significantly alter the dimensions of the implant approach should be carefully considered depending on the specific application.

4.4 Conclusion

In this study we have investigated the effect of implant modulus and diameter on the chronic reaction to neural implants by to coating conventionally hard borosilicate implants with PEG-DMA hydrogels with an elastic modulus close to that of brain tissue. Reducing the elastic modulus of neural implants leads to less scarring at chronic time points by minimizing the effects of micromotion induced strain fields around the implant. When considering coatings which significantly alter the final dimensions of the implant, there is a trade-off between the mechanical benefits of strain reduction and the increased diameter of the coating. Taken together, these results highlight the importance of both reducing the dimensions of implants as well as incorporating novel materials to reduce mechanical damage from micromotion around the implant.

The *in vivo* data suggests that optimal performance may be achieved by making implants which are both soft and are significantly smaller dimensions. There is a key trade-off with the ability to accurately implant these devices to targeted brain structures which should must be considered for this strategy. The force required for buckling/deflection of the probe during implantation is described by the Euler buckling equation:

$$F = \frac{\pi^2 E * I}{KL^2}$$

Where I is the second moment area of inertia, L is the length of the device, and E is the elastic modulus, and K is a geometric factor accounting for the support conditions of the

device. It is essential that the forces encountered during implantation remain above this value so that the probe may be accurately implanted to the desired region of interest. The moment of inertia for a rod is described as:

$$I = \frac{\pi}{2} * r^4$$

where r is the radius of the probe. Reducing diameter of the probe from 150 μm to 15 μm (putting engineering constraints aside) would result in a significantly reduced critical buckling force (approximately 10000 times less). This drastically reduced buckling force would likely result in the inability to accurately target deep brain structures. Potential solutions to overcome this problem include using larger implantation cannula (which is removed following the implantation procedure to prevent increased scarring) to guide the smaller probe, or implementing a degradable shuttle to temporarily increase the dimensions, and thus the flexible stiffness, of the device.

5 CONCLUSIONS AND FUTURE WORK

5.1 Summary of Results

A core objective of this thesis was to establish a local chemical based delivery platform for the chronic treatment of circuit diseases of the brain. Chapter 1 introduces the concept of approaching the treatment of neurological disorders from a circuit perspective and discusses possible strategies to achieve this. A successful device design should be capable of delivering nanoliter scale volumes of drug on demand to key focal points within the implicated neural circuit, while avoiding off target effects. These treatment strategies must operate for extended periods of time (months to years) following chronic implantation. Chapter 2 characterizes the chronic performance of the injectrode, a drug delivery device developed in our lab to locally modulate neural circuits through combined chemical and electrical stimulation. The results presented in this chapter demonstrate the ability to reliably deliver nanoscale volumes (10 nl – 1000 nl) of drug to interface with neural circuits both *in vitro* and *in vivo*. Muscimol, a $GABA_A$, agonist was chosen as a model drug to demonstrate the neuromodulatory potential of targeted, small volume chemical delivery. A small volume infusion of muscimol ($\approx$ 1 µl) targeted to a focal point within the basal ganglia locomotor circuit was capable of influencing the rodent's behavior for several hours post infusion. Chronic operation is an essential characteristic for optimal treatment, especially due to the invasive nature of the device implantation process. PET imaging was used to demonstrate that the device fluidics operate as intended over the course of the implantation period, with no significant changes in volume delivered over the course of implantation.

Glial scar is viewed as a major barrier to chronic neural probe function, and was the major focus of this thesis. Chapter 3 focused on evaluating the hypothesis that micromotion plays a major role in directing astrocyte reactivity to neural implants by concentrating strain fields around the implant. This hypothesis was first investigated by establishing a novel *in vitro* model, which more accurately represents the *in vivo* environment. High precision motion control was combined with advanced three dimensional cell culture techniques to simulate micromotion around neural probes. Astrocytes were found to exhibit glial scar characteristics (increased cellular area and perimeter) after one week in the presence of micromotion. The increased reactivity compared with no motion control wells, clearly demonstrates the importance of considering the mechanical effects of neural probes in the presence of micromotion. The *in vitro* model created in this section was constructed for a low cost, utilizing open source components, thus providing other researchers with a method to perform meaningful *in vitro* tests of neural probe designs.

These findings were applied in Chapter 4 to establish a strategy to improve the long term performance of the injectrode by reducing the extent of glial scarring around the implant. Hydrogel coatings with mechanical properties similar to brain tissue (E=11.6 kPa) were made on the surface of the injectrode device through a UV polymerization process. These coatings reduced the magnitude of local strain around neural probes by up to 70%, as shown within our custom *in vitro* brain phantom model. A comprehensive *in vivo* implantation study was conducted to characterize the effects of implant modulus and implant diameter on glial scarring. Reducing the implant modulus to a value close to that of brain tissue resulted in a significant reduction in scarring around the implant, when implant diameter was held constant. Increasing implant diameter, on the other hand, led to increased scarring when implant modulus was held

constant. Additional size effects due to increased implant size were also observed including increased BBB permeability, increased local macrophage staining, and decreased neural density. A combination of these two phenomenon was observed when considering the thick, mechanically matched hydrogel coatings on the injectrode. The total scarring was significantly reduced at eight weeks post implantation, although size effects from the increased diameter of the coating were also observed. The results of this experiment highlight the importance of considering the tradeoff in benefits between implant mechanical properties with changes in device dimensions when considering long term strategies to maximize the treatment of the disease.

The remainder of this chapter will discuss several potential next steps and future directions for this project.

5.2 Future Directions

5.2.1 Device Performance in Animal Disease Models

Chapter 2 focuses on the development and characterization of the fluidic connections necessary to establish reliable device performance in delivering nl-μl scale volumes of drug. It was shown that the injectrode can reliably modulate neural circuit behavior in a rodent locomotive model. Future work will explore long term device function in a range of preclinical animal models. These experiments will serve to validate device function, as well as provide a valuable opportunity to further optimize treatment efficacy before moving to clinical settings.

5.2.1.1 6-OHDA Rodent Parkinson's Model:

The first and most immediate step will be to test device function within a rodent Parkinson's model. This model is a logical next step from the behavioral model

presented in Chapter 2 as the regions of the brain, and device implantation procedures will be similar between the two experiments.

In the behavioral experiments (Section 2.2.11), muscimol was delivered to the substantia nigra (SN) to produce Parkinsonian symptoms by silencing the dopaminergic neurons which project to the striatum in the basal ganglia (*66*). The neurotoxin 6-hydroxydopamine (6-OHDA) will be infused unilaterally into medial forebrain bundle of rodents in these experiments (Figure 5-1). The infusion will be conducted following pretreatment with desipramine, so that the dopaminergic neurons within the basal ganglia circuit are selectively killed (*163*). This will deplete the dopamine concentration in the striatum on one side of the brain. The imbalance in dopamine activity between the two sides of the brain leads selectively turning in an ipsilateral direction. The degree of rotation may be enhanced through subcutaneous administration of the DA agonist D-amphetamine (*163*).

Devices and pumps primed with saline and dopamine will be implanted into the rodent striatum once the lesion effectiveness has been characterized, in a method similar to that described in chapter 2. The rodent's behavior will be monitored before and after infusion of dopamine directly into the striatum. Successful device operation will be indicated by degree of correction of the animals turning behavior. Saline control infusions will be included to confirm any observed changes in animal behavior are occurring as a result of the drug action. Local treatment efficacy may also be compared with systemic (L-Dopa) therapy to demonstrate the utility of a local approach to treat PD.

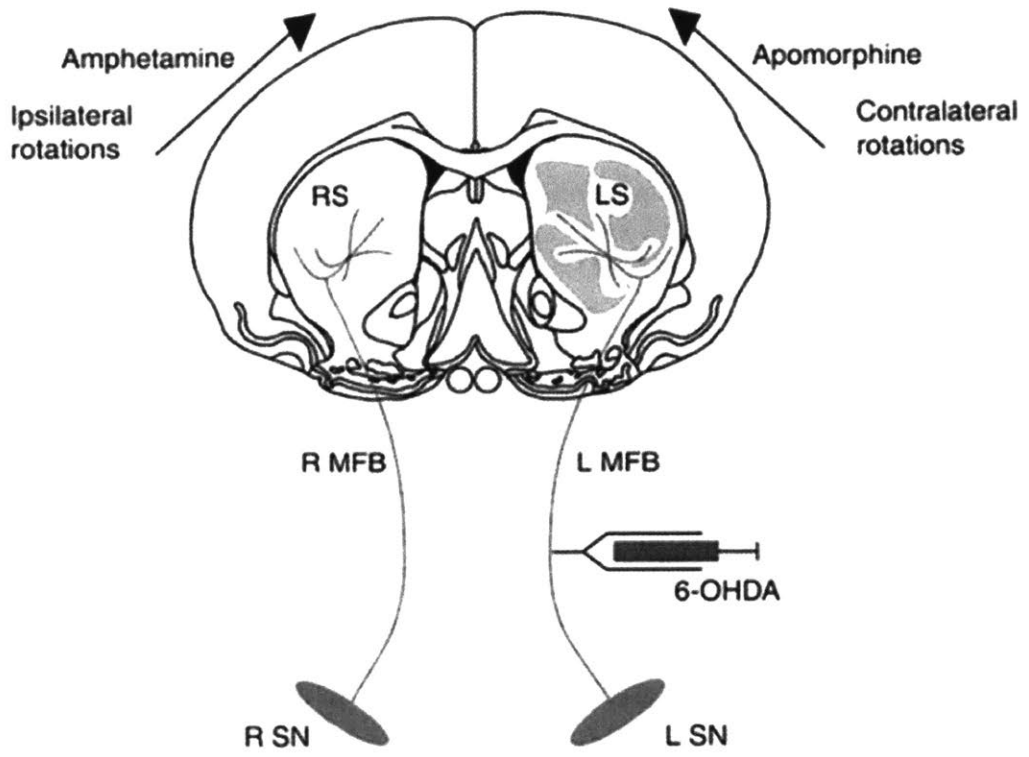

Figure 5-1 6-OHDA Rodent Parkinson's Model
A focal injection of 6-OHDA into the medial forebrain bundle leads to the selective death of the dopaminergic neurons in the nigrostriatal pathway which project to the striatum from the SN. The shaded area in the figure indicates region of DA depletion due to the lesion. (163). Animal rotational behavior will be monitored after infusion of dopamine into the striatum to confirm demonstrate device function.

5.2.1.2 Non-Human Primate Anxiety Models

Another next step in the will be to explore device operation in larger non-human primate (NHP) animal models. An advantage of the injectrode platform is the ability to scale between small and large animal models, without modification of the device design. Acute function has been demonstrated in NHP models (Figure 5-2). Chronic treatment capabilities will be assessed for in non-human primate models to demonstrate the potential to treat psychiatric disorders through rapid, precise chemical and electrical stimulation. Our collaborators in the Graybiel lab have established NHP behavioral models for anxiety (*17*). This model involves a cost-benefit decision making process in which the animal decides to receive a combination of reward and airpuff (approach), or

avoid the task all together. The boundary to the animal's decision making process, and thus the degree of their anxious behavior is identified by repeating the task for many different relative combinations for air puff and reward. Previous work has shown that local electrical microstimulation performed in a targeted region the anterior cingulate cortex (ACC) has a significant impact on the monkey's decision making process. This region of the brain has been in implicated in human anxiety disorders, depression, post-traumatic stress disorder, and addiction (*6*).

Devices will be chronically implanted into the ACC region of the trained animals. Animal performance in the behavioral task will be assessed before and after local drug infusion. Potential drug candidates include inhibitory neuromodulatory chemicals such as muscimol or drugs which are used clinically to treat anxiety (e.g. diazepam, paroxetine). It is anticipated that local infusions of these drugs will be much more efficacious than conventional systemic delivery. Drug effectiveness will be evaluated both on the ability to modulate the animal's behavior, as well as with recording electrodes implanted elsewhere within the anterior cingulate circuit (to confirm that the local stimulation is modulating the circuit wide behavior).

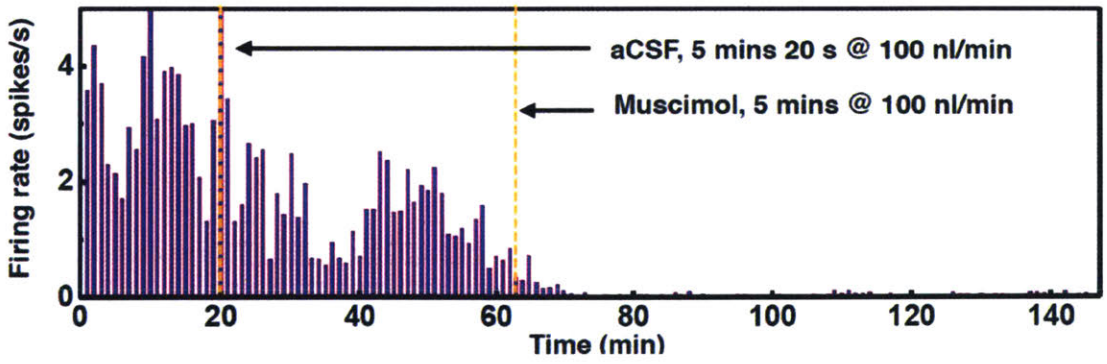

Figure 5-2 Initial Demonstration of Neural Silencing in NHP Model
Demonstration of device function in a NHP model. This plot shows the unit-firing rate as a function of time throughout the experiment. 500 µl of aCSF was infused at 20 minutes, which produced no significant change in neural activity. 500 nanolitres of muscimol was infused into a subcortical brain structure several cm deep into the brain. Muscimol is a GABA agonist which reduces the activity of the local neural tissue.

5.2.2 PET Imaging to Assess Glial Scar Characteristics:

Positron emission tomography was shown to have great utility in monitoring device function over time (Section 2.3.6). Infusions to the substantia nigra (8.5 mm below the surface) were able to be imaged longitudinally, with no significant impairment from the tissue, skull, or device fixation material. Glial scar did not have an observed effect on the device fluidic function up to eight weeks post implantation, in terms of the total volume and size of the infusion (section 2.3.6.2). These measurements were conducted with free Cu-64 in saline, which did not undergo any diffusion following infusion. This effect was likely due to the tracer being instantly bound to free proteins and/or being internalized into cells. Future work will seek to characterize how the presence of glial scar effects the distribution of more physiologically relevant molecules throughout the duration of implantation.

Thorne et al. used a method in which differing sized nanoparticles were infused to determine the effective pore size of the brain extracellular space (*61*). The diffusion coefficient was measured via integrative optical imaging for particles spanning a few orders of magnitude in diameter (0.51 nm to 35 nm). The ECS width in healthy tissue (64 nm) and hypoxic tissue (6 nm) was determined by fitting these values to a theoretical diffusion model.

A similar approach may be employed to probe the effects of glial scarring on the chronic drug delivery capabilities of the injectrode over time. Section 2.3.6.3 demonstrated the ability to label PEG molecules with Cu-64 for use in PET imaging experiments. Different size PEG molecules and/or nanoparticles of defined diameters (ranging up to ≈60 nm, the ECS width in healthy tissue) will be labeled with Cu-64, and infused into the rodent brain. Differences in clearance and diffusion rates from the initial infusion sites will be compared between molecules of different diameters to

obtain an estimate of the pore size. Measurements will be conducted immediately after implantation, as well as after scar formation (>4 weeks) to assess how the formation of glial scar affects the drug delivery capabilities of the probe.

A potential new strategy for the treatment of neurodegenerative diseases is oligonucleotide RNA therapy (*164-166*). These molecules are often encapsulated in nanoparticles to improve stability and circulation time. Poor penetration across the BBB likely requires many nanoparticles to be locally infused to the target site in the brain. There is currently no established criteria for optimal nanoparticle design for local delivery in the brain. The results of these PET infusion measurements will help provide guidance to nanoparticle treatment strategies for the treatment of neurological diseases. An effective nanoparticle treatment must be small enough in diameter so that the infusion can effectively bypass the glial scar around the implant.

5.2.3 Biocompatibility Studies

5.2.3.1 *In Vitro* Micromotion Model

Work was presented in chapter 3 which directly characterized the mechanical response of astrocytes to micromotion. The micromotion in this experiment was produced in the axial direction, which corresponds to the repetitive in/out motion that arises from respiration (*72*). Future work will seek to further expand our understanding of the role that micromotion plays in directing glial cell reactivity. More complex motions are often observed *in vivo*. There are, for example, perpendicular motions from head rotations (*104*). The model created is capable of more complex motion in both directions and with varying frequencies. Future work will characterize the response of glial cells to other modes of motion. Stress testing could be conducted in which a large

singular displacement, representative of a mild concussion, is applied to the probe (*105*).

The initial experiment was done with a micromotion magnitude of 30 μm, which simulates the motion that arises from respiration. Work will be done that characterizes the effect of smaller displacements (≈ 4μm) to replicate vascular pulsations (*72*). This work will seek to identify a threshold at which glial cells become reactive. This will help serve as a target guideline for future design strategies, which seek to mitigate the effects of micromotion.

The dynamics between different cell types could be explored in the culture at different time points. This work could involve both cocultures, as were used in the initial studies, as well as producing purified cultures of single cell population, such as astrocytes, microglia, or neurons (*95*). These experiments, taken together, will help illuminate key communication pathways which are activated by micromotion. Identification of these pathways could provide new metrics to assess device function, as well as identify potential drug targets to mitigate the effects of micromotion on driving scar formation.

The *in vitro* model may be further improved in the future by incorporating elements to make the model more representative of the *in vivo* microenvironment. This could be achieved through incorporating materials with viscoelastic properties matched to that of brain tissue (*167*) and incorporating brain ECM molecules (*106*).

5.2.3.2 *In Vivo* Biocompatibility Experiments

The experiments presented in the hydrogel coating studies (chapter 4) focused primarily on approaching the modulation of the glial scar response from a mechanical perspective. The chemical and biological properties of the implant tissue were primarily set aside, so that the role of micromotion could be rigorously characterized. Our

findings demonstrate the clear benefit in scar reduction when an implant's modulus is matched to brain tissue. This effect is due to the reduction in local strain that arises from micromotion. Potential next steps may include strategies which are directly targeted towards minimizing the size effects that were observed in the *in vivo* implantation studies. These size effects included increased BBB permeability, increased local macrophage activation, and reduced neural density around implants with increased diameter. Approaches to reduce these effects could include local drug delivery strategies, the incorporation biological molecules within the hydrogel to future improve the biocompatibility of the implants, and drastically reducing the dimensions of the device.

Local delivery of drugs may be achieved via passive release from the hydrogel coating itself (Figure 5-3). PEG hydrogels have been extensively used to release drugs in tissue engineering applications to improve cellular viability and tissue integration (*156*). Drugs which modulate neuron or glial cell behavior will be trapped within the hydrogel network during the UV polymerization process. The drugs would slowly release into the surrounding tissue via a diffusion controlled mechanism (*168*). Advantages of this approach include that the drug concentration is localized directly surrounding the implant. A clear disadvantage of using a local drug delivery approach to modulate the long term scar response is that there is a limited drug payload based on the coating dimensions. The effect that the drug has on directing cell behavior will diminish over time. One potential strategy to overcome this is to incorporate degradable linkers which temporarily bind the therapeutic to the hydrogel network, thus prolonging the therapeutic time frame (Figure 5-3b). Ashley et al. demonstrated that a β-eliminative linker could prolong drug release from an implanted PEG hydrogel for approximately 100 days (*169*). An alternative approach would be to deliver drugs locally through the

cannula of the injectrode. Delivery through the device provides an unlimited supply of therapeutic molecules, but requires the dedication of a fluidic channel. Potential drug candidates include minocycline to inhibit the activation and proliferation of microglia (*108, 159*), dexamethasone to reduce the reactivity of astrocytes (*160, 170, 171*), or resveratrol to improve BBB integrity and improve neuronal viability around the implant (*161*). Another potential strategy is to deliver protein molecules such as IL-4, which has been found to improve tissue integration in other parts of the body through shifting local macrophages to a less reactive phenotype (*107*).

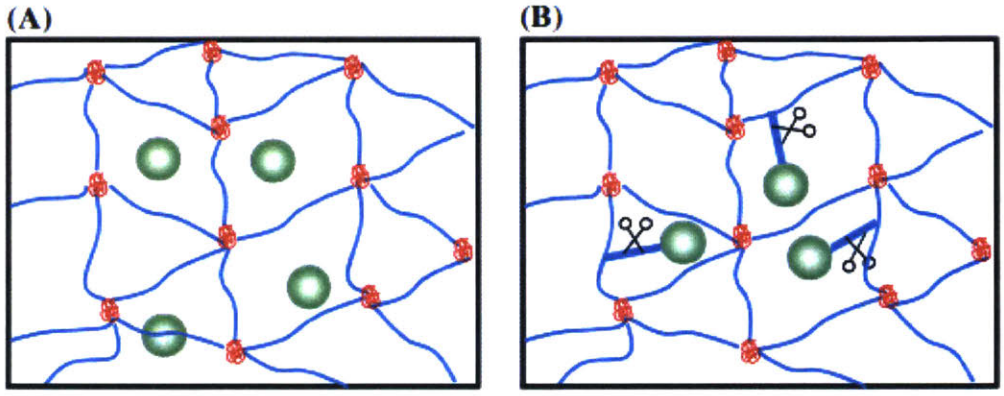

Figure 5-3 Schematic Diagram of Two Possible Hydrogel Drug Delivery Mechanisms

The drug molecules (green) can either by physically entrapped within the crosslinked polymer network (A) or chemically bonded (B) to the hydrogel structure. Release will be mediated by diffusion mechanisms, dependent on the size of the therapeutic molecule, and pore size of the hydrogel network, as well as the degradation rate of the linker in the case of the chemically bonded setup. Pure diffusion will lead to rapid release into the tissue (hours to days) while chemically bonding to the network can produce effective release up to months of implantation time. Image adapted from (156).

Another potential tactic to further improve the biocompatibility of the device is to incorporate molecules with targeted bioactivity on the surface of the coatings. Molecules which selectively improve the adhesion of certain cell populations and/or reduce the inflammatory microenvironment around the implant could be incorporated in the hydrogel formation process. Azemi et al. demonstrated that targeted peptide sequences (L1) can selectively improve the adhesion of neural cells over astrocytes/microglia (*172*). Probes coated with this peptide sequence were found to

increase neurofilament density, and decrease GFAP staining compared with uncoated controls. Other potential adhesion peptides that may be effective at improving cellular adhesion to the probe surface include IKVAV (*139*) and the general cell adhesion motif RGD (*173*). Improving the tissue integration may also improve the strain reduction from micromotion, as suggested by finite element simulations (*74*). Microglia reactivity could potentially be mitigated by incorporating anti-oxidant elements into the coating. Potter-Baker et al. demonstrated that coating neural implants with superoxide dismutase has benefits at reducing the concentrations of reactive oxygen species produced by microglial cells *in vitro* (*174*). Another strategy to combat microglia reactivity on the surface is to add anti-inflammatory peptides such as alpha melanocyte stimulating hormone (*175*) or IL-1Ra (*176*). Both of these peptides have been shown to antagonize inflammatory cytokine production when immobilized to the surface of neural probes. Combining neural adhesion strategies with elements to reduce microglia reactivity around the implant would help to eliminate the size effects that were observed in our experiments from increasing the implant diameter, thereby further improving the biocompatibility of the injectrode device.

The results of the glass capillary *in vivo* studies presented in Chapter 4 clearly demonstrate the importance of size at directing the glial scar response. Future studies should further explore this effect, particularly for capillaries of smaller dimensions ($\approx$10-50 μm range). Benefits in scar reduction due to significantly reduced device dimensions will have to be balanced with an increased fluidic resistance, as well as a decreased bending modulus.

All of the biocompatibility experiments discussed in these studies primarily involve analysis through immunohistochemical staining. Reduction in GFAP is generally viewed as the gold standard for determining if a certain strategy is viable at increasing

the neural probe's effectiveness (*69, 71*). Future experiments will seek to assess the functional benefits that incorporating mechanically matched hydrogels have on neural implant function. This will involve assessing neural recording function as well as drug diffusion characteristics. Devices with tetrodes and drug delivery fluidics will be implanted into rodents. The electrical performance will be assessed by quantifying functional recording metrics such as the signal to noise ratio (SNR) over time, impedance spectroscopy, and the ability to detect neural units throughout the course of implantation (*78*). Drug delivery capabilities will be assessed via longitudinal PET imaging. These studies will shed light into how the presence of the hydrogel coating affects the neural recording and stimulation capabilities. The electrical properties of the hydrogel coating may be improved by incorporating conductive polymers into the hydrogel network (*137, 177*).

6 REFERENCES

1. W. H. Organization, *Neurological disorders: public health challenges.* (World Health Organization, 2006).
2. L. M. L. de Lau, M. M. B. Breteler, Epidemiology of Parkinson's disease. *The Lancet Neurology* **5**, 525-535 (2006).
3. P. A. LeWitt, Levodopa for the Treatment of Parkinson's Disease. *New England Journal of Medicine* **359**, 2468-2476 (2008).
4. M. R. DeLong, T. Wichmann, Circuits and Circuit Disorders of the Basal Ganglia. *Arch Neurol* **64**, 20-24 (2007).
5. C. W. D. O. W. E. E. Kessler Rc, PRevalence, severity, and comorbidity of 12-month dsm-iv disorders in the national comorbidity survey replication. *Archives of General Psychiatry* **62**, 617-627 (2005).
6. W. C. Drevets, J. L. Price, M. L. Furey, Brain structural and functional abnormalities in mood disorders: implications for neurocircuitry models of depression. *Brain Structure and Function* **213**, 93-118 (2008).
7. K. S. Al-Harbi, Treatment-resistant depression: therapeutic trends, challenges, and future directions. *Patient preference and adherence* **6**, 369-388 (2012).
8. C. B. Nemeroff, Prevalence and management of treatment-resistant depression. *J Clin Psychiatry* **68 Suppl 8**, 17-25 (2007).
9. A. G. Purves D, Fitzpatrick D, et al., in *Neuroscience. 2nd edition.*, S. (MA), Ed. (2001).
10. D. J. Zgaljardic, J. C. Borod, N. S. Foldi, P. Mattis, A review of the cognitive and behavioral sequelae of Parkinson's disease: relationship to frontostriatal circuitry. *Cogn Behav Neurol* **16**, 193-210 (2003).
11. A. L. Brody *et al.*, Regional Brain Metabolic Changes in Patients With Major Depression Treated With Either Paroxetine or Interpersonal Therapy: Preliminary Findings. *Arch Gen Psychiatry* **58**, 631-640 (2001).
12. R. Marsh, T. V. Maia, B. S. Peterson, Functional disturbances within frontostriatal circuits across multiple childhood psychopathologies. *Am J Psychiatry* **166**, 664-674 (2009).
13. V. Gradinaru, M. Mogri, K. R. Thompson, J. M. Henderson, K. Deisseroth, Optical Deconstruction of Parkinsonian Neural Circuitry. *Science* **324**, 354-359 (2009).
14. L. Fan *et al.*, The Human Brainnetome Atlas: A New Brain Atlas Based on Connectional Architecture. *Cerebral cortex (New York, N.Y. : 1991)* **26**, 3508-3526 (2016).
15. A. H. Gittis, A. C. Kreitzer, Striatal microcircuitry and movement disorders. *Trends in neurosciences* **35**, 557-564 (2012).
16. K. M. Tye, K. Deisseroth, Optogenetic investigation of neural circuits underlying brain disease in animal models. *Nat Rev Neurosci* **13**, 251-266 (2012).

17. K.-i. Amemori, A. M. Graybiel, Localized microstimulation of primate pregenual cingulate cortex induces negative decision-making. *Nat Neurosci* **15**, 776-785 (2012).

18. S. J. Russo, E. J. Nestler, The brain reward circuitry in mood disorders. *Nat Rev Neurosci* **14**, 609-625 (2013).

19. L. Garcia, G. D'Alessandro, B. Bioulac, C. Hammond, High-frequency stimulation in Parkinson's disease: more or less? *Trends in Neurosciences* **28**, 209-216 (2005).

20. S. Fahn, The history of dopamine and levodopa in the treatment of Parkinson's disease. *Movement Disorders* **23**, S497-S508 (2008).

21. M. D. A. John Rush *et al.*, Acute and Longer-Term Outcomes in Depressed Outpatients Requiring One or Several Treatment Steps: A STAR*D Report. *American Journal of Psychiatry* **163**, 1905-1917 (2006).

22. N. J. Abbott, I. A. Romero, Transporting therapeutics across the blood-brain barrier. *Mol Med Today* **2**, 106-113 (1996).

23. D. R. Groothuis, The blood-brain and blood-tumor barriers: A review of strategies for increasing drug delivery. *Neuro-Oncology* **2**, 45-59 (2000).

24. W. M. Pardridge, Drug and gene targeting to the brain with molecular trojan horses. *Nat Rev Drug Discov* **1**, 131-139 (2002).

25. D. R. Groothuis *et al.*, The Effect of an Amino Acid-lowering Diet on the Rate of Melphalan Entry into Brain and Xenotransplanted Glioma. *Cancer Research* **52**, 5590-5596 (1992).

26. S. I. Rapoport, H. K. Thompson, Osmotic Opening of the Blood-Brain Barrier in the Monkey without Associated Neurological Deficits. *Science* **180**, 971 (1973).

27. J. Jankovic, L. G. Aguilar, Current approaches to the treatment of Parkinson's disease. *Neuropsychiatric Disease and Treatment* **4**, 743-757 (2008).

28. K. Noyes, H. Liu, R. G. Holloway, What is the risk of developing parkinsonism following neuroleptic use? *Neurology* **66**, 941-943 (2006).

29. R. H. Bobo *et al.*, Convection-enhanced delivery of macromolecules in the brain. *Proc Natl Acad Sci U S A* **91**, 2076-2080 (1994).

30. D. S. Bidros, Future of convection-enhanced delivery in the treatment of Brain Tumors. *Future Oncology* **6**, (2010).

31. W. Debinski, S. B. Tatter, Convection-enhanced delivery for the treatment of brain tumors. *Expert Rev Neurother* **9**, 1519-1527 (2009).

32. T. Kikuchi *et al.*, Convection-enhanced delivery of polyethylene glycol-coated liposomal doxorubicin: characterization and efficacy in rat intracranial glioma models. *J Neurosurg* **109**, 867-873 (2008).

33. R. Raghavan *et al.*, Convection-enhanced delivery of therapeutics for brain disease, and its optimization. *Neurosurgical Focus* **20**, E12 (2006).

34. M. A. Rogawski, Convection-enhanced delivery in the treatment of epilepsy. *Neurotherapeutics* **6**, 344-351 (2009).

35. S. Miocinovic, S. Somayajula, S. Chitnis, J. L. Vitek, HIstory, applications, and mechanisms of deep brain stimulation. *JAMA Neurology* **70**, 163-171 (2013).

36. L. Fenno, O. Yizhar, K. Deisseroth, The development and application of optogenetics. *Annual review of neuroscience* **34**, 389-412 (2011).

37. D. J. Urban, B. L. Roth, DREADDs (Designer Receptors Exclusively Activated by Designer Drugs): Chemogenetic Tools with Therapeutic Utility. *Annual Review of Pharmacology and Toxicology* **55**, 399-417 (2015).

38. J. C. Williams, T. Denison, From Optogenetic Technologies to Neuromodulation Therapies. *Science Translational Medicine* **5**, 177ps176-177ps176 (2013).

39. H.-C. Cheng, C. M. Ulane, R. E. Burke, Clinical Progression in Parkinson's Disease and the Neurobiology of Axons. *Annals of neurology* **67**, 715-725 (2010).

40. H. Bernheimer, W. Birkmayer, O. Hornykiewicz, K. Jellinger, F. Seitelberger, Brain dopamine and the syndromes of Parkinson and Huntington. Clinical, morphological and neurochemical correlations. *Journal of the neurological sciences* **20**, 415-455 (1973).

41. A. M. Owen, Cognitive Dysfunction in Parkinson's Disease: The Role of Frontostriatal Circuitry. *The Neuroscientist* **10**, 525-537 (2004).

42. O. Rascol *et al.*, A Five-Year Study of the Incidence of Dyskinesia in Patients with Early Parkinson's Disease Who Were Treated with Ropinirole or Levodopa. *New England Journal of Medicine* **342**, 1484-1491 (2000).

43. William R. Stauffer *et al.*, Dopamine Neuron-Specific Optogenetic Stimulation in Rhesus Macaques. *Cell* **166**, 1564-1571.e1566.

44. R. V. Shannon, A model of safe levels for electrical stimulation. *Biomedical Engineering, IEEE Transactions on* **39**, 424-426 (1992).

45. M. Fiandaca, J. Forsayeth, P. Dickinson, K. Bankiewicz, Image-guided convection-enhanced delivery platform in the treatment of neurological diseases. *Neurotherapeutics* **5**, 123-127 (2008).

46. J. D. Heiss, S. Walbridge, A. R. Asthagiri, R. R. Lonser, Image-guided convection-enhanced delivery of muscimol to the primate brain. *Journal of Neurosurgery* **112**, 790-795 (2009).

47. C. Foley, N. Nishimura, K. Neeves, C. Schaffer, W. Olbricht, Flexible microfluidic devices supported by biodegradable insertion scaffolds for convection-enhanced neural drug delivery. *Biomedical Microdevices* **11**, 915-924 (2009).

48. E. Sykova, C. Nicholson, Diffusion in brain extracellular space. *Physiol Rev* **88**, 1277-1340 (2008).

49. D. Chandra *et al.*, Prototypic GABA(A) Receptor Agonist Muscimol Acts Preferentially Through Forebrain High-Affinity Binding Sites. *Neuropsychopharmacology* **35**, 999-1007 (2010).

50. Daniel S. Kohane *et al.*, Effectiveness of Muscimol-containing Microparticles against Pilocarpine-induced Focal Seizures. *Epilepsia* **43**, 1462-1468 (2002).

51. K. B. Neeves, C. T. Lo, C. P. Foley, W. M. Saltzman, W. L. Olbricht, Fabrication and characterization of microfluidic probes for convection enhanced drug delivery. *Journal of Controlled Release* **111**, 252-262 (2006).

52. C. Nicholson, L. Tao, Hindered diffusion of high molecular weight compounds in brain extracellular microenvironment measured with integrative optical imaging. *Biophysical Journal* **65**, 2277-2290 (1993).

53. G. Paxinos, C. R. Watson, P. C. Emson, AChE-stained horizontal sections of the rat brain in stereotaxic coordinates. *Journal of neuroscience methods* **3**, 129-149 (1980).

54. A. Prasad *et al.*, Comprehensive characterization and failure modes of tungsten microwire arrays in chronic neural implants. *J Neural Eng* **9**, 056015 (2012).

55. V. Sankar *et al.*, Electrode impedance analysis of chronic tungsten microwire neural implants: understanding abiotic vs. biotic contributions. *Frontiers in Neuroengineering* **7**, (2014).

56. J. C. Williams, J. A. Hippensteel, J. Dilgen, W. Shain, D. R. Kipke, Complex impedance spectroscopy for monitoring tissue responses to inserted neural implants. *J Neural Eng* **4**, 410-423 (2007).

57. P. Abhishek, C. S. Justin, Quantifying long-term microelectrode array functionality using chronic in vivo impedance testing. *Journal of Neural Engineering* **9**, 026028 (2012).

58. S. S. Gambhir, Molecular imaging of cancer with positron emission tomography. *Nat Rev Cancer* **2**, 683-693 (2002).

59. E. Syková, T. Mazel, L. Vargová, I. Voříšek, Š. Prokopová-Kubinová, in *Progress in brain research,* K. F. C. N. E. S. L.F. Agnati, Ed. (Elsevier, 2000), vol. Volume 125, pp. 155-178.

60. R. G. Thorne, A. Lakkaraju, E. Rodriguez-Boulan, C. Nicholson, In vivo diffusion of lactoferrin in brain extracellular space is regulated by interactions with heparan sulfate. *Proceedings of the National Academy of Sciences* **105**, 8416-8421 (2008).

61. R. G. Thorne, C. Nicholson, In vivo diffusion analysis with quantum dots and dextrans predicts the width of brain extracellular space. *Proceedings of the National Academy of Sciences* **103**, 5567-5572 (2006).

62. T. Bonnevie *et al.*, Grid cells require excitatory drive from the hippocampus. *Nat Neurosci* **16**, 309-317 (2013).

63. C. M. Gray, P. E. Maldonado, M. Wilson, B. McNaughton, Tetrodes markedly improve the reliability and yield of multiple single-unit isolation from multi-unit recordings in cat striate cortex. *J Neurosci Methods* **63**, 43-54 (1995).

64. R. Pomfret, K. Sillay, G. Miranpuri, Investigation of the electrical properties of agarose gel: characterization of concentration using nyquist plot phase angle and the implications of a more comprehensive in vitro model of the brain. *Annals of Neurosciences* **20**, 99-107 (2013).

65. S. F. Cogan, Neural Stimulation and Recording Electrodes. *Annual Review of Biomedical Engineering* **10**, 275-309 (2008).

66. G. E. Martin, N. L. Papp, C. B. Bacino, Contralateral turning evoked by the intranigral microinjection of muscimol and other GABA agonists. *Brain Research* **155**, 297-312 (1978).

67. J. L. Hudson *et al.*, Correlation of apomorphine- and amphetamine-induced turning with nigrostriatal dopamine content in unilateral 6-hydroxydopamine lesioned rats. *Brain Research* **626**, 167-174 (1993).

68. G. Kook, S. Lee, H. Lee, I.-J. Cho, H. Lee, Neural Probes for Chronic Applications. *Micromachines* **7**, 179 (2016).

69. V. S. Polikov, P. A. Tresco, W. M. Reichert, Response of brain tissue to chronically implanted neural electrodes. *Journal of Neuroscience Methods* **148**, 1-18 (2005).

70. J. Mehdi, L. S. John, W. Christoph, R. C. Jeffrey, Progress towards biocompatible intracortical microelectrodes for neural interfacing applications. *Journal of Neural Engineering* **12**, 011001 (2015).

71. D. Prodanov, J. Delbeke, Mechanical and Biological Interactions of Implants with the Brain and Their Impact on Implant Design. *Frontiers in Neuroscience* **10**, (2016).

72. G. Aaron, M. Jit, Brain micromotion around implants in the rodent somatosensory cortex. *Journal of Neural Engineering* **3**, 189 (2006).

73. L. Hyunjung, V. B. Ravi, S. Wei, E. L. Marc, Biomechanical analysis of silicon microelectrode-induced strain in the brain. *Journal of Neural Engineering* **2**, 81 (2005).

74. S. Jeyakumar, C. M. David, R. K. Daryl, A finite-element model of the mechanical effects of implantable microelectrodes in the cerebral cortex. *Journal of Neural Engineering* **2**, 103 (2005).

75. R. Biran, D. C. Martin, P. A. Tresco, The brain tissue response to implanted silicon microelectrode arrays is increased when the device is tethered to the skull. *Journal of Biomedical Materials Research Part A* **82A**, 169-178 (2007).

76. T. Saxena *et al.*, The impact of chronic blood–brain barrier breach on intracortical electrode function. *Biomaterials* **34**, 4703-4713 (2013).

77. S. Musallam, M. J. Bak, P. R. Troyk, R. A. Andersen, A floating metal microelectrode array for chronic implantation. *Journal of Neuroscience Methods* **160**, 122-127 (2007).

78. H. S. Sohal *et al.*, The sinusoidal probe: a new approach to improve electrode longevity. *Frontiers in Neuroengineering* **7**, (2014).

79. A. Canales *et al.*, Multifunctional fibers for simultaneous optical, electrical and chemical interrogation of neural circuits in vivo. *Nat Biotech* **advance online publication**, (2015).

80. D. M. Simon *et al.*, Design and demonstration of an intracortical probe technology with tunable modulus. *Journal of Biomedical Materials Research Part A*, n/a-n/a (2016).

81. M. Jorfi, G. Voirin, E. J. Foster, C. Weder, Physiologically responsive, mechanically adaptive polymer optical fibers for optogenetics. *Opt. Lett.* **39**, 2872-2875 (2014).

82. V. S. Polikov, M. L. Block, J.-M. Fellous, J.-S. Hong, W. M. Reichert, In vitro model of glial scarring around neuroelectrodes chronically implanted in the CNS. *Biomaterials* **27**, 5368-5376 (2006).

83. A. M. Hopkins, E. DeSimone, K. Chwalek, D. L. Kaplan, 3D in vitro modeling of the central nervous system. *Progress in Neurobiology* **125**, 1-25 (2015).

84. T. B. Puschmann, Y. de Pablo, C. Zandén, J. Liu, M. Pekny, A Novel Method for Three-Dimensional Culture of Central Nervous System Neurons. *Tissue Engineering Part C: Methods* **20**, 485-492 (2013).

85. M. C. LaPlaca, V. N. Vernekar, J. T. Shoemaker, D. K. Cullen, Three-dimensional neuronal cultures. *Methods in Bioengineering: 3D Tissue Engineering. Artech House Publishers, London*, (2010).

86. E. East, J. P. Golding, J. B. Phillips, A versatile 3D culture model facilitates monitoring of astrocytes undergoing reactive gliosis. *Journal of Tissue Engineering and Regenerative Medicine* **3**, 634-646 (2009).

87. C. I. Ugbode, W. D. Hirst, M. Rattray, Astrocytes Grown in Alvetex® Three Dimensional Scaffolds Retain a Non-reactive Phenotype. *Neurochemical Research* **41**, 1857-1867 (2016).

88. T. B. Puschmann *et al.*, Bioactive 3D cell culture system minimizes cellular stress and maintains the in vivo-like morphological complexity of astroglial cells. *Glia* **61**, 432-440 (2013).

89. A. F. Jeffery, M. A. Churchward, V. K. Mushahwar, K. G. Todd, A. L. Elias, Hyaluronic Acid-Based 3D Culture Model for In Vitro Testing of Electrode Biocompatibility. *Biomacromolecules* **15**, 2157-2165 (2014).

90. L. Karumbaiah *et al.*, The upregulation of specific interleukin (IL) receptor antagonists and paradoxical enhancement of neuronal apoptosis due to electrode induced strain and brain micromotion. *Biomaterials* **33**, 5983-5996 (2012).

91. M. C. LaPlaca, D. K. Cullen, J. J. McLoughlin, R. S. Cargill Ii, High rate shear strain of three-dimensional neural cell cultures: a new in vitro traumatic brain injury model. *Journal of Biomechanics* **38**, 1093-1105 (2005).

92. S. I. Jeong *et al.*, Mechano-active tissue engineering of vascular smooth muscle using pulsatile perfusion bioreactors and elastic PLCL scaffolds. *Biomaterials* **26**, 1405-1411 (2005).

93. M. Sladkova, G. de Peppo, Bioreactor Systems for Human Bone Tissue Engineering. *Processes* **2**, 494 (2014).

94. B. D. Riehl, J.-H. Park, I. K. Kwon, J. Y. Lim, Mechanical Stretching for Tissue Engineering: Two-Dimensional and Three-Dimensional Constructs. *Tissue Engineering. Part B, Reviews* **18**, 288-300 (2012).

95. B. Liu, J. S. Hong, Primary rat mesencephalic neuron-glia, neuron-enriched, microglia-enriched, and astroglia-enriched cultures. *Methods Mol Med* **79**, 387-395 (2003).

96. V. S. Polikov, E. C. Su, M. A. Ball, J.-S. Hong, W. M. Reichert, CONTROL PROTOCOL FOR ROBUST IN VITRO GLIAL SCAR FORMATION AROUND MICROWIRES: ESSENTIAL ROLES OF BFGF AND SERUM IN GLIOSIS. *Journal of neuroscience methods* **181**, 170-177 (2009).

97. J. Thelin *et al.*, Implant size and fixation mode strongly influence tissue reactions in the CNS. *PLoS One* **6**, e16267 (2011).

98. P. Köhler *et al.*, Influence of Probe Flexibility and Gelatin Embedding on Neuronal Density and Glial Responses to Brain Implants. *PLoS ONE* **10**, e0119340 (2015).

99. J. K. Nguyen *et al.*, Mechanically-compliant intracortical implants reduce the neuroinflammatory response. *Journal of Neural Engineering* **11**, 056014 (2014).

100. A. Schander *et al.*, Design and fabrication of novel multi-channel floating neural probes for intracortical chronic recording. *Sensors and Actuators A: Physical* **247**, 125-135 (2016).

101. A. P. Kelsey, C. B. Amy, K. S. Wade, R. C. Jeffrey, Stab injury and device implantation within the brain results in inversely multiphasic neuroinflammatory and neurodegenerative responses. *Journal of Neural Engineering* **9**, 046020 (2012).

102. M. Ravikumar *et al.*, The roles of blood-derived macrophages and resident microglia in the neuroinflammatory response to implanted Intracortical microelectrodes. *Biomaterials* **35**, 8049-8064 (2014).

103. K. S. Parthasarathy *et al.*, Biocompatibilities of sapphire and borosilicate glass as cortical neuroprostheses. *Magnetic Resonance Imaging* **25**, 1333-1340 (2007).

104. M. S. Fee, Active Stabilization of Electrodes for Intracellular Recording in Awake Behaving Animals. *Neuron* **27**, 461-468 (2000).

105. P. V. Bayly *et al.*, Deformation of the Human Brain Induced by Mild Acceleration. *Journal of neurotrauma* **22**, 845-856 (2005).

106. T.-W. Wang, M. Spector, Development of hyaluronic acid-based scaffolds for brain tissue engineering. *Acta Biomaterialia* **5**, 2371-2384 (2009).

107. D. Hachim, S. T. LoPresti, C. C. Yates, B. N. Brown, Shifts in macrophage phenotype at the biomaterial interface via IL-4 eluting coatings are associated with improved implant integration. *Biomaterials* **112**, 95-107 (2017).

108. R. L. Rennaker, J. Miller, H. Tang, D. A. Wilson, Minocycline increases quality and longevity of chronic neural recordings. *Journal of Neural Engineering* **4**, L1 (2007).

109. L. Spataro *et al.*, Dexamethasone treatment reduces astroglia responses to inserted neuroprosthetic devices in rat neocortex. *Experimental Neurology* **194**, 289-300 (2005).

110. F. A. Ponce, A. M. Lozano, in *Progress in brain research,* B. Anders, M. A. Cenci, Eds. (Elsevier, 2010), vol. Volume 184, pp. 311-324.

111. P. Krack, M. I. Hariz, C. Baunez, J. Guridi, J. A. Obeso, Deep brain stimulation: from neurology to psychiatry? *Trends in Neurosciences* **33**, 474-484 (2010).

112. J. M. Bronstein *et al.*, Deep Brain Stimulation for Parkinson Disease: An Expert Consensus and Review of Key Issues. *Arch Neurol* **68**, 165- (2011).

113. Andres M. Lozano, N. Lipsman, Probing and Regulating Dysfunctional Circuits Using Deep Brain Stimulation. *Neuron* 77, 406-424 (2013).

114. J. J. Daly, J. R. Wolpaw, Brain–computer interfaces in neurological rehabilitation. *The Lancet Neurology* 7, 1032-1043 (2008).

115. R. A. Normann, Technology Insight: future neuroprosthetic therapies for disorders of the nervous system. *Nat Clin Pract Neuro* **3**, 444-452 (2007).

116. M. A. L. Nicolelis, Brain-machine interfaces to restore motor function and probe neural circuits. *Nat Rev Neurosci* **4**, 417-422 (2003).

117. P. Rohatgi, N. B. Langhals, D. R. Kipke, P. G. Patil, In vivo performance of a microelectrode neural probe with integrated drug delivery. *Neurosurgical Focus* **27**, E8 (2009).

118. N. V. Thakor, Translating the Brain-Machine Interface. *Science Translational Medicine* **5**, 210ps217-210ps217 (2013).

119. P. Takmakov *et al.*, Rapid evaluation of the durability of cortical neural implants using accelerated aging with reactive oxygen species. *Journal of Neural Engineering* **12**, (2015).

120. E. Syková, L. Vargová, Š. Prokopová, Z. Šimonová, Glial swelling and astrogliosis produce diffusion barriers in the rat spinal cord. *Glia* **25**, 56-70 (1999).

121. J. L. Ridet, A. Privat, S. K. Malhotra, F. H. Gage, Reactive astrocytes: cellular and molecular cues to biological function. *Trends in Neurosciences* **20**, 570-577 (1997).

122. J. N. Turner *et al.*, Cerebral Astrocyte Response to Micromachined Silicon Implants. *Experimental Neurology* **156**, 33-49 (1999).

123. D. H. Szarowski *et al.*, Brain responses to micro-machined silicon devices. *Brain Research* **983**, 23-35 (2003).

124. R. Farra *et al.*, First-in-Human Testing of a Wirelessly Controlled Drug Delivery Microchip. *Science Translational Medicine* **4**, 122ra121 (2012).

125. G. Voskerician, L. Chung-Chiun, J. M. Anderson, Electrochemical characterization and in vivo biocompatibility of a thick-film printed sensor for continuous in vivo monitoring. *Sensors Journal, IEEE* **5**, 1147-1158 (2005).

126. J. M. Anderson, A. Rodriguez, D. T. Chang, Foreign body reaction to biomaterials. *Seminars in Immunology* **20**, 86-100 (2008).

127. A. Rolls, R. Shechter, M. Schwartz, The bright side of the glial scar in CNS repair. *Nat Rev Neurosci* **10**, 235-241 (2009).

128. J. Silver, J. H. Miller, Regeneration beyond the glial scar. *Nat Rev Neurosci* **5**, 146-156 (2004).

129. P. J. Rousche, R. A. Normann, Chronic recording capability of the Utah Intracortical Electrode Array in cat sensory cortex. *J Neurosci Methods* **82**, 1-15 (1998).

130. D. R. Kipke, R. J. Vetter, J. C. Williams, J. F. Hetke, Silicon-substrate intracortical microelectrode arrays for long-term recording of neuronal spike activity in cerebral cortex. *IEEE Trans Neural Syst Rehabil Eng* **11**, 151-155 (2003).

131. W. M. Grill, Signal Considerations for Chronically Implanted Electrodes for Brain Interfacing Environment. (2008).

132. C. R. Butson, C. B. Maks, C. C. McIntyre, Sources and effects of electrode impedance during deep brain stimulation. *Clinical Neurophysiology* **117**, 447-454 (2006).

133. K. M. Kovach *et al.*, High-throughput in vitro assay to evaluate the cytotoxicity of liberated platinum compounds for stimulating neural electrodes. *Journal of Neuroscience Methods* **273**, 1-9 (2016).

134. I. Vořišek, M. Hájek, J. Tintěra, K. Nicolay, E. Syková, Water ADC, extracellular space volume, and tortuosity in the rat cortex after traumatic injury. *Magnetic Resonance in Medicine* **48**, 994-1003 (2002).

135. T. Roitbak, E. Syková, Diffusion barriers evoked in the rat cortex by reactive astrogliosis. *Glia* **28**, 40-48 (1999).

136. C. L. Kolarcik *et al.*, In vivo effects of L1 coating on inflammation and neuronal health at the electrode-tissue interface in rat spinal cord and dorsal root ganglion. *Acta Biomater* **8**, 3561-3575 (2012).

137. X. Cui *et al.*, Surface modification of neural recording electrodes with conducting polymer/biomolecule blends. *J Biomed Mater Res* **56**, 261-272 (2001).

138. L. Kam, W. Shain, J. N. Turner, R. Bizios, Selective adhesion of astrocytes to surfaces modified with immobilized peptides. *Biomaterials* **23**, 511-515 (2002).

139. K. Tashiro *et al.*, A synthetic peptide containing the IKVAV sequence from the A chain of laminin mediates cell attachment, migration, and neurite outgrowth. *Journal of Biological Chemistry* **264**, 16174-16182 (1989).

140. W. Shain *et al.*, Controlling cellular reactive responses around neural prosthetic devices using peripheral and local intervention strategies. *IEEE Trans Neural Syst Rehabil Eng* **11**, 186-188 (2003).

141. W. D. Callister, *Materials Science And Engineering: An Introduction.* (John Wiley & Sons, 2007).

142. K. H. J. Buschow, *Encyclopedia of materials: science and technology.* (Elsevier, 2001).

143. S. Lin-Gibson *et al.*, Synthesis and Characterization of PEG Dimethacrylates and Their Hydrogels. *Biomacromolecules* **5**, 1280-1287 (2004).

144. D. C. Lin, E. K. Dimitriadis, F. Horkay, Robust Strategies for Automated AFM Force Curve Analysis---I. Non-adhesive Indentation of Soft, Inhomogeneous Materials. *Journal of Biomechanical Engineering* **129**, 430-440 (2007).

145. J. A. W. van Dommelen, T. P. J. van der Sande, M. Hrapko, G. W. M. Peters, Mechanical properties of brain tissue by indentation: Interregional variation. *Journal of the Mechanical Behavior of Biomedical Materials* **3**, 158-166 (2010).

146. A. Sridharan, S. D. Rajan, J. Muthuswamy, Long-term changes in the material properties of brain tissue at the implant–tissue interface. *Journal of Neural Engineering* **10**, 066001 (2013).

147. S. Lin-Gibson, R. L. Jones, N. R. Washburn, F. Horkay, Structure−Property Relationships of Photopolymerizable Poly(ethylene glycol) Dimethacrylate Hydrogels. *Macromolecules* **38**, 2897-2902 (2005).

148. I. De Graeve, J. Vereecken, A. Franquet, T. Van Schaftinghen, H. Terryn, Silane coating of metal substrates: Complementary use of electrochemical, optical and thermal analysis for the evaluation of film properties. *Progress in Organic Coatings* **59**, 224-229 (2007).

149. V. Gupta, N. Madaan, D. S. Jensen, S. C. Kunzler, M. R. Linford, Hydrogen Plasma Treatment of Silicon Dioxide for Improved Silane Deposition. *Langmuir* **29**, 3604-3609 (2013).

150. S.-H. Yang, Y.-S. J. Lee, F.-H. Lin, J.-M. Yang, K.-s. Chen, Chitosan/poly(vinyl alcohol) blending hydrogel coating improves the surface characteristics of segmented polyurethane urethral catheters. *Journal of Biomedical Materials Research Part B: Applied Biomaterials* **83B**, 304-313 (2007).

151. R. A. Evangelista, M. V. Sefton, Coating of two polyetoer-polyurethanes and polyethylene with a heparin-poly-(vinyl alcohol) hydrogel. *Biomaterials* **7**, 206-211 (1986).

152. J. A. Beamish, J. Zhu, K. Kottke-Marchant, R. E. Marchant, The effects of monoacrylated poly(ethylene glycol) on the properties of poly(ethylene glycol) diacrylate hydrogels used for tissue engineering. *Journal of Biomedical Materials Research Part A* **92A**, 441-450 (2010).

153. S. Arati, K. N. Jessica, R. C. Jeffrey, M. Jit, Compliant intracortical implants reduce strains and strain rates in brain tissue in vivo. *Journal of Neural Engineering* **12**, 036002 (2015).

154. J. L. Skousen *et al.*, Reducing surface area while maintaining implant penetrating profile lowers the brain foreign body response to chronically implanted planar silicon microelectrode arrays. *Progress in brain research* **194**, 167-180 (2011).

155. J. P. Mazzoccoli, D. L. Feke, H. Baskaran, P. N. Pintauro, Mechanical and cell viability properties of crosslinked low- and high-molecular weight poly(ethylene glycol) diacrylate blends. *J Biomed Mater Res A* **93**, 558-566 (2010).

156. C.-C. Lin, K. S. Anseth, PEG Hydrogels for the Controlled Release of Biomolecules in Regenerative Medicine. *Pharmaceutical Research* **26**, 631-643 (2009).

157. J. Zhu, Bioactive modification of poly(ethylene glycol) hydrogels for tissue engineering. *Biomaterials* **31**, 4639-4656 (2010).

158. T. R. Hoare, D. S. Kohane, Hydrogels in drug delivery: Progress and challenges. *Polymer* **49**, 1993-2007 (2008).

159. T. Tikka, B. L. Fiebich, G. Goldsteins, R. Keinänen, J. Koistinaho, Minocycline, a Tetracycline Derivative, Is Neuroprotective against Excitotoxicity by Inhibiting Activation and Proliferation of Microglia. *The Journal of Neuroscience* **21**, 2580-2588 (2001).

160. L. Spataro *et al.*, Dexamethasone treatment reduces astroglia responses to inserted neuroprosthetic devices in rat neocortex. *Exp Neurol* **194**, 289-300 (2005).

161. K. A. Potter *et al.*, The effect of resveratrol on neurodegeneration and blood brain barrier stability surrounding intracortical microelectrodes. *Biomaterials* **34**, 7001-7015 (2013).

162. D.-H. Kim, M. Abidian, D. C. Martin, Conducting polymers grown in hydrogel scaffolds coated on neural prosthetic devices. *Journal of Biomedical Materials Research Part A* **71A**, 577-585 (2004).

163. R. Deumens, A. Blokland, J. Prickaerts, Modeling Parkinson's Disease in Rats: An Evaluation of 6-OHDA Lesions of the Nigrostriatal Pathway. *Experimental Neurology* **175**, 303-317 (2002).

164. W. Querbes *et al.*, Direct CNS Delivery of siRNA Mediates Robust Silencing in Oligodendrocytes. *Oligonucleotides* **19**, 23-30 (2008).

165. Y. Liu, J. Zhou, Oligodendrocytes in neurodegenerative diseases. *Frontiers in Biology* **8**, 127-133 (2013).

166. I. Magen, E. Hornstein, Oligonucleotide-based therapy for neurodegenerative diseases. *Brain Research* **1584**, 116-128 (2014).

167. A. E. Forte, S. Galvan, F. Manieri, F. Rodriguez y Baena, D. Dini, A composite hydrogel for brain tissue phantoms. *Materials & Design* **112**, 227-238 (2016).

168. C.-C. Lin, A. T. Metters, Hydrogels in controlled release formulations: Network design and mathematical modeling. *Advanced Drug Delivery Reviews* **58**, 1379-1408 (2006).

169. G. W. Ashley, J. Henise, R. Reid, D. V. Santi, Hydrogel drug delivery system with predictable and tunable drug release and degradation rates. *Proceedings of the National Academy of Sciences* **110**, 2318-2323 (2013).

170. T. D. Y. Kozai, A. S. Jaquins-Gerstl, A. L. Vazquez, A. C. Michael, X. T. Cui, Dexamethasone retrodialysis attenuates microglial response to implanted probes in vivo. *Biomaterials* **87**, 157-169 (2016).

171. M. Asplund, C. Boehler, T. Stieglitz, Anti-inflammatory polymer electrodes for glial scar treatment: Bringing the conceptual idea to future results. *Frontiers in Neuroengineering* **7**, (2014).

172. E. Azemi, C. F. Lagenaur, X. T. Cui, The surface immobilization of the neural adhesion molecule L1 on neural probes and its effect on neuronal density and gliosis at the probe/tissue interface. *Biomaterials* **32**, 681-692 (2011).

173. L. Kam, W. Shain, J. N. Turner, R. Bizios, Selective adhesion of astrocytes to surfaces modified with immobilized peptides. *Biomaterials* **23**, 511-515 (2002).

174. K. A. Potter-Baker *et al.*, Development of Superoxide Dismutase Mimetic Surfaces to Reduce Accumulation of Reactive Oxygen Species for Neural Interfacing Applications. *Journal of materials chemistry. B, Materials for biology and medicine* **2**, 2248-2258 (2014).

175. W. He, G. C. McConnell, T. M. Schneider, R. V. Bellamkonda, A Novel Anti-inflammatory Surface for Neural Electrodes. *Advanced Materials* **19**, 3529-3533 (2007).

176. A. H. Taub, R. Hogri, A. Magal, M. Mintz, Y. Shacham-Diamand, Bioactive anti-inflammatory coating for chronic neural electrodes. *Journal of Biomedical Materials Research Part A* **100A**, 1854-1858 (2012).

177. X. Cui, J. Wiler, M. Dzaman, R. A. Altschuler, D. C. Martin, In vivo studies of polypyrrole/peptide coated neural probes. *Biomaterials* **24**, 777-787 (2003).

7 APPENDICES

APPENDIX A. MICROMOTION EQUIPMENT SETUP:

This section details the electrical schematic and the program used to control the micromotion magnitude and frequency in the micromotion simulation model.

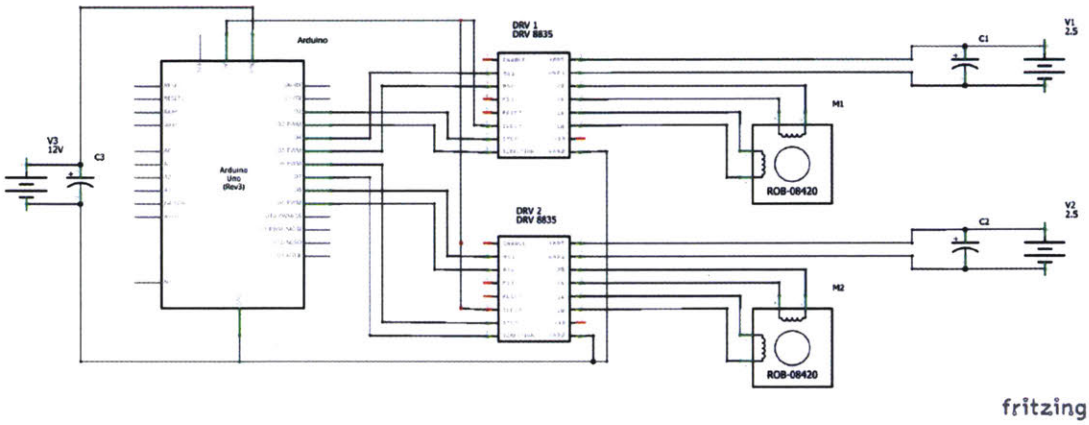

Figure 7-1 Electrical Schematic Diagram for the Micromotion Model
Two high precision linear actuators (Haydon Kirk 21H4U-2.5-907) are driven by an Arduino Uno microcontroller board and TI DRV8834 stepper motor drivers.

7.1.1 Arduino Code to Program Linear Actuators

The program used to drive the linear actuators is detailed below. The distance travelled is controlled by the programmed number of steps. The frequency is controlled by the programmed delay (in milliseconds).

// Shows how to multiple simultaneous steppers

// Runs one stepper forwards and backwards, accelerating and decelerating at the limits. Runs other steppers at the same time

// Copyright (C) 2009 Mike McCauley

// $Id: MultiStepper.pde,v 1.1 2011/01/05 01:51:01 mikem Exp mikem $

#include <AccelStepper.h>

```
// Define some steppers and the pins the will use


AccelStepper stepper1(AccelStepper::DRIVER, 2, 3);

AccelStepper stepper2(AccelStepper::DRIVER, 6, 7);

// Micro-Step Resolution Pins


int m0x=4;  // Pin 4, M0X

int m1x=5;  // Pin 5, M1X

int m0y=8;  // Pin 8, M0Y

int m1y=9;  // Pin 9, M1Y

void setup()

{

  stepper1.setMaxSpeed(10000.0);

  stepper1.setMinPulseWidth(20);

  stepper1.setAcceleration(10000.0);

  stepper1.moveTo(0);


  stepper2.setMaxSpeed(8000.0);

  stepper2.setMinPulseWidth(20);

  stepper2.setAcceleration(10000.0);

  stepper2.moveTo(-5);
```

```
  ///////STEP RESOLUTIONS


  digitalWrite(m0x,LOW);  //full: low, low; half: high, low; quarter: float, low; eigth:
low, high; sixteenth: high, high; thirty-second: float, high
  digitalWrite(m1x,LOW);
  //--------------------
  digitalWrite(m0y,LOW);
  digitalWrite(m1y,LOW);
}
void loop()
{
  // Change direction at the limits
  if (stepper1.distanceToGo() == 0)
        stepper1.moveTo(-stepper1.currentPosition());
  if (stepper2.distanceToGo() == 0)
    {delay(2000);
        stepper2.moveTo(-stepper2.currentPosition());
    }
  stepper1.run();
  stepper2.run();
}
```